Spectroscopy and Decays of Charmed Strange Mesons

A THESIS

PRESENTED TO THE FACULTY OF THE GRADUATE SCHOOL

OF THE UNIVERSITY OF MINNESOTA

BY

Selina Zhao Li

IN PARTIAL FULFILLMENT OF THE REQUIREMENTS

FOR THE DEGREE OF

DOCTOR OF PHILOSOPHY

Jon Urheim, Advisor

December 2004

Spectroscopy and Decays of Charmed Strange Mesons

by Selina Zhao Li

Under the supervision of Professor Jon Urheim

ABSTRACT

Using $13.4 fb^{-1}$ of e^+e^- collision data taken with the CLEO-II detector at center-of-mass energies near 10.6 GeV, we present two analyses to study the spectroscopy and decays of charmed strange mesons.

In the first analysis, we have obtained the first confirming evidence for the existence of the $D^*_{sJ}(2317)^+$. We have also observed and established the existence of a second narrow resonance, denoted as the $D_{sJ}(2463)^+$. The two narrow resonances are observed in the $D_s^+\pi^0$ and $D_s^{*+}\pi^0$ final state, respectively. Accounting for the cross-feed backgrounds due to the addition or omission of photons, we have measured the mean mass differences $\langle \Delta M(D_s\pi^0)\rangle = 350.0 \pm 1.2$ [stat.] ± 1.0 [syst.] MeV/c^2 for the $D^*_{sJ}(2317)^+$ state, and $\langle \Delta M(D_s^*\pi^0)\rangle = 351.2 \pm 1.7$ [stat.] ± 1.0 [syst.] MeV/c^2 for the new $D_{sJ}(2463)^+$ state. We have also searched, but find no evidence, for decays of the two states via the channels $D_s^{*+}\gamma$, $D_s^+\gamma$, and $D_s^+\pi^+\pi^-$. The observations of the two

states at 2.32 and 2.46 GeV/c^2, in the $D_s^+\pi^0$ and $D_s^{*+}\pi^0$ decay channels respectively, are consistent with their interpretations as $c\overline{s}$ mesons with orbital angular momentum $L = 1$, and spin-parity $J^P = 0^+$ and 1^+.

In the second analysis, we report an improved measurement of the partial width for the decay $D_s^+ \to \mu^+\nu_\mu$. Using a neutrino reconstruction method based on missing energy and momentum, we identify a sample of $D_s^+ \to \mu^+\nu_\mu$ candidates. Specifically we measure the branching fraction to be $\mathcal{B}(D_s \to \mu^+\nu_\mu)/\mathcal{B}(D_s \to \phi\pi^+) = 0.167 \pm 0.031[\text{stat.}]\pm 0.011[\text{syst.}]$, from which we extract the pseudoscalar decay constant $f_{D_s} = (270 \pm 25 \pm 9 \pm 34)$ MeV where the last error in f_{D_s} is due to the uncertainty on the previously meassured value for $\mathcal{B}(D_s^+ \to \phi\pi^+)$.

To my parents and my siblings.

ACKNOWLEDGEMENTS

Special thanks first go to my thesis advisor, Jon Urheim, for all of his help and understanding through the last three and a half years. I would have not made it this far without him. I am especially grateful that he continued to advise me even after he moved to Indiana University. His encouragement and support have helped me through difficult times.

I would like to thank people from the Wilson Synchrotron Lab for making my work enjoyable and educational. I apologize in advance if I forget to name every single one of you who helped me through my work here at Wilson Lab. Chris Stepaniak helped my move to Ithaca smoothly, and continued to be a good friend who I can chat with about almost everything. Stefan Anderson had been a great help when I first came to the Wilson Lab. Sangjoon Lee was a good person to chat with in the Minnesota office. Alex Smith had given me some good advice on charm physics. Kaiyan Gao had been a good company and gave me valuable advice about life although I have to admit that it was impossible to argue with her. Datao Gong helped share the Crystal Calorimeter (CC) responsibilties. Zhongchao Li was always there to talk to. Alexander Scott allowed me to show him how to play ping pong. I want to thank Tim Klein for taking over the CC hardware responsibilities so that I can focus on finishing up my thesis. I also want to thank David Kreinick for putting a smile on my face every working day. Sorry if I forgot to come by to say "good morning" occasionally.

I will never forget the time when Steve Gray and you sang me the Birthday song. Thanks to Tom Meyer for sharing his expertise in CC electronics and for training me to be a CC expert. I was very inspired by his detailed documentations. His dedication to the CLEO detector was greatly appreciated and acknowledged. Brian Heltsley shared his knowledge in calorimeter and provided guidance as well. Dan Cronin-Hennessy had been the best run manager I ever got to work closely with. I learned some good usage of PAW from him as well. His dedication to research was admirable, just like Edward Thorndike's. Ed helped deliver printouts and never failed to deliver a smile too. The hike to the Lick Brook Trails with Ed was adventurous and unforgetable. Basit Arthar was one of the first CLEOns I got to know after I arrived Ithaca. Jim Alexander shared his expertise in silicon detector and also provided me advice in future experiments, job search and preparation, etc.. David Cassel provided a lot of advice and allowed me to sit in his experimental high energy physics class offered at Cornell. Rich Galik showed concerns and encouragement in times I needed them. Pete Zweber always either made me laugh out loud or scared me to death. Jana and Greg Thayer shared their experience at CLEO. Jana won't stop looking until she found the answer to my questions. Lauren Hsu and Hanna Mahlke-Krueger were wonderful in organizing ladies' get-togethers. People from the electronic shops at Wilson Lab also deserve some thanks for helping with the CC hardware repairs, especially Bill Lucas and John Barley. The CLEO collaboration has been like a family to me. It is hard for me to say goodbye to such a nice and friendly collaboration.

I would like to thank other main authors of the D_{sJ} paper for CLEO: David Cinabro, Sheldon Stone, Jon Urheim, and J.C. Wang for their contribution to the

analysis. It was an exciting period and it was my pleasure to be able to work closely with all of them. One month of hard work was definitely worth it. I thank the D_{sJ} paper committee: Roy Briere, David Miller, John Yelton and Dave Besson. The CLEO management: David Cassel, Ian Shipsey, and Rich Galik helped us get the D_{sJ} results presented in Chapter 3 published quickly.

I also want to thank people I got to know outside of work in Ithaca. Tae Kwon Do (TKD) has been something fun I started since I first arrived Cornell University. First, I want to thank my TKD instructors. Alison Dietrich, Sue Irvine and Nancy Moore had been great in teaching me the TKD basic techniques, forms, sparing, as well as self-defense skills that really help me build confidence. I hope to see you all in the summer camp special training for the years to come. Bob Meller is an excellent teacher in TKD. I thank him for being patient with me and for showing me the techniques of kicks and punches to every single detail. My friends in Ithaca also deserve a lot of thanks. Clinton Cronin had been a wonderful dance partner and a best friend. I want to thank him for making me smile and for adding flavors to my life. It had been fun going to Salsa dancing with Clinton, Matt Chasse and Paras Naik. The Sunday open mic night at the Nines was memorable. Curtis Jastremsky threw great parties and I had the privilege to hear him sing during their jam sessions at Paras'. It had been fun hanging out with Janelle Tompkins and Aaron Young. I wish we had more time to go dancing. It was my pleasure to get to know a local artist like Janelle. Richard Eshelman gave me my very first lesson in Merengue and introduced me to Latin dancing that made my last year in Ithaca entertaining. Dave Rice led me in doing the difficult part of turning in Bachata. These people have made

my life in Ithaca so enjoyable that I don't really want to leave.

I thank my Physis professors from the University of Minnesota. Benjamin Bayman who not only taught me classical mechanics, but not helped me and other graduate students with the written qualifying exam. Mikhail Voloshin and Arkady Vainshtein taught me Particle Physics, and Serge Rudaz made Quantum Field Theory interesting and reasonable. I want to thank Ron Poling for his support and understanding. Yuichi Kubota was my academic advisor for the first two years of my graduate studies. I had a good time with friends from my first two years of graduate studies: Tatsuhiko Sagara, Xifeng Han, Eunjung Ko, Tao Qian, Emily Maher, Bernard Becker, Ben Bousquet, Sarwa Tan, and Christina Nieman. Christina became my best friend who invited me to holiday celebrations with her family in Minnesota. She had taught me a lot of American family traditions.

Of course, I also want to express my gratitude toward the Physics professors Paul Brady, Ling-Lie Chau, Randy Harris, Winston Ko, Richard Lander, and Richard Scalettar from University of California, Davis. The McNair Scholar's program at UC Davis helped me with my graduate school application and preparation.

I thank my first Physcis teacher Qiuxian Tan from junior high school in China. He believed that one day I would get my Ph.D., and here I am. I did it.

At Last but not least, I would like to thank my family. There is no words can describe the love and support I got from my family. I dedicate this thesis to them.

TABLE OF CONTENTS

1 Introduction **1**

1.1 The Standard Model 1

1.2 Spectroscopy and Basic Properties of $c\overline{s}$ Mesons 3

1.2.1 The S-Wave States 5

1.2.2 The P-Wave States 7

1.3 Meson Decay Constants 10

1.4 An Overview of This Thesis 13

2 Experimental Apparatus **14**

2.1 CESR e^+e^- Collider 14

2.2 The CLEO Detector 20

2.2.1 The Tracking System 22

2.2.2 The Time-of-Flight System 29

2.2.3 Electromagnetic Calorimeter 29

2.2.4 The Solenoidal Magnet 31

2.2.5 The Muon Chambers 32

2.3 The Trigger and Data Acquisition System 33

2.4 Event Reconstruction 35

2.5 Particle Identification 35

2.5.1 Hadron Identification Using $\frac{dE}{dx}$ 36

2.5.2 Photon Identification 38

2.5.3 Muon Identification 39

2.5.4 Electron Identification 39

2.6 Monte Carlo Simulations for Physics 40

3 The Observation of Two New Particles **42**

3.1 General Approach 42

3.2 Confirmation of $D^*_{sJ}(2317)^+ \to D^+_s\pi^0$ 43

3.2.1 Event Selection Criteria 43

3.2.2 The $D^*_{sJ}(2317)$ Signal 46

3.3 Searches for $D^*_{sJ}(2317)$ in Other Decay Modes 58

3.3.1 Decays to $D_s\gamma$ 58

3.3.2 Decays to $D^*_s\gamma$ 61

3.3.3 Decays to $D_s\pi^+\pi^-$ 62

3.3.4 Decays to $D_s^*\pi^0$ . . . 66
3.3.5 Summary of Different Decay Modes for $D_{sJ}^*(2317)$ . . . 68
3.4 Observation of a New State at 2.463 $\mathbf{GeV/c^2}$ . . . 68
3.4.1 Analysis of Cross Feed between $D_s^+\pi^0$ and $D_s^{*+}\pi^0$ Samples . . . 70
3.4.2 Further Evidence for the $D_{sJ}(2460)^+ \to D_s^*\pi^0$ Decay . . . 76
3.5 Searches for $D_{sJ}(2460)$ in Other Decay Modes . . . 79
3.5.1 Decays to $D_s\gamma$ . . . 79
3.5.2 Decays to $D_s^*\gamma$ . . . 82
3.5.3 Decays to $D_s\pi^+\pi^-$ . . . 82
3.5.4 Decays to $D_{sJ}^*(2317)\gamma$ . . . 85
3.5.5 Summary of Different Decay Modes for $D_{sJ}(2460)$ . . . 85
3.6 Properties of the $D_{sJ}^*(2317)^+$ and $D_{sJ}(2460)^+$ States . . . 86
3.6.1 Mass and Width of the $D_{sJ}^*(2317)^+$ . . . 86
3.6.2 Mass and Width of the $D_{sJ}(2460)^+$ . . . 89
3.7 Conclusions and Discussion . . . 89

4 Leptonic Decays of D_s Mesons **92**
4.1 Experimental Status of Leptonic D_s Decay . . . 92
4.2 Analysis Method for $D_s \to \mu\nu$ . . . 94
4.2.1 General Approach . . . 94
4.2.2 Data Samples . . . 96
4.2.3 Event Selection Criteria . . . 102
4.2.4 Neutrino Reconstruction . . . 104
4.2.5 Cut Optimization for Background Suppression . . . 109
4.2.6 Background Estimation . . . 116
4.2.7 Signal Shape and Efficiency . . . 125
4.3 Normalization Mode $D_s^+ \to \phi\pi^+$ . . . 127
4.4 Results . . . 130
4.4.1 Fit Results . . . 130
4.4.2 Systematic Uncertainties . . . 133
4.4.3 Cross-checks . . . 139
4.5 Conclusions . . . 145

5 Conclusions **149**

BIBLIOGRAPHY **151**

LIST OF TABLES

3.1 Summary of the $D_s\pi^0$ yield as function of fit and selection variations. 57
3.2 90% CL upper limits on the ratio of branching fractions for $D^*_{sJ}(2317)$ to the decay modes shown relative to the $D_s^+\pi^0$ state 70
3.3 Observed numbers of events based on observed numbers and feed up and down. 74
3.4 90% CL upper limits on the ratio of branching fractions for $D_{sJ}(2460)$ to the decay modes shown relative to the $D_s^{*+}\pi^0$ state 86

4.1 Summary of measurements of the decay constants for the D_s. 92
4.2 Summary of Monte Carlo samples used in this analysis. 97
4.3 The ratio of on/off-resonance in MC and data 111
4.4 The background modes in CLEOII+II.V Continuum MC 117
4.5 The lepton fake rates (%) for $P > 2.4$ GeV/c in data 119
4.6 The hadron fraction in CLEOII.V continuum MC 120
4.7 The decay in flight correction determined using $D^{*+} \to \pi^+ D^0$, $D^0 \to K^-\pi^+$ MC sample. 120
4.8 Total lepton fake rates (%) determined for data 121
4.9 the number of reconstructed D_s^* events $N_{D_s^*}$ and D_s events N_{D_s}, as well as their corresponding reconstruction efficiency $\epsilon_{D_s^*}$ and ϵ_{D_s} . . . 125
4.10 Summary for efficiency and signal yield for the normalization mode $D_s^* \to \gamma D_s$, $D_s \to \phi\pi$, $\phi \to K^+K^-$. 130
4.11 Summary for the overall reconstruction efficiency and signal yield for the normalization mode $D_s^* \to \gamma D_s$, $D_s \to \mu\nu$. 131
4.12 The ratio of the decay width $\Gamma(D_s \to \mu\nu)/\Gamma(D_s \to \phi\pi)$. 133
4.13 Estimated systematic errors on the decay width ratio. 133
4.14 The neutrino reconstruction efficiency ϵ_ν in MC and data 135
4.15 The neutrino reconstruction efficiency ϵ_ν for CLEOII MC and data with different values of M_{jet}. 135
4.16 The lepton fake rates calculated with different hadron fractions. . . . 137
4.17 The number of reconstructed signal events from different fits to $\Delta M = M(\gamma\mu\nu) - M(\mu\nu)$ 138

LIST OF FIGURES

1.1 The low-lying spectroscopy of the $c\overline{s}$ mesons. 4
1.2 Feynman diagram for the leptonic decay $M_{Q\bar{q}} \to l\nu$ of a charged meson. 11

2.1 The CESR e^+e^- collider. 15
2.2 The hadronic cross-section in the Upsilon region. 19
2.3 The side view of the CLEO II.V detector 21
2.4 A layout of the PT, VD and DR tracking system 23
2.5 Cross-sectional views of the silicon vertex detector 25
2.6 A cross-section of a muon chamber super-layer. 32
2.7 Measured dE/dx as a function of momentum 37

3.1 The distribution of the helicity angle of the $\phi \to KK$ decay in signal MC and data 45
3.2 Fitting the mass distributions for $M(\phi\pi)$ 47
3.3 The distribution of $M(D_s)$ and $M(D_s\pi^0)$ in CLEOII+II.V data . . . 48
3.4 The distribution of $M(D_s\pi^0)$ and $\Delta M(D_s\pi^0)$ in CLEOII+II.V data and MC 50
3.5 $D_s^*(2112)^\pm \to D_s^\pm\pi^0$, $D_s^\pm \to \phi\pi^\pm$, $\phi \to K^+K^-$ in continuum MC and data 51
3.6 The $D_s\pi^0$ mass and mass difference spectrum showing the effect of the E9/E25 1% cut. 52
3.7 The distribution of $M(D_s\pi^0)$ in CLEOII+II.V data with different photon energy cuts applied to both photons of the π^0 daughter. 53
3.8 The distribution of `SGKADI` for kaons. 54
3.9 The mass distribution in CLEOII+II.V data 55
3.10 The fit to the mass difference distributions in $D_{sJ}^*(2317) \to D_s\pi^0$ signal MC and data 56
3.11 The mass difference $M(D_s\gamma) - M(D_s)$ in data 59
3.12 The fit to mass difference $M(\gamma\phi\pi) - M(\phi\pi)$ for $D_s^{*+} \to D_s^+\gamma$ signal MC and $D_{sJ}^*(2317)^+ \to D_s^+\gamma$ in data 60
3.13 The spectrum of the mass difference $\Delta M(D_s^*\gamma) = M(D_s^*\gamma) - M(D_s^*)$ for $D_s^*\gamma$ candidates. 62
3.14 The mass difference $\Delta M(D_s^*\gamma)$ for $D_{sJ}^*(2317)^+ \to D_s^{*+}\gamma$, $D_s^{*+} \to D_s^+\gamma$, $D_s^+ \to \phi\pi^+$, $\phi \to K^+K^-$ signal MC and data 63

3.15 The mass difference $\Delta M(D_s\pi\pi) = M(D_s\pi\pi) - M(D_s)$ for $D_s^+\pi^+\pi^-$ candidates 64
3.16 The mass difference $\Delta M(D_s\pi\pi)$ for $D_{sJ}^*(2317)^+ \to D_s^+\pi^+\pi^-$, $D_s^+ \to \phi\pi^+$, $\phi \to K^+K^-$ signal MC and data 65
3.17 The $D_s\pi^0$ mass spectrum comparing different track selections 67
3.18 The mass difference spectrum $\Delta M(D_s^*\pi^0) = M(D_s\gamma\pi^0) - M(D_s\gamma)$. 69
3.19 The mass difference spectra $\Delta M(D_s\pi^0)$ using $D_{sJ}^*(2320)^+ \to D_s^+\pi^0$ and $D_{sJ}(2460)^+ \to D_s^{*+}\pi^0$ signal MC 71
3.20 The mass difference spectra $\Delta M(D_s^*\pi^0)$ using $D_{sJ}(2460)^+ \to D_s^{*+}\pi^0$ and $D_{sJ}^*(2320)^+ \to D_s^+\pi^0$ signal MC 72
3.21 Finding out the significance of the $D_s^*\pi^0$ signal 77
3.22 The mass difference spectra $\Delta M(D_s^*\pi^0)$ after Ds* side band subtraction 78
3.23 The fit to mass difference $M(D_s\gamma) - M(D_s)$ for $D_s(2460)^+ \to D_s^+\gamma$ signal MC and data 80
3.24 The mass difference $M(D_s\gamma) - M(D_s)$ in data. 81
3.25 $D_s(2460)^+ \to D_s^{*+}\gamma$, $D_s^{*+} \to D_s^+\gamma$, $D_s^+ \to \phi\pi^+$, $\phi \to K^+K^-$ in signal MC and data 83
3.26 $D_s(2460)^+ \to D_s^+\pi^+\pi^-$, $D_s^+ \to \phi\pi^+$, $\phi \to K^+K^-$ in signal MC and data 84
3.27 The two Gaussian fit to the mass difference distributions in $D_{sJ}^*(2317) \to D_s\pi^0$ data 88

4.1 The distribution of momenta (in GeV/c) for CLEOII signal MC at the generator-level. 98
4.2 The D_s^* momentum spectrum before and after tuning 100
4.3 The D_s and D_s^* momentum spectrum 101
4.4 The m_{jet} as a function of momentum 107
4.5 The D_s mass constraint ellipsoid 107
4.6 A comparison of the mass difference before and after D_s mass constraint. 108
4.7 The distribution of the background suppression variables for tagged signal and background events 110
4.8 Plots of charge*$Cos(\theta_{P_{lepton}})$ and ΔM 112
4.9 The 2-D plots of charge*$Cos(\theta_{P_{lepton}})$ vs. charge*$Cos(\theta_{P_{miss}})$ 114
4.10 The distribution of charge*$Cos(\theta_{P_{lepton}})$ (top) and mass difference . . 115
4.11 The mass difference for the following background modes 122
4.12 Production rate D_s^*/D_s as a function of D_s momentum cut for CLEOII and II.V data. 124
4.13 The fit to the mass difference after the D_s mass constraint for $D_s \to \mu\nu$ CLEOII and CLEOII.V signal MC. 126
4.14 The distribution of $M(\phi\pi)$ 128

4.15 Fits to the mass difference for $D_s^* \to \gamma D_s$, $D_s \to \phi\pi$, $\phi \to K^+K^-$ . . 129
4.16 A fit to the mass difference for $D_s \to \mu\nu$ 132
4.17 the mass difference for CLEOII+II.V continuum MC and data for the muon and electron modes 140
4.18 A fit to the mass difference for $D_s \to \mu\nu$ 141
4.19 The coordinate system with P_{D_s} defined to be pointed along the z-axis. Muon is placed on the y-z plane. ψ is then the psi angle between the photon and the y-z plane. 142
4.20 The mass difference and its fit to the muon data with kinematic constraints. 144
4.21 A fit to the background subtracted mass difference with kinematic constraints applied for CLEOII+II.V data. 146

CHAPTER 1

Introduction

1.1 The Standard Model

To our current knowledge, all matter is made of three kinds of elementary particles: quarks, leptons, and gauge bosons. There are six types, or flavors, of quarks: up (u), down (d), strange (s), charm (c), bottom (b), and top (t). They can be classified into three generations, with electric charge $\frac{2}{3}e$ for the quarks in the first row and $-\frac{1}{3}e$ for those in the second:

$$\begin{pmatrix} u \\ d \end{pmatrix}, \begin{pmatrix} c \\ s \end{pmatrix}, \begin{pmatrix} t \\ b \end{pmatrix}.$$

Each quark also has its corresponding antiquark with opposite charge. Quarks are never found separately, but only inside composite particles called hadrons. There are two classes of hadrons that are composed of quarks: baryons, which contain three quarks, and mesons, which contain one quark and one antiquark. Similarly, there are six leptons: electron (e), electron neutrino (ν_e), muon (μ), muon neutrino (ν_μ), tau (τ), and tau neutrino (ν_τ). They also fall into three generations, with charge $-e$ for

the leptons in first row and no charge for those in the second:

$$\begin{pmatrix} e \\ \nu_e \end{pmatrix}, \begin{pmatrix} \mu \\ \nu_\mu \end{pmatrix}, \begin{pmatrix} \tau \\ \nu_\tau \end{pmatrix}.$$

The Standard Model accounts for the electromagnetic, weak, and strong interactions of the quarks and leptons. Each interaction has gauge bosons or mediators associated with it: a photon for the electromagnetic interaction, two charged vector bosons $W^{\pm}$ and one neutral Z^0 for the weak interaction, and eight gluons for the strong interaction.

In high energy physics, a considerable amount of effort is devoted to measurements of fundamental standard-model parameters and understanding decay dynamics. The Cabibbo-Kobayashi-Maskawa (CKM) matrix elements V_{ij} are fundamental input parameters of the Standard Model, and cannot be predicted. The CKM matrix $\mathbf{V}$ describes the rotation of the physical quark states (d, s, b) to a set of weak interaction eigenstates (d', s', b'):

$$\begin{pmatrix} d' \\ s' \\ b' \end{pmatrix} = \begin{pmatrix} V_{ud} & V_{us} & V_{ub} \\ V_{cd} & V_{cs} & V_{cb} \\ V_{td} & V_{ts} & V_{tb} \end{pmatrix} \begin{pmatrix} d \\ s \\ b \end{pmatrix}.$$

The matrix elements V_{ij} measure the relative weak couplings between quarks of different flavors, and can be complex.

By definition, the CKM matrix must satisfy the unitarity condition $\mathbf{V}\mathbf{V}^{\dagger} = 1$. Furthermore, the off-diagonal elements are small and close to zero, reflecting the fact that the coupling between different generations of the quarks is small. Various

experiments [1] have measured the magnitudes of the CKM matrix elements to be in the intervals:

$$\begin{pmatrix} 0.9739 - 0.9751 & 0.221 - 0.227 & 0.0029 - 0.0045 \\ 0.221 - 0.227 & 0.9730 - 0.9744 & 0.039 - 0.044 \\ 0.0048 - 0.014 & 0.037 - 0.043 & 0.9990 - 0.9992 \end{pmatrix}$$

1.2 Spectroscopy and Basic Properties of $c\overline{s}$ Mesons

A charm quark and an anti-strange quark are bound together to form a $c\overline{s}$ meson. The parity as well as spin and orbital angular momenta are used to describe the state of any particles. The parity P is an intrinsic property of a quark and it is defined to be $+1$ for quark and -1 for an antiquark. Thus, a meson has a parity of $P = (-1)^{(L+1)}$, where L is the magnitude of the orbital angular momentum. In the case of a $c\overline{s}$ meson, we have the spin angular momenta $\vec{s}_c$ and $\vec{s}_s$ which are another intrinsic properties of the quarks and an orbital angular momentum $\vec{L}$ between the c and s quark. The total angular momentum is then $\vec{J} = \vec{L} + \vec{s}_s + \vec{s}_c$. Each quark carries a spin of $\frac{1}{2}$, so the possible values of a meson's spin are non-negative integers. States with values of L larger than 1 are difficult to form and decay rapidly and thus tend to be broad states.

The c quark (with mass $\sim$1.2 GeV/c^2) is heavier than the characteristic energy scale for strong interactions ($\Lambda_{QCD} \sim 300$ MeV), while the s quark (with mass $\sim$0.1 GeV/c^2) is not. The heaviness of the c quark allows us to employ the Heavy Quark Effective Theory (HQET), a theoretical approach that has been successful in describing properties of mesons containing one heavy and one light quark. In the heavy

quark limit, the configuration of the light quark in the meson is not affected by the replacement of the spin of another heavy quark. This is known as the heavy quark symmetry (HQS). In other words, the strong force between the c and s quark decouples from the spin of the c quark, and thus the $\vec{s}_c$ and $\vec{j} = \vec{L} + \vec{s}_s$ are conserved separately.

Two $L = 0$ (S-wave) and four $L = 1$ (P-wave) states are expected for the $c\bar{s}$ mesons. The two ground states with orbital angular momentum $L = 0$ and spin-parity $J^P = 0^-$, $J^P = 1^-$ can be considered as members of a $j = \frac{1}{2}$ doublet. Two of the four orbitally excited states with $L = 1$ namely those with $J^P = 0^+, 1^+$ can be treated as a $j = \frac{1}{2}$ doublet, while the remaining $J^P = 1^+, 2^+$ represent a $j = \frac{3}{2}$ doublet [2, 3]. The known spectroscopy of P-wave (L=1) $c\bar{s}$ mesons prior to 2003 is summarized in Ref.[4]. Figure 1.1 shows the spectroscopy of the currently known

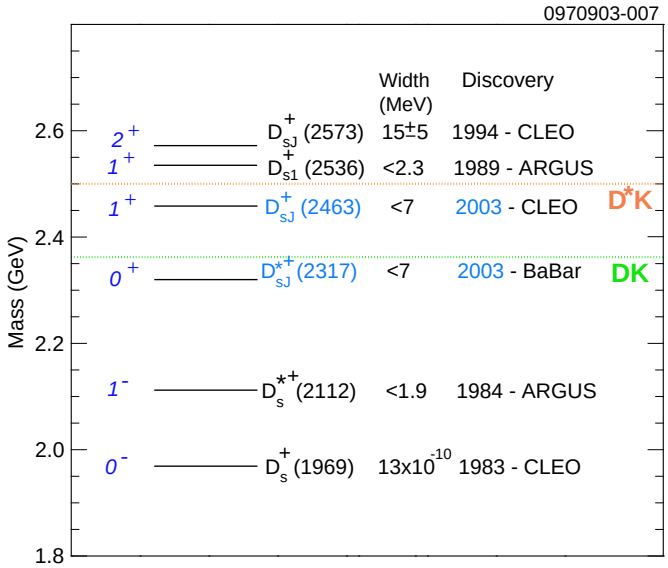

Figure 1.1: The low-lying spectroscopy of the $c\bar{s}$ mesons.

$c\overline{s}$ mesons, including the two new states first observed in 2003. The confirmation of the $D^*_{sJ}(2317)^+$ and discovery of the $D_{sJ}(2460)^+$ are the subject of Chapter 3 in this thesis.

1.2.1 The S-Wave States

The two states with $L = 0$ for $c\overline{s}$ mesons are named D_s and D^{*+}_s. The ground state D_s meson with mass 1969 MeV/c^2 and spin-parity $J^P = 0^-$ was discovered by CLEO [5] in 1983. It is the lightest $c\overline{s}$ meson and only decays weakly.

There are three types of W-boson mediated weak decays of the D_s meson, namely the leptonic, semileptonic, and hadronic decays. In leptonic decays, the mechanism is weak annihilation of the c and s quarks. The process for leptonic decays is $D^+_s \to l^+\nu_l$ where l is a lepton and ν_l is its corresponding antineutrino. The decays are suppressed by angular momentum considerations given the V-A structure of the weak interaction (helicity suppression), and hence with the exception of $D^+_s \to \tau^+\nu_l$, the decay branching fractions are small. The purely leptonic decays of heavy mesons, especially the D_s are discussed in Section 1.3.

The semileptonic decay $D_s \to Xl\nu_l$, where X is a meson less massive than the mass of the D_s meson M_{D_s}. The total semileptonic branching fraction is about 5-6%, dominated by a weak $c \to s$ quark transition, i.e., $D_s \to \phi l\nu$ and $D_s \to \eta l\nu$ where the ϕ and η are primarily $s\overline{s}$. Additionally, there should be Cabibbo-suppressed $c \to d$ quark transitions which give rise to final states shared by the dominant D^0 and D^+ semileptonic decays. The decay rates for a $c \to d$ transistion such as $D_s \to K^{(*)0}l\nu$ are suppressed by a factor of $\tan^2\theta_C \approx 0.05$ relative to that expected from the decays

of non-strange charmed mesons such as the D^0 and D^+, where θ_C is the Cabibbo angle that can be used to characterize the CKM matrix.

In hadronic decays, the decay products of the D_s are hadrons only which suggest that they can interact strongly with each other. The decay mechanism is complicated further as the quarks are bound inside hadrons by strong force. There are quark level diagrams for the weak process that are absent in leptonic and semileptonic decays. For example, in addition to the external spectator diagram, internal spectator, W-exchange and annihilation diagrams could all play a role in the process. Currently, there is not a complete experimental or theoretical picture of hadronic D_s decays although many decay modes have been studied.

The decay rates for hadronic decay modes of the D_s have neither been measured experimentally for all channels, nor are they sufficiently well-understood theoretically to allow absolute branching fractions to be determined from the relative rates alone. Measuring absolute branching fractions for D_s decay modes requires a relatively pure unbiased sample of events containing D_s for the denominator of a branching fraction measurement. This can be achieved with experiments of $e^+e^- \to c\bar{c}$ just above the $D_s^+ D_s^-$ threshold, in which case we can reconstruct a D_s^+ decay in some decay modes and know that there must be a D_s^- recoiling against it. This is totally independent of what mode the D_s^- decayed through, and so it provides a pure and unbiased D_s^- sample. The CLEO-c experiment will be collecting data at the D_s production threshold, providing favorable experimental conditions to study D_s decays.

Currently, the poor knowledge of the absolute branching fraction scale is a severe limitation for the extraction of fundamental physics from branching fraction mea-

surements in the D_s system. As we will see, this uncertainty poses difficulties in interpreting the results of measurements of leptonic decays, described in Chapter 4. The branching fraction scale uncertainty remains large ($> 25\%$) until we have a high statitics sample of the D_s produced at threshold. Establishing this uncertainty at the 1-2% level is an important goal of the CLEO-c program [6] now under way.

The 1^- state D_s^{*+} with a mass of 2112 MeV/c^2 was discovered by ARGUS [7] in 1984. The D_s^{*+} decay dominantly to $D_s^+\gamma$ with a decay probability (or branching fraction) of about 94%. The D_s^{*+} decays primarily electromagnetically because of the isospin and phase-space suppresions of the $D_s\pi^0$ final state. The decay $D_s^* \to D_s\pi^0$ violates isospin symmetry since all $c\overline{s}$ mesons are isospin singlets while the π is an isospin triplet. It is phase-space suppressed since the mass difference between the D_s^* and D_s is about 144 MeV/c^2 which becomes the only energy available to produce a π^0 with mass of $\sim$ 135 MeV/c^2 and not much is left for anything else, and thus the transistion is less likely to occur. As a result of the suppressions, $D_s^{*+} \to D_s\pi^0$ has a branching fraction of only $\sim 6\%$.

1.2.2 The P-Wave States

Prior to 2003, only two of the four $L = 1$ states were observed. Various theories [2, 3, 8, 9, 10] predicted that all four states with $L = 1$ are massive enough that their dominant strong decays would be to the isospin-conserving DK and/or D^*K final states. In the heavy quark limit, they also predict that the two states with $j = \frac{3}{2}$ would be narrow while the two with $j = \frac{1}{2}$ would be broad. The $j = \frac{3}{2}$ states are expected to be narrow because the dominant decays are strong transitions to

$L = 0$ charmed mesons with $j = \frac{1}{2}$ which involve D-wave transitions so as to conserve angular momentum and parity. Such transitions are suppressed by virtue of the large angular momentum centrifugal barrier. The $j = \frac{1}{2}$ states on the other hand can decay via S-wave transitions, and consequently (prior to their observation) had been expected to be broad with widths of $\sim$ 200 MeV, as appears to be the case in the $c\overline{u}$ and $c\overline{d}$ meson systems. The observations of the two narrow $j = \frac{3}{2}$ states as in $D_{s1}(2536) \to D^*K$ by ARGUS [11] in 1989 and $D_{sJ}(2573)^+ \to D^0K^+$ by CLEO [12] in 1994 and the compatibility of the $D_{sJ}(2573)$ with the J^P assignment as 2^+ support these predictions.

The two states with $j = \frac{1}{2}$ remained missing until a new narrow resonance with a mass near 2.32 GeV/c^2 was reported by the BaBar Collaboration [13] in 2003. This new resonance is named the $D^*_{sJ}(2317)^+$ as it is consistent with the spin-parity restrictions imposed by the particular final state observed. The observation of $D^*_{sJ}(2317)$ is unexpected because it is narrow (with intrinsic width $\Gamma < 10$ MeV); it decays to the $D_s^+\pi^0$ final state which is isospin-violating if $D^*_{sJ}(2317)$ is purely a $c\overline{s}$ meson; and its mass (2317.6 ± 1.3 [stat.] MeV/c^2) is smaller than most theoretical predictions for a 0^+ $c\overline{s}$ state. However, if we accept the low mass, the other surprising attributes of isospin-viloation and narrow width follow naturally. It was suggested from the decay products that it could be identified as one of the four $L = 1$ $c\overline{s}$ mesons with spin-parity $J^P = 0^+$. However, by virtue of its low mass, exotic interpretations for this state have also been proposed.

A number of interpretations have appeared [14, 15, 16, 17, 18, 19, 20] to provide theoretical explanations for the narrow resonance after the initial observation of the

$D^*_{sJ}(2317)$. At least two theoretical calculations [21, 22] prior to the $D^*_{sJ}(2317)^+$ observation had suggested that, in the heavy quark limit, the $j = \frac{1}{2}$ states with $J^P = 0^+$ and 1^+ could be considered as chiral partners of the D_s and D^*_s mesons, and thus would be relatively light. In this case, the $D^{(*)}K$ decay modes are not allowed kinematically due to its low mass, and the only allowed strong transition is the isospin-violating final state. Therefore, the isospin suppression in the decay $D^*_{sJ}(2317) \to D^+_s\pi^0$ could explain the small decay width. Cho and Wise [23] suggested a decay mechanism for the $D^*_{sJ}(2317) \to D_s\pi^0$ decay, namely decay to a D_s plus a virtual η, where the η is off-shell and mixes with the π^0 via electromagnetic process which does not involve isospin. Cahn and Jackson [14] calculate the mass within potential model while applying non-relativistic vector and scalar exchange forces to the constituent quarks. Barnes, Close and Lipkin [15] consider a quark model explanation unlikely and propose a DK molecular state. Similarly, Szczepaniak [18] suggests a $D\pi$ atom. Also going beyond a simple quark model description, Van Beveren and Rupp [16] explain the low mass for a 0^+ $c\overline{s}$ state as a threshold effect based on unitarized meson model, by analogy with members of the light scalar meson nonet.

In further support of the explanation for the new resonance being an ordinary excited $c\overline{s}$ state, Bardeen, Eichten and Hill [17] and Nowak, Rho, and Zahed [24] couple chiral perturbation theory with a quark model representation in heavy quark effective theory, building on the model described in Ref. [22]. They infer that the $D^*_{sJ}(2317)$ is indeed the 0^+ $c\overline{s}$ state expected in the quark model, predict the existence of the 1^+ partner of this state with a $1^+ - 1^-$ mass splitting equal to the $0^+ - 0^-$ mass splitting, and compute the partial widths for decays to allowed final states.

Godfrey [19] and Colangelo and De Fazio [20] find that the radiative transistion of the $D_{sJ}^*(2317)$ should be significant if it is indeed a $c\overline{s}$ state.

The analysis described in Chapter 3 was motivated by the observation of the $D_{sJ}^*(2317)$ by BaBar. The goals of this analysis are to use the CLEO data to provide independent evidence regarding the existence of the $D_{sJ}^*(2317)$, to shed additional light on its properties, and to search for decays of other new, possibly related states. To do so, we search for the $D_{sJ}^*(2317)$ in the $D_s^+\pi^0$ final state, as well as other decays such as the electromagnetic decays $D_s\gamma$ or $D_s^*\gamma$ and the other hadronic mode for strong decays such as $D_s^*\pi^0$, or the isospin-conserving but Okubo-Zweig-Iizuka (OZI) suppressed [25, 26, 27, 28] decay $D_s\pi^+\pi^-$. If the $D_{sJ}^*(2317)$ is the expected 0^+ $c\overline{s}$ state, the remaining 1^+ state may also be below threshold for decay to D^*K, as suggested in Ref. [17], and thus be narrow enough to be observable in its decays to $D_s^*\pi^0$, $D_s\gamma$ or $D_s^*\gamma$.

1.3 Meson Decay Constants

From a theoretical point of view, purely leptonic decays of mesons provide a means of studying the strong interaction in a relatively simple way. The initial quark and antiquark within the meson annihilate into a virtual W boson, which produces a two-body final state consisting of a lepton (l) and its antineutrino (ν_l). Figure 1.2 shows the Feynman diagram for this leptonic decay. The effect of strong interactions can be isolated due to the presence of only one hadronic current. Experimentally, the final state charged lepton is the clearest signature for a weak process.

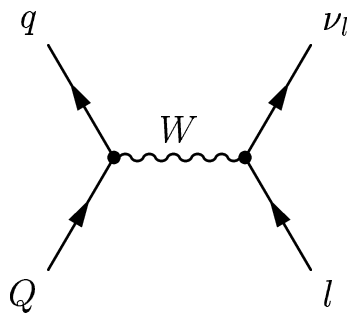

Figure 1.2: Feynman diagram for the leptonic decay $M_{Q\bar{q}} \to l\nu$ of a charged meson.

The decay rate for a charged pseudoscalar meson $M_{Q\bar{q}}$, such as the D^+ $(= c\bar{d})$, D_s^+ $(= c\bar{s})$ and B^+ $(= u\bar{b})$ mesons, ignoring radiative corrections, is given by

$$\Gamma(M_{Q\bar{q}} \to l\nu) = \frac{G_F^2}{8\pi} f_M^2 m_l^2 M (1 - \frac{m_l^2}{M^2})^2 |V_{qQ}|^2, \tag{1.1}$$

where G_F is the Fermi coupling constant, V_{qQ} is the CKM matrix element, f_M is the corresponding weak decay constant, and M and m_l are the masses of the decaying meson and the final state lepton, respectively. The decay constant measures the probability amplitude that the quark and antiquark have zero separation.

The factor $(m_l)^2(1 - \frac{m_l^2}{M^2})$ in Equation 1.1 is a consequence of the helicity suppression which results from the V-A nature of the charged weak interaction. The angular momentum of the D_s meson requires that the spins of the lepton and antineutrino be opposite, that is, they both have to be in right-handed helicity states or both have to be in left-handed helicity states. However, the weak interaction involves left-handed couplings to fermions and right-handed couplings to antifermions, so one of the final state particles has to be in un-preferred helicity state from the standpoint of

the weak interaction. The probability of a particle of a particular chirality being in its un-preferred helicity state is roughly proportional to mass, so the charged lepton will be in the un-preferred helicity state and the decay rate will suffer the helicity suppression factor $(\frac{m_l}{M})^2(1-\frac{m_l^2}{M^2})$. Therefore, the decay rate is suppressed when the m_l is small compared to the mass of the parent meson. The impact of the helicity suppression can be shown in the ratio of the decay rates:

$$\Gamma(D_s^+ \to e^+\nu_e) : \Gamma(D_s^+ \to \mu^+\nu_\mu) : \Gamma(D_s^+ \to \tau^+\nu_\tau) \approx 10^{-5} : 1 : 10 \qquad (1.2)$$

Theoretical predictions for f_{D_s} are in the range of 190 MeV to 356 MeV with a world average of 255 ± 30 MeV [29] and f_D is expected to be about 10% smaller. From unitarity constraints, the CKM matrix elements V_{cs} and V_{cd} are relatively well determined. The decay lifetimes τ_{D_s} and τ_D are also well measured. Hence, measurements of the branching fraction for $D_s \to \mu\nu$ and $D \to \mu\nu$ allow the extraction of the decay constants f_{D_s} and f_D, respectively, using Equation 1.1 and

$$B(D_{(s)} \to \mu\nu) = \tau_{D_{(s)}}\Gamma(D_{(s)} \to \mu\nu). \qquad (1.3)$$

These measurements will provide a more accurate prediction about the decay constants f_{B_s} and f_B from which the poorly known CKM matrix elements V_{ts} and V_{td} can be extracted with measurements of $B_s\bar{B}_s$ and $B^0\bar{B}^0$ mixing. Since the leptonic decay of $B_{(s)} \to l\nu$ is suppressed by a factor of $|\frac{V_{ub}}{V_{cb}}|^2$ (where $V_{ub} \approx 0.002 - 0.005$), the value of $f_{B_{(s)}}$ is beyond the reach of current experiments and thus must be calculated theoretically. Therefore, measurements of f_D and f_{D_s} will provide a check on these theoretical calculations. The goal of the analysis described in Chapter 4 is to provide a more precise measurement of the decay constant f_{D_s}.

1.4 An Overview of This Thesis

This thesis documents measurements pertaining to two distinct physical processes involving D_s mesons, as described in the preceding sections. We first describe in Chapter 2 how we produce, collect, and process our data used to study the physical processes in question. In Chapter 3 we report on the confirmation of the existence of the $D^*_{sJ}(2317)$ meson and on the observation of a new state which we denote the $D_{sJ}(2460)$ meson in the decay mode $D^*_s\pi^0$. We then focus on the leptonic decays of the charmed mesons D_s in Chapter 4.

CHAPTER 2

Experimental Apparatus

This chapter describes the Cornell Electron Storage Ring (CESR) in Section 2.1 and the CLEO detector in Section 2.2 from which we collected data for the analyses in this thesis. The data acquisition and event reconstruction are described in Section 2.3. Finally, Section 2.6 describes how we simulate the detector to study the physical processes involved in the analyses.

2.1 CESR e^+e^- Collider

Heavy mesons are short-lived, such as the D_s meson with a life time of about 4.9×10^{-13} s; therefore they do not stay around for long before decaying if they are created in nature (for example by high energy cosmic rays). In order to study them, we must first create them in a laboratory such as CESR at Wilson Synchrotron Laboratory.

CESR is a symmetric e^+e^- collider with a circumference of 768 meters and about forty feet under the track-and-field facility of Cornell University. The major parts of the CESR collider are the linear accelerator (Linac), the CESR synchrotron, and the storage ring, as shown in Figure 2.1. Einstein's famous equation $E = mc^2$ tells us that mass and energy are equivalent. In other words, we can create massive particles

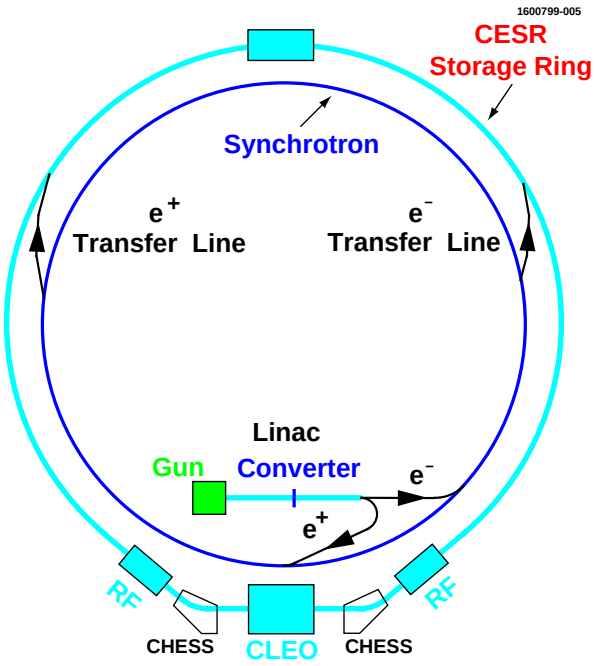

Figure 2.1: The CESR e^+e^- collider.

by colliding lighter particles of sufficient energy. The process of creating mesons at CESR starts with the Linac which produces both electron and positron beams and provides the first stage of acceleration. Electrons are produced by heating a filament inside the electron gun. Approximate 10^{11} electrons are collected, collimated and then bunched together to accelerate to an energy of about 300 MeV by a series of radio-frequency (RF) cavities that generated the electric field for acceleration as they come out of the 30 meter long vacumm pipe. To create positrons, electrons from the heated filament are accelerated to have an energy of about 150 MeV and then are directed into a tungsten target, producing electrons, positrons, and photons. Positrons are selected out by a magnetic field and then accelerated in the remainder of the Linac to an energy of 200 MeV.

The electron and positron bunches from the Linac are injected into the synchrotron for further acceleration till they reach their ultimate energies. The synchrotron consists of 192 bending and focusing magnets as well as 4 linear accelerating cavities. The bending magnets provide a dipole magnetic field to bend the trajectory of the particles in a circle with a radius of $R = p/qB$ where R is the radius of the synchrotron ring, p is the momentum of the particle, q is its charge, and B is the magnetic field strength. The three-meter long cavities keep accelerating the particles as they circle around the synchrotron. In order to maintain the beam bunches in the fixed radius, the magnetic field must be increased to synchronize with the momentum increase of the particles. It is from this synchronization that the synchrotron takes its name. It takes about 4000 revolutions or aobut 1/100 seconds for the particles to reach the desired energies of about 5.29 GeV. Then, the electron and positron bunches are transferred to the

storage ring, at which point the particles are traveling at 99.9999995% of the speed of light.

The electron and positron beams traveling at opposite direction are stored and confined in the storage ring. Like the synchrotron, CESR contains 106 quadrupole focusing magnets and 86 dipole bending magnets. In addition, CESR also has sextupole and octupole magnets to focus the momentum distribution of the beam. As a result of these magnets around the beam pipe that contains the particle beams, we have well focused beams circulating in the storage ring without colliding into the beam pipe walls. However, each electron or positron on average loses about 1.2 MeV of energy per revolution in the form of X-rays, which are known as "synchrotron radiation" because they are a by-product of bending charged particles in a magnetic field. Therefore, the RF cavities in the ring are needed to restore the energy of the particles. The synchrotron radiation deposits energy in the vacuum chamber wall which has water circulating to carry away the heat generated. Some of the synchrotron radiation photons are collected by the Cornell High Energy Synchrotron Source (CHESS) facility for X-ray research in the areas of physics, chemistry, biology, environmental science, and material science. Since both the electron and positron bunches are stored in the same ring, electrostatic separators are used to displace the electron and positron orbits so that the collisions of the multiple bunch beams occur only at the south interaction region surrounded by the CLEO detector.

There are nine groups of particles, called trains, evenly spaced around the storage ring. At the beginning of the CLEOII phase of the experiment described in this thesis, each train contains only one bunch of particles, but later more bunches were

added to allow more particles in the storage ring as so to increase the frequency of collisions. At the end of CLEOII.V phase, CESR operated with 9 trains of 4 closely spaced bunches in each beam. The electron and positron bunches with equal beam energy are brought to collision at a small horizontal crossing angle (± 2 mrad) and each bunch is 2 cm long, 0.3 mm wide, and 8 μm high at the interaction point. Each crossing in which a collision between an electron and positron results in particles with some momenta perpendicular to the beam is referred to as an "event".

One of the main parameters as well as a measure of performance of an accelerator is the instantaneous luminosity $\mathcal{L}$, which is the number of collisions for each cm^2 per second, defined as

$$\mathcal{L} \equiv n f \frac{N_{e^+} N_{e^-}}{A}, \tag{2.1}$$

where f is the frequency of revolution of the particles, n is the number of electron (or positron) bunches in the beam, N_{e^+} and N_{e^-} are the number of electrons and positrons in each bunch, repectively, and A is the cross-sectional area of the beams. The highest instantaneous luminosity achieved during the time period of data taking for the data sets used in this thesis was 8.3×10^{32} cm^{2}s^{-1}. The total number of collisions that occur is measured by integrating the instantaneous luminosity over time. The number of events N for a particular physical process occurs is given by

$$N = \sigma \left[\int \mathcal{L} dt \right], \tag{2.2}$$

where σ is the cross-section for the process in question. Figure 2.2 shows the total cross-section for $e^+e^- \rightarrow$ hadrons at center-of-mass energies around 10 GeV. The peaks at this plot are known as Upsilon (Υ) resonances, and the hadronic background

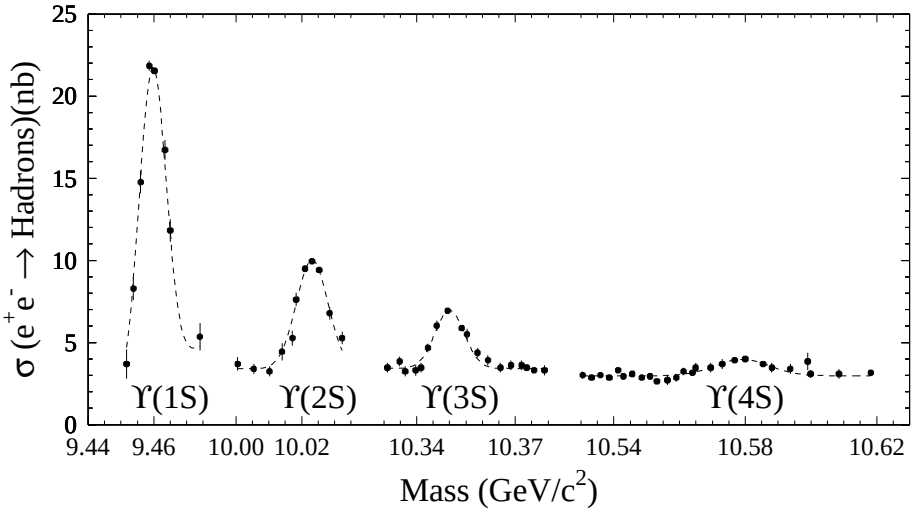

Figure 2.2: The hadronic cross-section in the Upsilon region.

underneath the peaks is often referred to as the "continuum background" for the resonances.

CESR was designed to run over a range of energies to provide symmetric electron and positron beam collisions. During the operation of CLEO II and II.V data taking, it ran at or just below a center of mass energy of 10.58 GeV at which the e^+e^- collision produces a bound state of a b and $\bar{b}$ quark known as the $\Upsilon(4S)$ resonance, which was first observed at CLEO. The total hadronic cross section at the $\Upsilon(4S)$ resonance is about 4 nb (1b=10^{-24}cm^2). About one-fourth of this is due to the production of $\Upsilon(4S)$, and the rest is from the continuum production of lighter quark-antiquark pairs: $e^+e^- \to q\bar{q}$ where q stands for a u, d, s, or c quark. Note that the cross section for the continuum production of charm is $\sigma(e^+e^- \to c\bar{c}) \approx 1.2$ nb. The two analyses described in Chapter 3 and 4 are based on data taken from 1990 to 1999, with this continuum production involving the $c\bar{s}$ mesons. The data sample used in these two

analyses consists of an integrated luminosity of 9.13 fb^{-1} at a center-of-mass energy near 10.58 GeV (referred to as on-resonance), and 4.35 fb^{-1} about 60 MeV below the $\Upsilon(4S)$ (referred to as off-resonance).

2.2 The CLEO Detector

With mesons created from the electron-positron collisions provided by CESR, we need instrumentation to detect and record these events in order to study them. To help detect and measure the properties of these particles and their subsequent decays, the CLEO detector was built.

CLEO is a general purpose collider detector with cylindrical geometry and with a solid angle coverage of almost 4π, and is described in detail in Refs. [30, 31]. The analyses in Chapter 4 and 3 rely heavily on the detector's ability to measure the momentum of charged tracks and the energy of electromagnetic showers, as well as its ability to identify tracks as coming from leptons or hadrons.

The CLEO detector is referred to as "a detector", however, it is actually a collection of different types of sub-detectors. A side view of the CLEO detector is shown in Figure 2.3. We will briefly discuss the sub-detectors in the following sections in the order that a particle created at the interaction region will encounter: the Precision Tracker, the Vertex Detector, the main drift chamber, the Time of Flight Detector, the Electromagnetic Calorimeter, and the Muon Chamber.

We use the following coordinate system as we describe the detector. The z-axis points along the direction of the positron beam (west), and the polar angle θ is

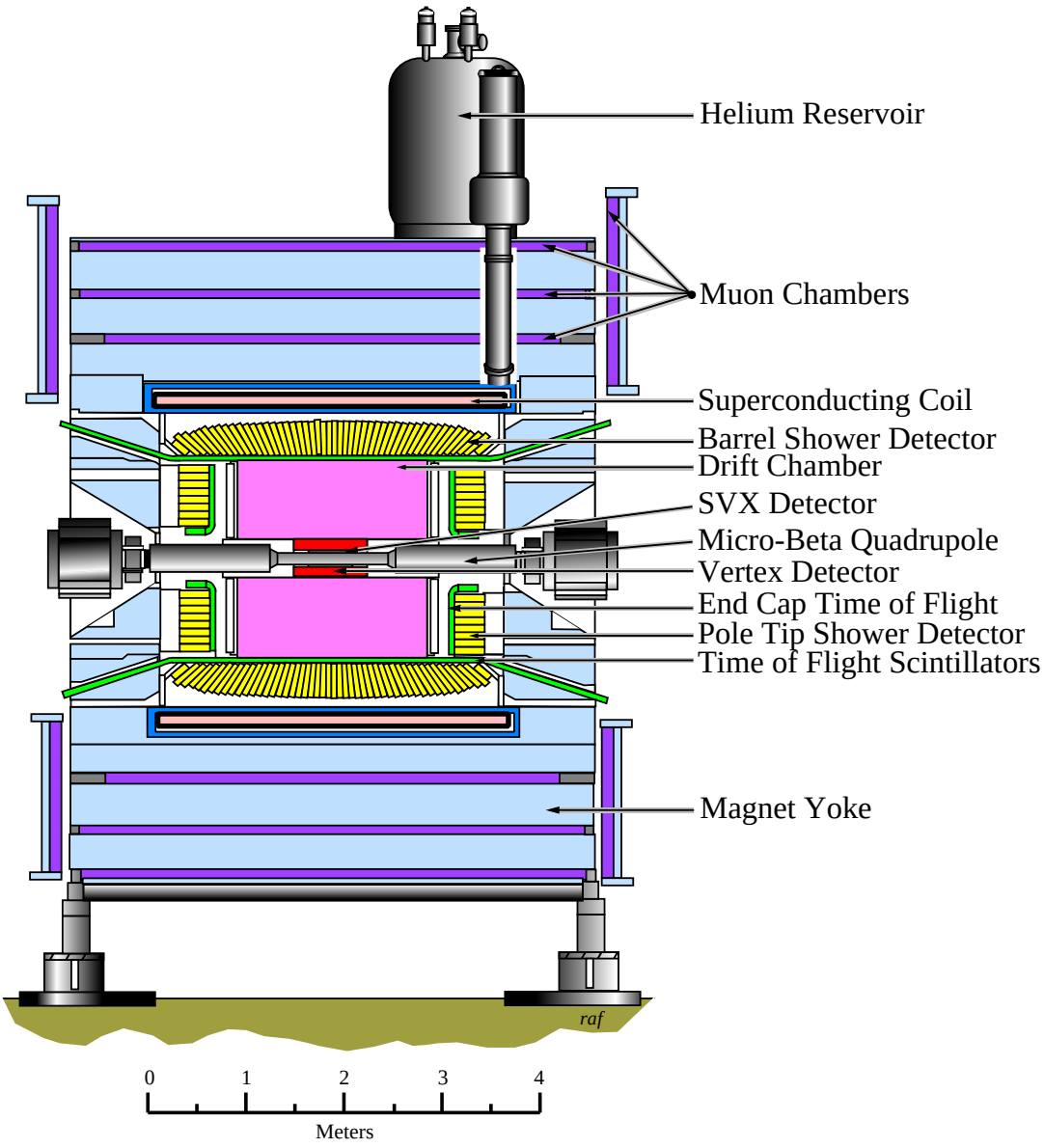

Figure 2.3: The side view of the CLEO II.V detector

defined with respect to the z-axis. In a cylindrical coordinate system, r is the distance from the beam line, $\phi = 0$ corresponds to the northward (onward) direction at the interaction point. The CLEO detector is symmetric about z=0 with respect to θ and also symmetric in ϕ continuously.

2.2.1 The Tracking System

The tracking system in the CLEOII configuration was comprised of a six-layer straw tube chamber (PTL) just outside of a 3.5 cm radius beryllium beam pipe, followed by a 10 layer hexagonal cell drift chamber (VD) and a 51 layer square cell drift chamber (DR), immersed in a 1.5 T magnetic field generated by a superconducting solenoid. The layout of this tracking system covers about 95% of the solid angle and is shown in Figure 2.4.

Precision Tracker

Particles from the interaction point first pass through the beam pipe and enter the innermost layer of CLEOII's tracking system, which is the Precision Tracker (PT). It consists of six layers of aluminized mylar tubes with a gold-plated tungsten sense wire strung in each tube. There are a total of 384 straw tubes, and each layer of tubes with various diameter is arranged in the pattern as in Figure 2.4 by the label "PTL" for Precision Tracking Layers. The PT detects charged particles by using the ionization electrons and an electric field. The wires in the tubes are held at high positive voltage with the tubes grounded, which produces an electric field within the tube in a direction that pushes electrons toward the wire. A gas mixture of 50%

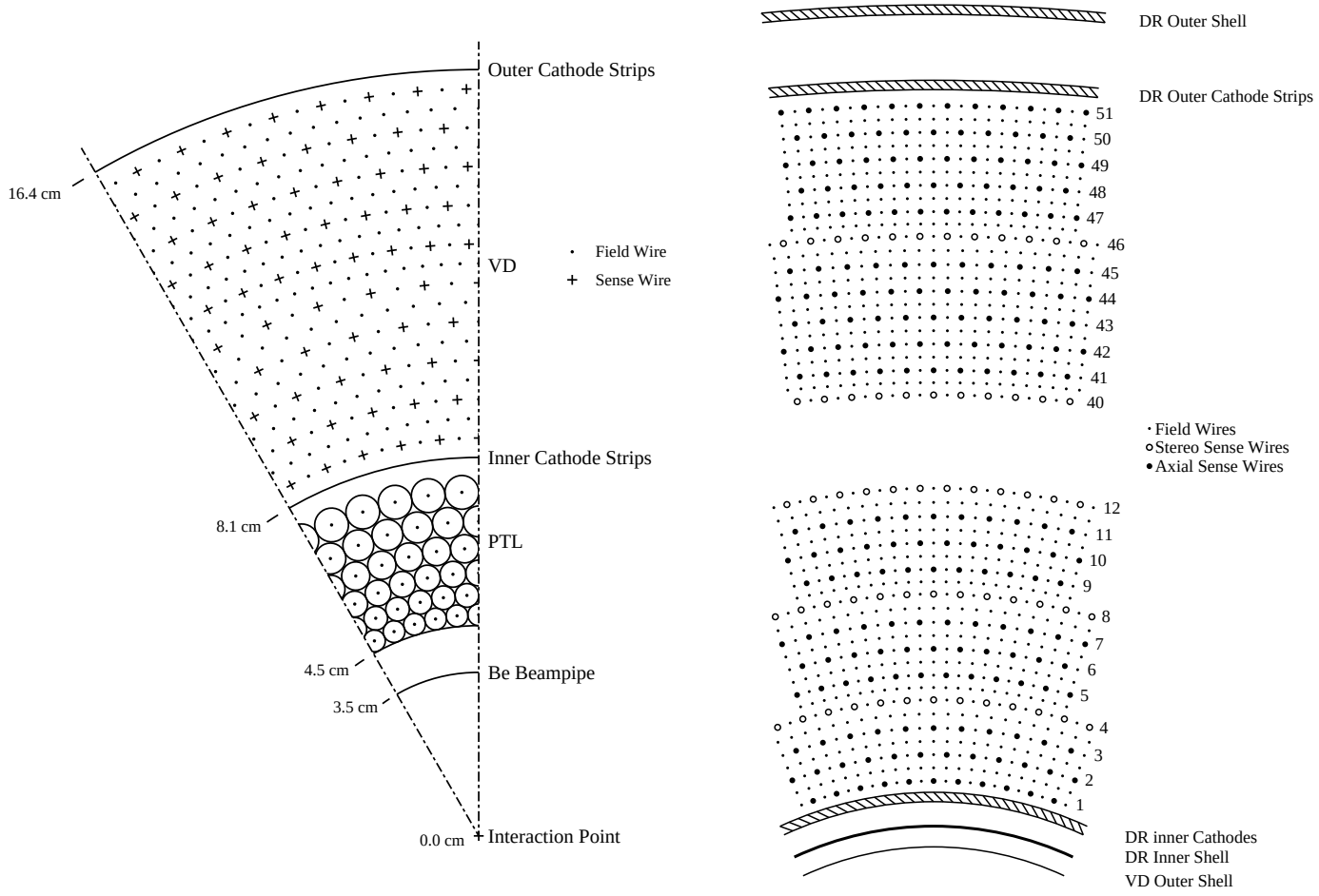

Figure 2.4: The left plot shows a layout of the Precision Tracker and Vertex Detector in CLEO II. The right plot shows the cross-sectiional view of the cell structure for the main drift chamber

argon and 50% ethane flows throught the tubes. In April 1992, the gas mixture was switched to dimethyl ether to produce better position resolution. A charged particle traveling through the tube ionizes the gas particles in the tube, creating liberated electrons which follow the direction opposing the electric field and drift toward the wire. Collisions with gas molecules keep the average velocity of the electrons roughly constant. Near the surface of the wire the electric field grows to a level that electrons are accelerated quickly enough to ionize the gas molecules they encounter. This creates a chain reaction known as an "avalanche" as they get closer to the wire. When the electrons reach the wire, they produce a measurable current in the wire, allowing a readout of the electrical signal that includes time and accumulated charge (pulse height). The wires are called "sense wires" because they indirectly detect particles passing through. The PT provides information about the $r - \phi$ position of a charged particle with a resolution of about 100 μm.

CLEOII.V Silicon Vertex Detector

In 1995, the CLEOII detector was upgraded to the CLEOII.V configuration for which the beam pipe and straw tube chamber were replaced by a 2.0 cm radius beam pipe plus three concentric layers of silicon (Si) strip detectors each with double-sided readout. The end and side views of the silicon vertex detector (SVX) are shown in Figure 2.5. The 300-μm-thick double-sided silicon wafers were mounted directly to the beam pipe. The electrons and holes created by a charged particle along its traversing path drift in opposite directions and are collected on the sensing strips on the opposite sides of the silicon wafer as a result. The aluminum readout strips are

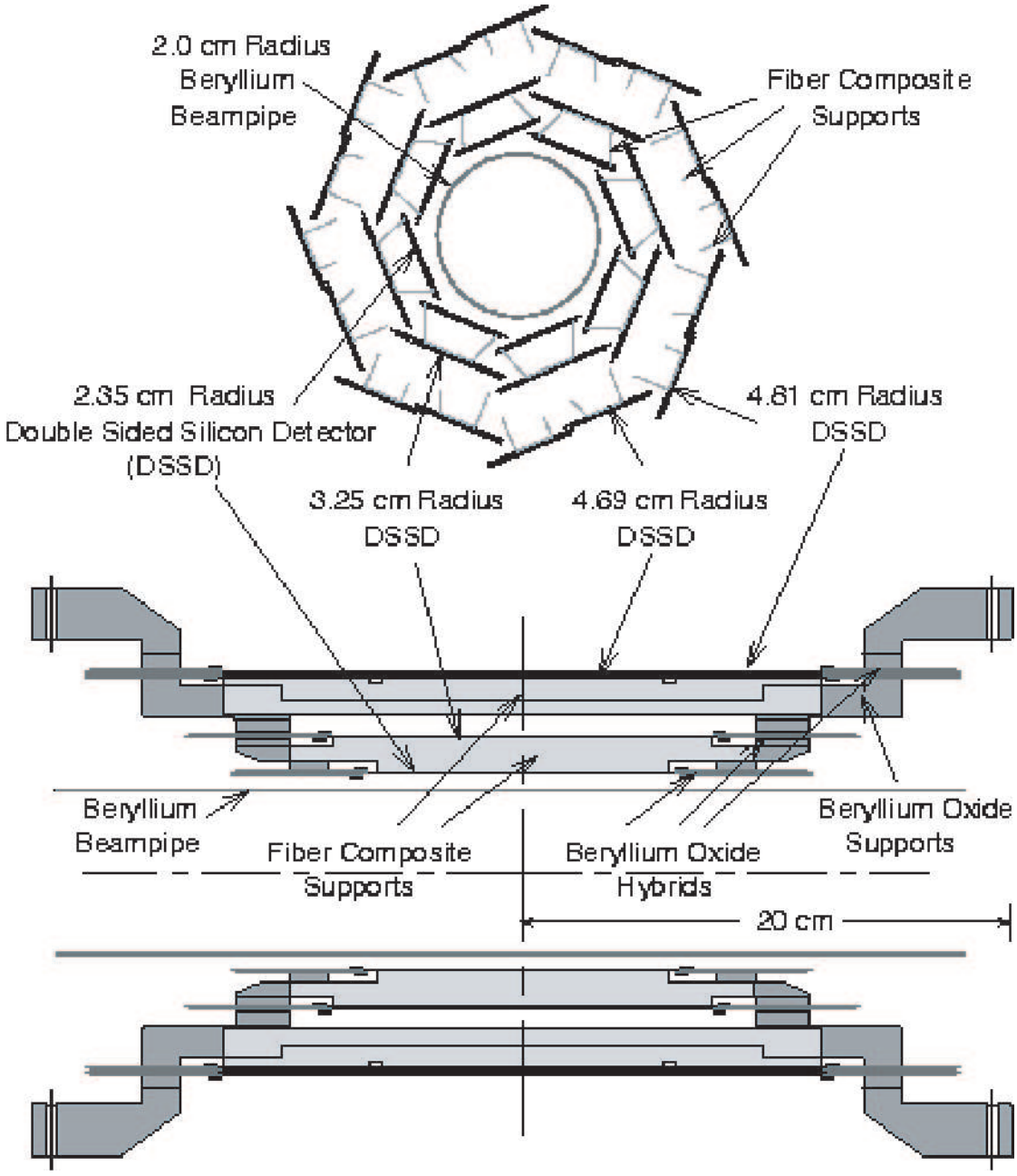

Figure 2.5: End-on (top) and side (bottom) cross-sectional views of the silicon vertex detector in CLEO II.V

capacitively coupled to the sense strips.

Vertex Detector

Outside the PT is the Vertex Detector (VD) which operates with the similar principle as the PT. Unlike the PT, the VD is an open cell drift chamber that consists of wires and two sheets of cathode strips, and its volume is filled with a 50-50 gas mixture of argon and ethane. The VD has a total of 800 nickel-chromium sense wires and 2,272 aluminum field wires arranged to form 10 layers of hexagonal cells. The field wires surround the sense wires to shape the electric field, replacing the function of the tubes in the PT. The sense wires are read out at both ends, and a charged particle's z position can be determined from the different amount of charge that accumulates at each end of the wire (known as the "charge division" method). Therefore, VD provides information about a charged particle's position in z as well as the $r-\phi$ plane. The average resolution of the VD was about 1.7 cm in z and 150 μm for $r-\phi$. The two cathodes are made of sheets of mylar to which aluminum foil has been applied, sitting inside the innermost and outside of the outermost layer of wires. The foil is segmented in ϕ and z into separate "pads". When a particle induces a negatively-charged avalanche on a sense wire near a cathode, a negative "image charge" of the ion cloud develops on the cathode pads nearest the avalanche. The z position of the avalanche and hence the particle is determined by analyzing the distibution of charge on the pads. The segmented cathode planes are instrumented to also provide z position measurements for charged particles with a typical resolution of 750 μm.

Main Drift Chamber

The main drift chamber (DR) outside the VD in CLEOII or the SVX in CLEOII.V is the largest and most important tracking device in the CLEO detector. The drift chamber has an inner radius of 17.5 cm, an outer radius of 95 cm, and is 2.15 m long in length, consisting of sense wires, field wires, and cathodes arranged as shown in the plot at the right of Figure 2.4. A total of 12,240 gold-plated tungsten sense wires are arranged in 51 layers of nearly square cells consisting of 36,240 field wires surrounding them. The field wires around the inner 40 layers are made of gold-plated aluminum with the remainder made of gold-plated copper-beryllium. The wires are strung between two aluminum endplates held apart at their outer edge by a cylinder of composite panels. The wires are insulated from the endplates with plastic bushings. The sense wires are held at high voltage, and the field wires and cathodes are grounded. In the CLEOII.V upgrade, a helium-propane gas mixture replaced the 50-50 argon-ethane mixture previously used in the main drift chamber. Multiple scattering is considerably reduced for particles going through the helium-propane mixture which also improves the charge collection efficiency from the outer part of a drift cell by having more uniform drift characteristics. The DR operates based on the same principle as in VD with a difference in the arrangement of wires. Forty of the 51 layers strung parallel to the z-axis are known as axial layers, while eleven sense layers are stereo layers which are offset about 3°-7° from the z-axis to provide z information throughout the volume of the detector. To determine the z position of the particle at the stereo layer, the particle's $r - \phi$ position is predicted first using the axial layers and is used to match the $r - \phi$ information from the stereo wires.

The inner and outer radii of the drift chamber are covered with longitudinally and azimuthally segmented cathodes to provide precise measurements of the z position of most tracks. Each electrical signal from the wire is called a hit on the wire. The average $r - \phi$ resolution for a DR hit was about 150 μm and the z resolution of the stereo layers varied from 3 to 5 mm.

Track Reconstruction

Information from the PT, VD, and DR is used together to determine the paths that charged particles traveled through the detector. A pattern-recognition algorithm employs all the $r - \phi$ and z information, grouping the hits to form tracks. The tracking system is inside an axial magnetic field and so charged particles follow a helical path with positive charges curling in the $+\hat{\phi}$ direction and negative charges curling in the $-\hat{\phi}$ direction for the magnetic field oriented along the $-z$ direction. We can determine the transverse momentum $P_\perp$ by measuring the curvature of the track as they are related by

$$P_\perp = qBa, \tag{2.3}$$

where q is the magnitude of the particle's charge, B is the magnitude of the magnetic field, and a is the radius of curvature. A measurement of a particle's total momentum can be obtained by using $P_\perp$ and the particle's polar angle θ. The track candiates are fit with helical trajectories, corrected for energy loss in material. This process is called track reconstruction. The momentum resolution for reconstructed tracks is approximately

$$(\frac{\sigma_P}{P})^2 = (0.0015P)^2 + (0.0055)^2, \tag{2.4}$$

where P is the track's momentum in GeV/c in the $r-\phi$ plane. For particles with momentum of 2 GeV/c, this gives a resolution of 0.6 %. The angular resolution of tracks is 1 mrad in ϕ and 4 mrad in θ.

2.2.2 The Time-of-Flight System

Beyond the tracking system was located a 5 cm thick plastic scintillation counter system for time-of-flight measurement and triggering. The Time of Flight (TF) system is divided into three parts to provide better solid angle coverage. The cylindrical arrangement of the scintillators is the "barrel" section which sits just outside the DR. There are 64 rectangular (2.8 m $\times$ 10 cm $\times$ 5 cm) blocks, also called counters, of special plastic that has been doped to make it scintillate, or emit light, when particles pass through it. The light signal is read out on each end by photomultiplier tubes which are connected to the counters with lucite light pipes. The two "endcap" sections consist of 28 wedge-shaped counters about 58 cm long and 5cm thick, sitting outside each of the DR endplates. The endcap counters are read out with photo multiplier tubes attached directly to the narrow ends of the counters. The barrel and endcap sections provide 97% solid angle coverage, and the time resolution of the TF system is about 150 ps.

2.2.3 Electromagnetic Calorimeter

Outside the TF is an electromagnetic calorimeter, known as the Crystal Calorimeter (CC), which is a very important part of the CLEO detector for the analyses in this

thesis. The CC resides inside the magnet coil, consisting of 7,800 thallium-doped cesium iodide (CsI) scintillation crystals covering 95% of the solid angle. The CC is divided into a barrel and two endcap sections. The barrel calorimeter consists of 6144 tapered CsI(Tl) crystals 30 cm in length and 5 cm square in cross section, arrayed in a projective geometry, with their long axis oriented radially with respect to the e^+e^- interaction point. An additional 1656 crystals with about 16 radiation lengths were deployed in two endcaps to complete the solid angle coverage.

The high density of the crystal (4.53 g/cm^3) makes it probable that particles will lose energy as they traverse and interact in the calorimeter. The interactions taken place inside the crystal material are particle species dependent. All charged particles deposit energy via electronic excitation, and the reabsorption of those electrons in the crystal results in scintillation light. Additionally high energy electrons have a high probability of interacting with the atomic nuclei, leading to emission of bremsstrahlung photons. These photons can also undergo interaction with the atomic nuclei resulting in e^+e^- pair production. This process generates a cascade of electromagnetic showers. Lower energy electrons, positrons, and photons cause excitations of the electronic structure of the atoms that lead to the scintillation light. High energy photons can also initiate electromagnetic showers in processes similar to high energy electrons. Hadrons can interact via the strong interaction with the nuclei of the cyrstal. Some of the scintillation light makes it to the back of the crystal for detection by four silicon photodiodes mounted on the crystal. A "shower" is the accumulated light associated with the Bethe-Bloch formula in Equation 2.5 for the normal energy loss for interactions with atomic electrons in the crystal material.

From now on, we refer to a shower as a cluster of measured energy that has been deposited through the interactions of a particle traversing the calorimeter.

Showers are reconstructed by first converting the amount of light detected into an estimate of energy deposited in the crystal, and then locating the clusters of adjacent and near-adjacent crystals with energies above threshold. The highest-energy crystal in each cluster must have a signal above 10 MeV. The shower energy is the sum of energies from that crystal and its neighboring crystals in a cluster. The photon energy resolution is 3.8% at 100 MeV and 1.5% at 5 GeV in the barrel. The position of the shower can be used to determine the flight direction of neutral particles under the assumption that they are produced at the interaction point. It is calculated as the energy-weighted mean of the position of the center of each contributing crystal in the cluster. The angular resolution for barrel photon showers is 11 mrad at 100 MeV and 3 mrad at 5 GeV. The endcap performance is degraded by the presence of the aluminum DR endplates and electronics in front of the crystals. The excellent energy and angular resolution of the calorimeter is critical for the reconstruction of $\pi^0 \to \gamma\gamma$ decays as well as of single low-energy photons such as those emitted in the $D_s^{*+} \to D_s\gamma$ transition.

2.2.4 The Solenoidal Magnet

The superconducting solenoidal magnet coil outside the barrel calorimeter generates a 1.5 Tesla magnetic field parallel to the beam axis. The coil has a diameter of 3 meters and is 3.5 meters in length. It carries a current of 3,300 amps and stores 25 MJ of energy, and it is cooled down to superconducting temperatures with liquid helium.

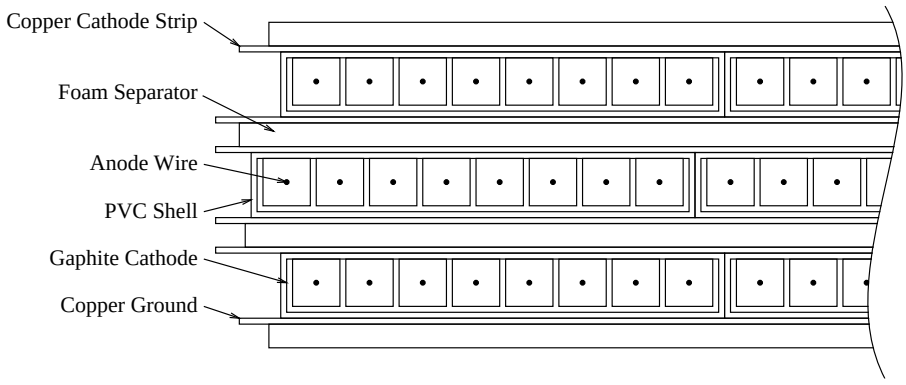

Figure 2.6: A cross-section of a muon chamber super-layer.

Three layers of 36-cm-thick iron flux return for the magnet also serves as part of the absorber for the muon identification system. The magnetic field is uniform to within 0.2% over 95% of the tracking volume. The tracking software assumes a uniform magnetic field.

2.2.5 The Muon Chambers

Outside the magnet is the muon identification system consisting of proportional counters placed at increasing depth in steel absorber. The muon chambers (MU) operate like the tracking chambers. A cross-section of the muon super-layer is shown in Figure 2.6. Each super-layer consists of three layers of staggered proportional wire chambers of 4 m long, 8.3 cm wide, and 1.0 cm tall and oriented with its long axis parallel to the z-axis. The sections are divided into eight separate volumes with a piece of plastic

that runs the length of the section with a comb-like profile. The plastic is coated with graphite to provide a field cage on three sides for silver-plated copper-beryllium wires which run down the center of each of the eight channels. Orthogonal copper pickup strips, similar in idea to the VD and DR cathodes, provide the fourth side of the field cage and give z information. The wires are held at high voltage in a volume filled with a 50-50 mixture of argon and ethane. Signals from the wires are read out at both ends and use charge division to give more z information. This kind of tracking chamber is known as a "plastic streamer counter". Three barrel layers of counters are placed in the magnet return iron at depths of 36, 72, and 108 cm, corresponding to 3, 5, and 7 nuclear interaction lengths (also known as the absorption length, the average distance a particle travels in a material before scattering off a nucleus). There is one super-layer in the endcaps at a depth of about 7 absorption lengths. The total solid angle coverage of the barrel and endcap muon chambers is 85%. The spatial resolution of the muon chambers is 5.7 cm for particles which reach the outer layer of barrel counters.

2.3 The Trigger and Data Acquisition System

The electron and positron trains pass each other with a frequency of 390 kHz such that with 9 trains the crossing frequency is about 3.5 MHz. Although not every crossing produces a collision and not every collison produces physical processes of interest, the rate is still too high for the data acquisition system to read out every collision event. CLEO employed a sophisticated system of electronics and software

filters called the trigger system to examine each event as it happens and determine if that event gets read out. The trigger system is driven by the timing system, which coordinates the readout of events with the bunch crossing. The timing system also enables, disables, and resets readout from all detector components, based on results of the trigger system.

The trigger operates on several levels, each with increasing complicated information from the detector to make its decision. The first front end is a hardware trigger called level-zero trigger (L0). L0 takes about 30 ns to make a decision based on the information from the VD, TF, and CC. It reduces the event rate from the 3.5 MHz bunch-crossing frequency to the data-taking rate of about 20 kHz. If an event passes the L0 trigger, the gates to the detector electronics are disabled so that no new data are read in. The next level is the level-one trigger (L1) which looks at the DR data as well as those from L0. It takes about 1 μs to make a L1 decision, which slows the rate to about 25 Hz. The level-two trigger (L2) accepts events from L1 and uses additional information from the VD and DR to decide if an event should read out or not. L2 takes about 30-50 μs to make a decision, and slows the rate to a few Hz. After L2, the hardware trigger is reset, and CLEO is ready for data-taking again. If any of the levels fail, the system goes back to ground zero. A software trigger called L3 takes the event passed by L2 and then either reject or accept the event based on more sophisticated reconstruction algorithms. Events such as those from cosmic rays or interactions of the beam with residual gas molecules in the beampipe are rejected by L3 before they are permanently recorded. L3 rejects about half of the events passed from L2.

2.4 Event Reconstruction

The raw data recorded must be processed by software packages to reconstruct tracks and showers for the events. The software programs that processes the data are called `Pass1` and `Pass2` which includes a collection of processors and routines to perform event reconstruction from raw data collected from different components of the detector. An event reconstruction includes both track and shower reconstructions, which have already been discussed at some level in previous sections. The track reconstruction includes a track parameter fitting based on an implementation of the Kalman filter method that accounts for multiple scattering and energy loss.

`Pass1` performs fast classification of the raw data events and runs online to provide real-time feedback about the performance of the detector during data taking for data quality control. It only processes one-tenth of all the events collected with fast reconstruction. `Pass2` processes all events for more detailed and accurate event reconstruction. All data that are used for physics analyses in CLEO have been processed by `Pass2`.

2.5 Particle Identification

We make use of the information collected from different components of the detector to identify particles.

2.5.1 Hadron Identification Using $\frac{dE}{dx}$

The drift chamber provides measurements of not only the momentum of a charged particle but also the specific ionization ($\frac{dE}{dx}$) used for particle identification for electron, pion, kaon, and proton. The mean ionization loss per unit length of a particle trajectory in gas depends on the particle's velocity as given by the Bethe-Bloch formula [1]:

$$< \frac{dE}{dx} >= -(4\pi N_A r_e^2 m_e c^2)\frac{Z}{A}(\frac{z}{\beta})^2[\frac{1}{2}log(\frac{2m_e c^2\beta^2\gamma^2 T_{max}}{I^2}) - \beta^2 - \frac{\delta}{2}] \qquad (2.5)$$

where N_A is the Avogadro number, r_e is the classical electron radius, Z and A are the atomic number and atomic mass of the gas medium, z is the particle charge in electron units, m_e is the mass of an electron, βc is the particle's velocity, $\gamma = \frac{1}{\sqrt{1-\beta^2}}$ is the relativistic factor, T_{max} is the maximum kinetic energy that can be transferred to a free electron in a single collision, I is the mean excitation energy, and δ is the density effect correction. Experimentally, the linear density of energy deposited in the gas by the passage of a charged particle, dE/dx, is estimated from the integrated charge of the hits it caused in the DR. This quantity, when combined with the track's measured momentum, gives the DR some power to discriminate between particles of different mass, and thus some particle identification abilities. Figure 2.7 shows the expected curves for various particle types versus measured dE/dx as a function of momentum.

To perform particle identification using dE/dx, we cut on the difference between the mean of the lowest half of the pulse heights (thus truncating the Landau-like high-side tail of the distribution) and the expected pulse heights for a given particle type

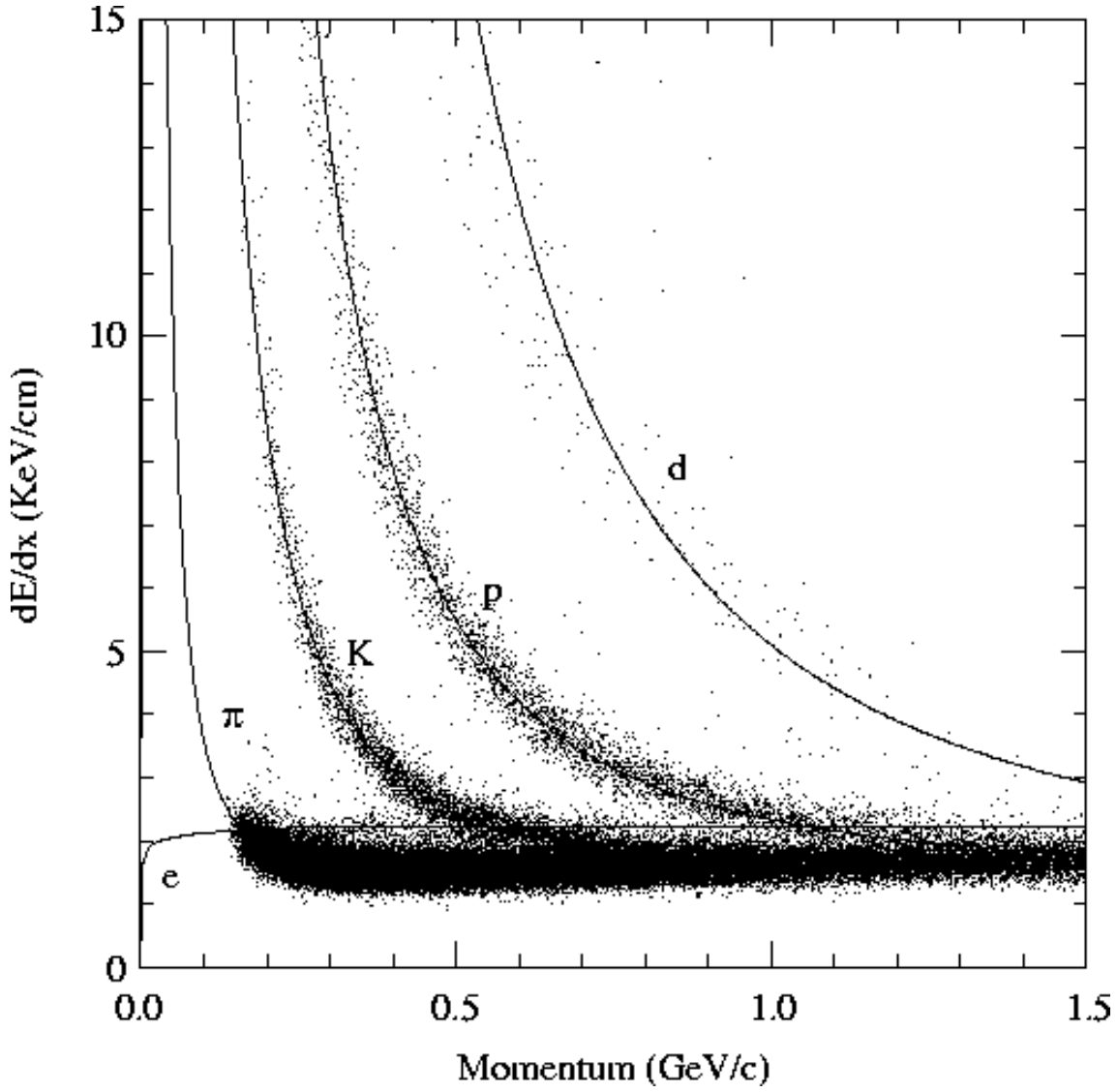

Figure 2.7: Measured dE/dx as a function of momentum. The solid lines represent theoretical curves for various particle types.

divided by the expected resolution for that pulse height and number of hits. For kaon or pion identification in the two analyses described later, we use the CLEO quantity `SGKADI` or `SGPIDI`, the number of standard deviations away the dE/dx measurement for a track is from the expected value for a kaon or pion, respectively.

2.5.2 Photon Identification

The CC is the only detector that detects photons at CLEO. Electrons and photons interact electromagnetically in the crystal and deposit almost all of their energy through a cascading process of bremsstrahlung and pair production. Muons and hadrons are not stopped by the bremsstrahlung processes as easily by virtue of their higher mass, and usually travel through the calorimeter with only a small amount of energy loss due to ionization. Charged hadrons are not only subject to the electromagnetic processes, but also can interact via the strong force with the nuclei of the CsI(Tl) cyrstals, producing secondary hadrons and causing non-localized showers. Thus, the energy distribution or shower shape of the shower helps distinguish photons and electrons from other particles. The shower shape is measured by a quantity called E9/E25 which is the ratio of the energy measured in the 9 crystals (3×3) surrounding and including the highest-energy crystal to the energy measured in the 25 surrounding crystals (5×5). Showers from photons and electrons tend to have an E9/E25 value closer to 1 than the hadrons.

To distinguish photons showers from electron showers, we look for reconstructed tracks that point to the shower. This process is called track-shower matching. Electromagnetic showers that have tracks pointing to them can be ruled out as photon

showers since photons do not leave tracks in the tracking chambers.

2.5.3 Muon Identification

Muons do not interact via the strong force, and they do not lose much energy to bremsstrahlung processes due to their high mass. Therefore, muons are the only charged particles capable of penetrating the magnet yokes, making them easy to identify with the muon chambers. Tracks are identified as muons by matching hits in the MU chambers to the extrapolated trajectory of a DR track. To be a match, there must be hits in at least two out of the three counters in that layer. The variable `DPTHMU` records how many interaction lengths of iron the particle penetrated to reach the outermost matched layer. Particles must have at least 1, 1.4, and 1.8 GeV/c of momentum to reach a `DPTHMU` of 3, 5, and 7, respectively. Requiring higher values of `DPTHMU` gives a lower efficiency in identifying muons but decreases the likelihood that the track is not a muon, known as the "fake rate".

2.5.4 Electron Identification

The CC can be used to identify electrons as discussed in Section 2.5.2. Furthermore, since the electrons have a very small mass (0.5 MeV/c^2), the relationship $E^2 = m^2c^4 + p^2c^2$ becomes E=pc to a good approximation and E/p is very close to 1 for electrons. In light of this, we obtain the value of E/p from taking the ratio of the energy measured in the CC to the momentum measured in the DR. CLEO developed the Cornell Electron Identification (CEID) package to identify electron candidates.

CEID examines each track and combines track and shower information to produce a log-likelihood to separate electrons from other charged particles. This log-likelihood variable `R2ELEC` is defined as

$$R2ELEC = \sum_i ln(\frac{P_{ei}}{P_{\not e i}}), \tag{2.6}$$

where P_{ei} is the probability that the track/shower was produced by an electron, and $P_{\not e i}$ is the probability that it was not produced by an electron. The sum is over several variables such as dE/dx, E9/E25, E/p, the time of flight, the track-shower match distance, and the size of the shower. The CEID likelihoods are calibrated from radiative bhabha electrons that have been embedded in hadronic events. A high value of `R2ELEC` means that it is more likely that track was produced by an electron.

2.6 Monte Carlo Simulations for Physics

We use simulated data to determine detection efficiency, estimate background, or extract background and signal shapes for the physical processes studied in this thesis. The simulated event samples are called Monte Carlo (MC) because of the use of random numbers in generating possible outcomes for the processes.

The production of Monte Carlo samples involves three stages. The first is to generate the physical processes using the `QQ` e^+e^- interaction generator which produces Monte Carlo events with a list of particles (with their corresponding four-momenta) created in an e^+e^- interaction at 10.58 GeV. It simulates events for $e^+e^- \rightarrow q\bar{q}$ where q can be a up, down, strange, charm, or bottom quark. The quark fragmentation simulation uses an interface to the JETSET software package that models quark and

gluon hadronization. The subsequent decays of unstable particles are simulated based on the probabilities of decays obtained from a decay table being updated periodically to reflect our current best knowledge.

The second stage of the Monte Carlo generation is to propagate the list of particles to a CLEO event simulation program called CLEOG based on CERN's GEANT software program that simulates the passage of particles through the detector material. As the particle propagates through the detector, a random number is generated to determine if the particle interacts with the detector material. If it does, another random number is generated to determine its effect on the particle. Detector noise is also simulated using either calibration data or hits from random trigger events when no colliding physics events were present.

Finally, the simulated events are processed with the same reconstruction programs as used for real data.

CHAPTER 3

The Observation of Two New Particles

This analysis was motivated by the recent discovery by the BaBar Collaboration [13] of a narrow state at 2.32 GeV/c^2, the $D^*_{sJ}(2317)^+$, that decays to $D_s^+\pi^0$. It was suggested to be the missing $J^P = 0^+$ P-wave $c\overline{s}$ meson as discussed in Chapter 1 even though its mass is much lower than most theoretical predictions. If so, the other missing P-wave $c\overline{s}$ state with 1^+ might also be less massive than predicted, and thus be narrow enough to be observable in its decays to $D_s^*\pi^0$, $D_s\gamma$ or $D_s^*\gamma$. The goals of this analysis are to first confirm the $D^*_{sJ}(2317)^+$ if it exists, to look for its other decay modes, and then to search for the missing 1^+ state.

3.1 General Approach

A typical approach to search for a new particle is to look at the mass distribution for the most probable decay of the particle, and then perform a fit to the peak to obtain the mass of the particle in question. In this case, we search for the new resonance in the decay modes $D^*_{sJ}(2317)^+ \to D_s^+\pi^0$. However, we look at the mass difference of the charmed mesons rather than its mass directly in this analysis, namely, $\Delta M(D_s\pi^0) = M(D_s\pi^0) - M(D_s)$. By fitting to the mass difference, we get better resolution and

more precise determination of the mass since some of the mis-reconstructions of the heavier daughter meson (D_s) in the decay will get canceled out. After we establish the existence of the new particle with a mass of 2.13 GeV/c^2, we explore its properties by searching for its decays into other particles with well-known properties.

3.2 Confirmation of $D^*_{sJ}(2317)^+ \to D^+_s\pi^0$

The search for the $D^*_{sJ}(2317)$ was carried out by reconstructing the $D^+_s\pi^0$ state with $13.5 fb^{-1}$ of CLEOII and II.V data. We fully reconstruct the decay chain $D^*_{sJ}(2317)^+ \to D^+_s\pi^0$, $D^+_s \to \phi\pi^+$, where the ϕ candidates are reconstructed via the decay mode $\phi \to K^+K^-$. Charge conjugation is implied throughout this chapter.

3.2.1 Event Selection Criteria

We first require that an event satisfies the hadronic event classification criteria. We define a "good" reconstructed track as one that satisfies the following track quality requirements. It is not parallel to the beam axis and thus did not cross most of the stereo layers in the DR or the cathodes, and did not project to the edge of the drift chamber. It has a good track fit, and projects back to the interaction region so as to be classified as a good primary or secondary track, with the impact parameter with respect to the beam spot smaller than 0.002 meters and the z coordinate at point of closest approach to the origin smaller than 0.05 meters. If dE/dX is available, we require that dE/dX information is consistent with the track hypothesis (π/K) within 2.5 standard deviations. We further require that the invariant mass of the

oppositely charged kaon pair $M_{K^+K^-}$ is consistent with ϕ mass within ± 10 MeV/c^2 (2.5σ) of $M_\phi = 1.0195$ GeV/c^2 [32]. The π^0 candidates are reconstructed using the decay $\pi^0 \to \gamma\gamma$. The directions and energies of the two photons are adjusted with a kinematic fit with two-photon invariant mass constrained to the π^0 mass. To reduce background from random photons, we require that each of the photons from the π^0 decay must have energy greater than 100 MeV in the good barrel region: $|cos\theta| < 0.71$. The invariant mass of the two photons is within $-3.0\sigma < M(\gamma\gamma) - M(\pi^0) < 2.5\sigma$ where σ is the number of standard deviations from the nominal π^0 mass. For each cluster being considered as a photon candidate, we additionally require that the lateral profile of energy deposition in the calorimeter be consistent, at the 99% confidence level, with expectations for photons (that is, we use a 1% cut on the E9/E25). To suppress combinatoric backgrounds, we further required that the momentum of the $D_s^+\pi^0$ candidate be greater than 3.5 GeV/c.

To further reject background, we take advantage of the polarization of ϕ as it is spin-1 while the D_s and π^0 are spin-0. From signal MC events of $D_{sJ}^*(2317)^+ \to D_s^+\pi^0$, $D_s^+ \to \phi\pi^+$, $\phi \to K^+K^-$, we observed that the helicity angle of the $\phi \to K^+K^-$ varies as $cos^2\theta_h$, where θ_h is the opening angle between D_s^+ and one of the changed kaons in ϕ rest frame. Figure 3.1 shows the distribution of the helicity angle in signal MC as well as that in data where the combinatoric backgrounds tend to be flat. Therefore, we performed a cut optimization based on $\frac{S^2}{S+B}$, where S is taken to be the number of events in the D_s mass peak in data without the helicity angle cut multiplied by the fraction of signal events that remain after a particular $cos\theta_h$ cut; and B is number of events in D_s mass sideband region multiplied by the fraction of these events remaining

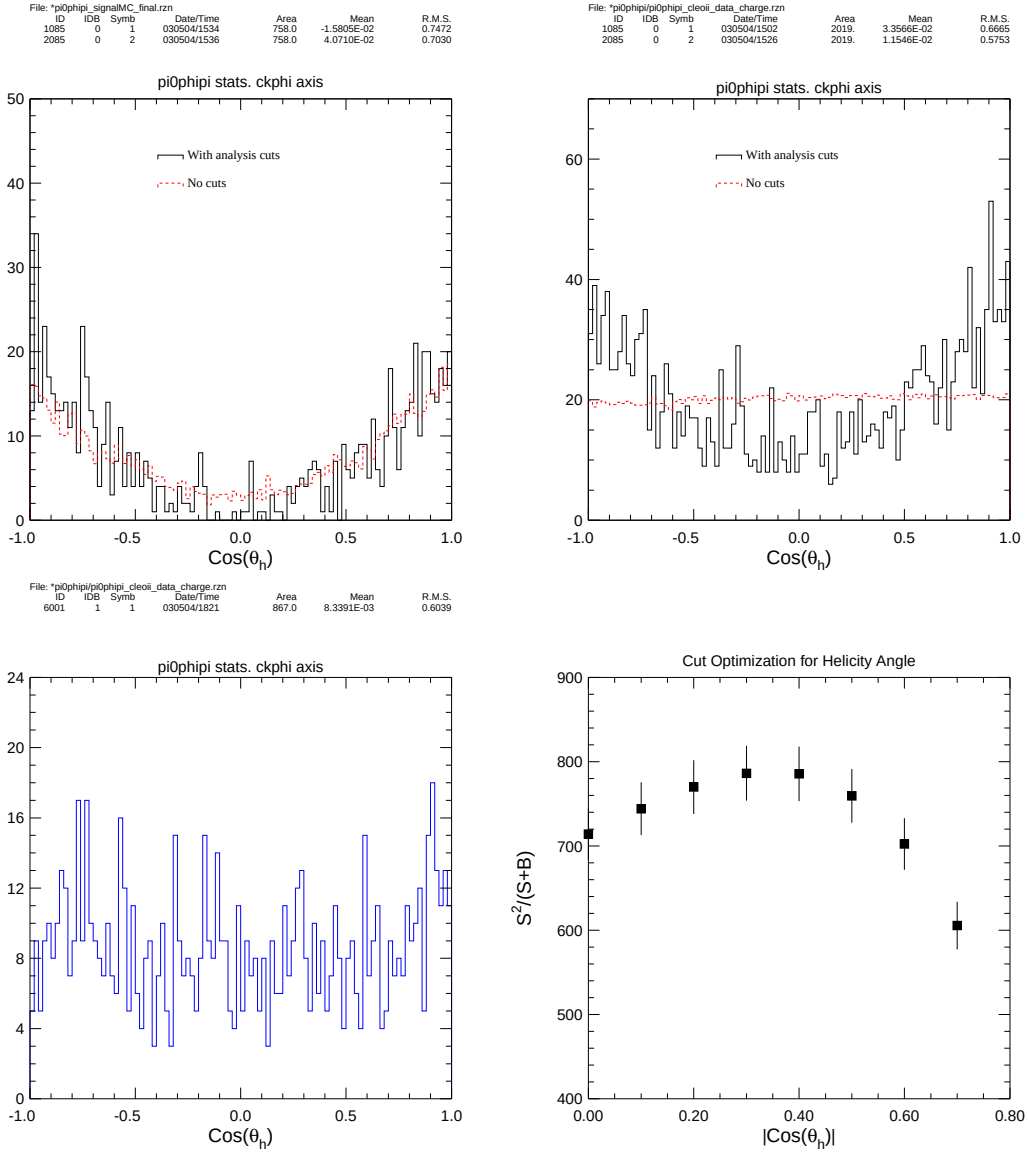

Figure 3.1: The distribution of the helicity angle of the $\phi \to KK$ decay in signal MC (top left) and CLEOII data (top right). The plot at the bottom left is for D_s mass sideband events in CLEOII data with selection criteria applied. The bottom right shows cut optimized at $|Cos(\theta_h)| > 0.3$.

after the $cos\theta_h$ cut. We found that a cut on $|cos\theta_h| > 0.3$ is optimal.

We plot the mass $M_{\phi\pi^+}$ satisfying the above requirements and fit the peak at around 1.97 GeV/c^2 to a Gaussian in Figure 3.2. The observed D_s^+ mass peak has a standard deviation (σ) of 6.5 ± 0.4 MeV/c^2 in our data. The other mass peak at around 1.87 GeV/c^2 corresponds to the Cabibbo-suppressed decay $D^+ \to \phi\pi^+$. This distribution is shown again in Figure 3.3(a), where the shaded regions indicate our selection criterion for D_s candidates, and for sideband regions used to study combinatoric backgrounds. The D_s signal region corresponds to $1.9565 < M(\phi\pi^+) < 1.9805$ GeV/c^2, which is $\pm 2.5\sigma$ about the known D_s mass.

3.2.2 The $D_{sJ}^*(2317)$ Signal

For $D_s\pi^0$ combinations satisfying the requirements in Section 3.2.1, a peak for the invariant mass of the $D_s\pi^0$ at around 2.3 GeV/c^2 is clearly evident in Figure 3.3(b). We note that there are no peaks in this region when $KK\pi$ combinations with $M(KK\pi)$ lying in D_s side band regions are combined with a π^0 candidate. To improve the experimental resolution on $M(D_s\pi^0)$, the known value of the D_s mass, $M_{D_s} = 1968.5 \pm 0.6$ MeV/c^2 [32], has been used to determine the energy of the $KK\pi$ system from its measured momentum. The narrow peak in Figure 3.3(b) (solid histogram) at a mass near 2.32 GeV/c^2 is in qualitative agreement with the BaBar observation. The other feature of note in the spectra is the sharp signal from $D_s^{*+} \to D_s^+\pi^0$ [33] near the kinematic threshold.

CLEO has a set of generic continuum MC samples with simulated data for the continuum production of $e^+e^- \to q\bar{q}$ where q stands for a u, d, s, or c quark. We

MINUIT Likelihood Fit to Plot 5010&0
pi0phipi stats. Mds axis
File: Generated internally 9-JUN-2003 11:07
Plot Area Total/Fit 12725. / 12725. Fit Status 3
Func Area Total/Fit 12725. / 12725. E.D.M. 1.176E-05
Likelihood = 75.4
χ^2= 76.3 for 50 - 9 d.o.f., C.L.=0.678E-01%

Errors		Parabolic	Minos	
Function 1: Gaussian (sigma)				
AREA	1262.6	± 61.85	- 61.07	+ 62.66
MEAN	1.9693	± 3.1462E-04	- 3.1359E-04	+ 3.1617E-04
SIGMA	6.54214E-03	± 3.8940E-04	- 3.7754E-04	+ 4.0163E-04
Function 2: Gaussian (sigma)				
AREA	631.15	± 50.97	- 50.15	+ 51.83
MEAN	1.8703	± 5.0106E-04	- 5.0050E-04	+ 5.0304E-04
SIGMA	5.84294E-03	± 4.8602E-04	- 4.6633E-04	+ 5.0835E-04
Function 3: Chebyshev Polynomial of Order 2				
NORM	43926.	± 521.4	- 519.8	+ 523.0
CHEB01	-0.28450	± 1.7607E-02	- 1.7566E-02	+ 1.7649E-02
CHEB02	4.10224E-02	± 1.7350E-02	- 1.7384E-02	+ 1.7317E-02

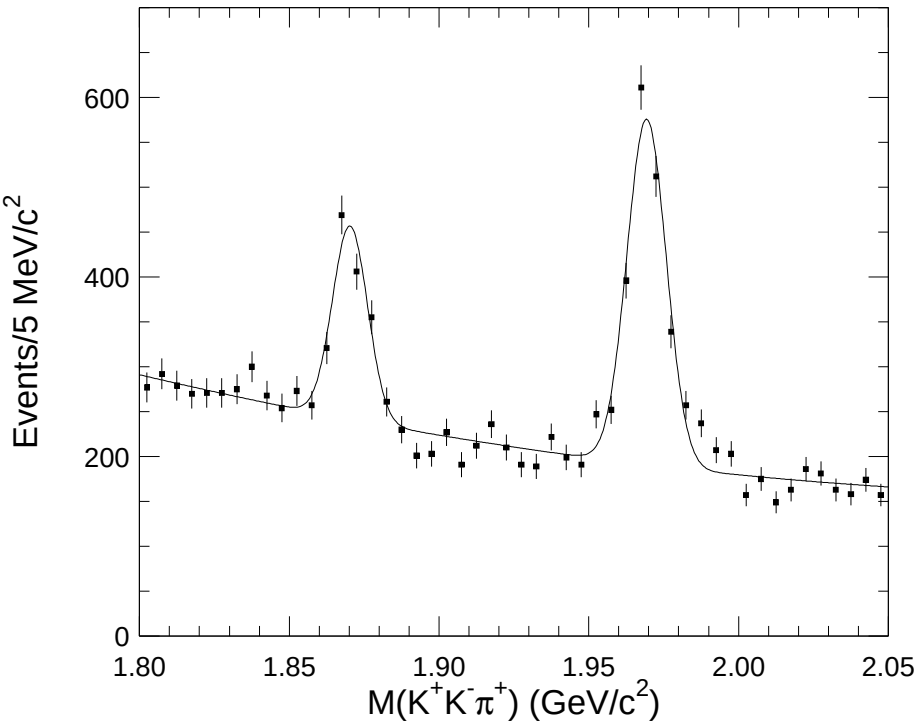

Figure 3.2: Fitting the mass distributions for $M(\phi\pi)$ after all analysis selection criteria except the D_s mass requirement applied to the CLEOII+II.V data.

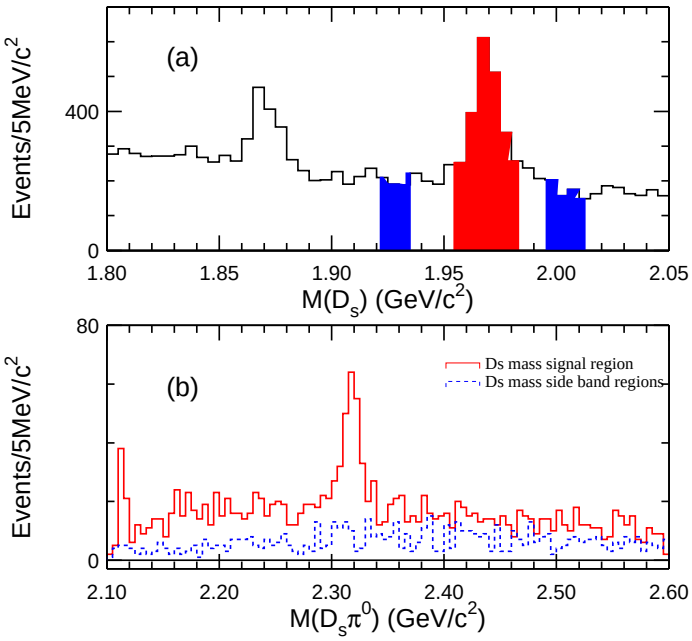

Figure 3.3: The distribution of $M(D_s)$ and $M(D_s\pi^0)$ in CLEOII+II.V data. The shaded regions at the top indicated the signal region and side bands of the D_s mass which are used to plot the $M(D_s\pi^0)$ histograms at the bottom. For $M(D_s\pi^0)$, the nominal D_s^+ mass is used in calculating the D_s energy.

run on a subset of this generic continuum MC samples (equivalent luminosity of 6 fb^{-1} for CLEOII and 11 fb^{-1} for CLEOII.V) where we reconstruct $D_s\pi^0$ as if it is from data. We plot the mass $M(D_s\pi^0) = M(KK\pi\pi^0)$ and the mass difference $\Delta M(D_s\pi^0) = M(D_s\pi^0) - M(D_s)$ in Figure3.4(a) and (b), respectively. Note again that the known value of the D_s mass, $M_{D_s} = 1968.5 \pm 0.6$ MeV/c^2 [32], has been used to determine the energy of the $KK\pi$ system from its measured momentum in Figure 3.4(a). This substitution is not done for $\Delta M(D_s\pi^0)$ in Figure 3.4(b), or for the calculation of other mass differences entering this analysis, since reconstruction errors and resolution effects associated with the D_s system tend to cancel in the mass difference. The overlaid curve represents the results from a fit of the data to a Gaussian signal function plus a second-order polynomial background function.

There is no peak seen in the 2.32 GeV/c^2 region for the continuum MC sample. To further show that our MC has been correctly calibrated to data, we perform fits to the mass difference ΔM for the decay mode $Ds^* \to D_s\pi^0$. The fit results in Figure 3.5 show that the mass difference $M(D_s\pi^0) - M(D_s) = 143.77 \pm 0.17 MeV/c^2$ for continuum MC and 143.76 ± 0.25 MeV/c^2 for data which also agrees with the old CLEO measurement in 1995: 143.76 ± 0.39 MeV/c^2 [33]. The agreement between the Monte Carlo and data distributions in Figure 3.4 in normalization as well as shape demonstrates that the simulation of 'random' photons accompanying D_s decays is accurate. The accuracy of this simulation is important for our detailed analysis of this signal, described in Section 3.4.

We have carried out a study on the shower shape to confirm that the random photon background can be dramatically reduced after applying a cut on the shower

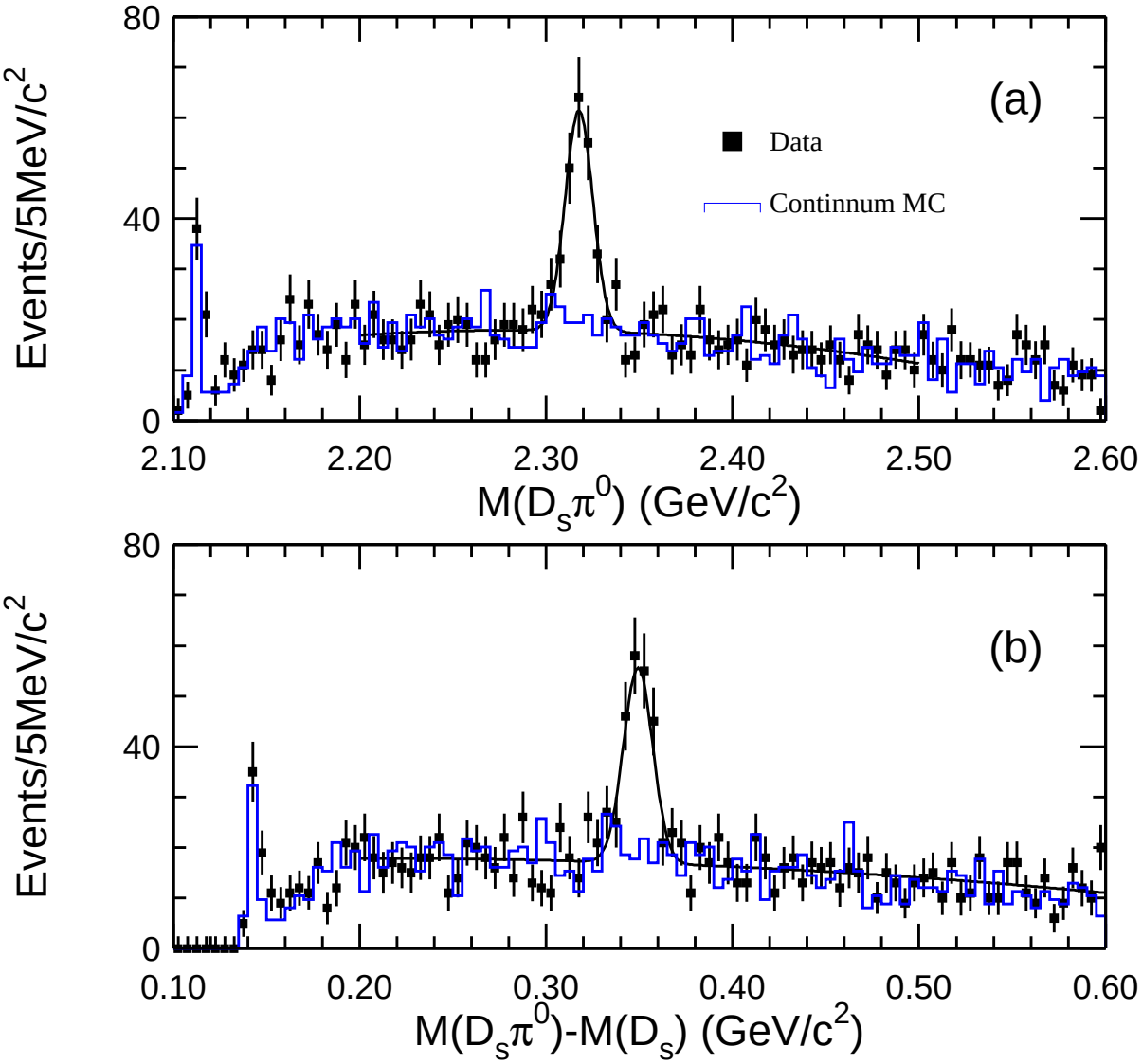

Figure 3.4: The distribution of $M(D_s\pi^0)$ and $\Delta M(D_s\pi^0)$ in CLEOII+II.V data and overlaid with generic continuum MC normalized to data according to equilvalent luminosity. The normalization on the left plots assumes a cross section of 3.25 nb for the $e^+e^- \to q\overline{q}$ ($q = u,\ d,\ s,\ c$).

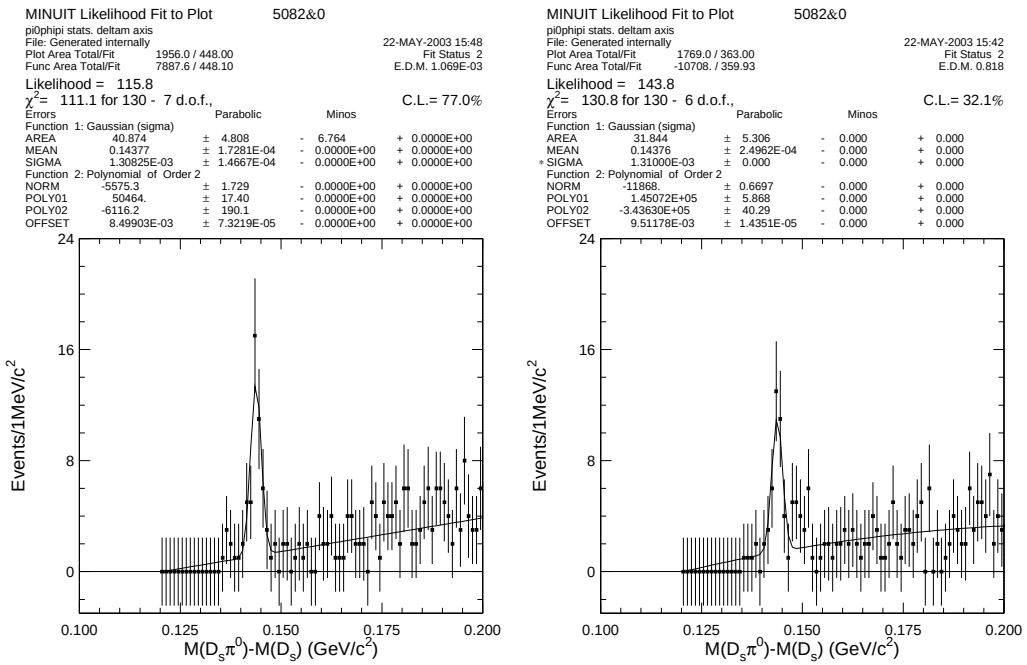

Figure 3.5: $D_s^*(2112)^{\pm} \to D_s^{\pm}\pi^0$, $D_s^{\pm} \to \phi\pi^{\pm}$, $\phi \to K^+K^-$ in continuum MC (left) and CLEOII+II.V data (right). Note that when fitting data, we fix the sigma of the Gaussian to that of the continuum MC.

shape. The effect of the 1% cut on E9/E25 cut for the showers can be shown in Figure 3.6. As a result of this study, we apply this E9/E25 cut for all decay modes in this

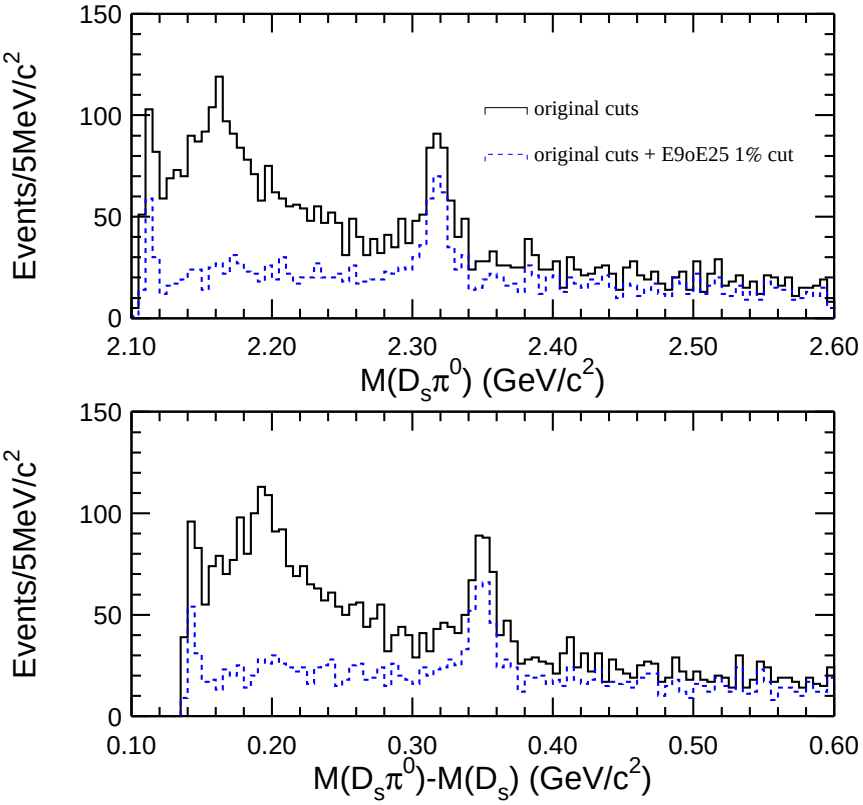

Figure 3.6: The $D_s\pi^0$ mass and mass difference spectrum showing the effect of the E9/E25 1% cut.

chapter.

Figure 3.7 explores different cuts on the photon energy. As the photon energy cuts increase, the $D^*_{sJ}(2317)$ signal persists while background is being suppressed.

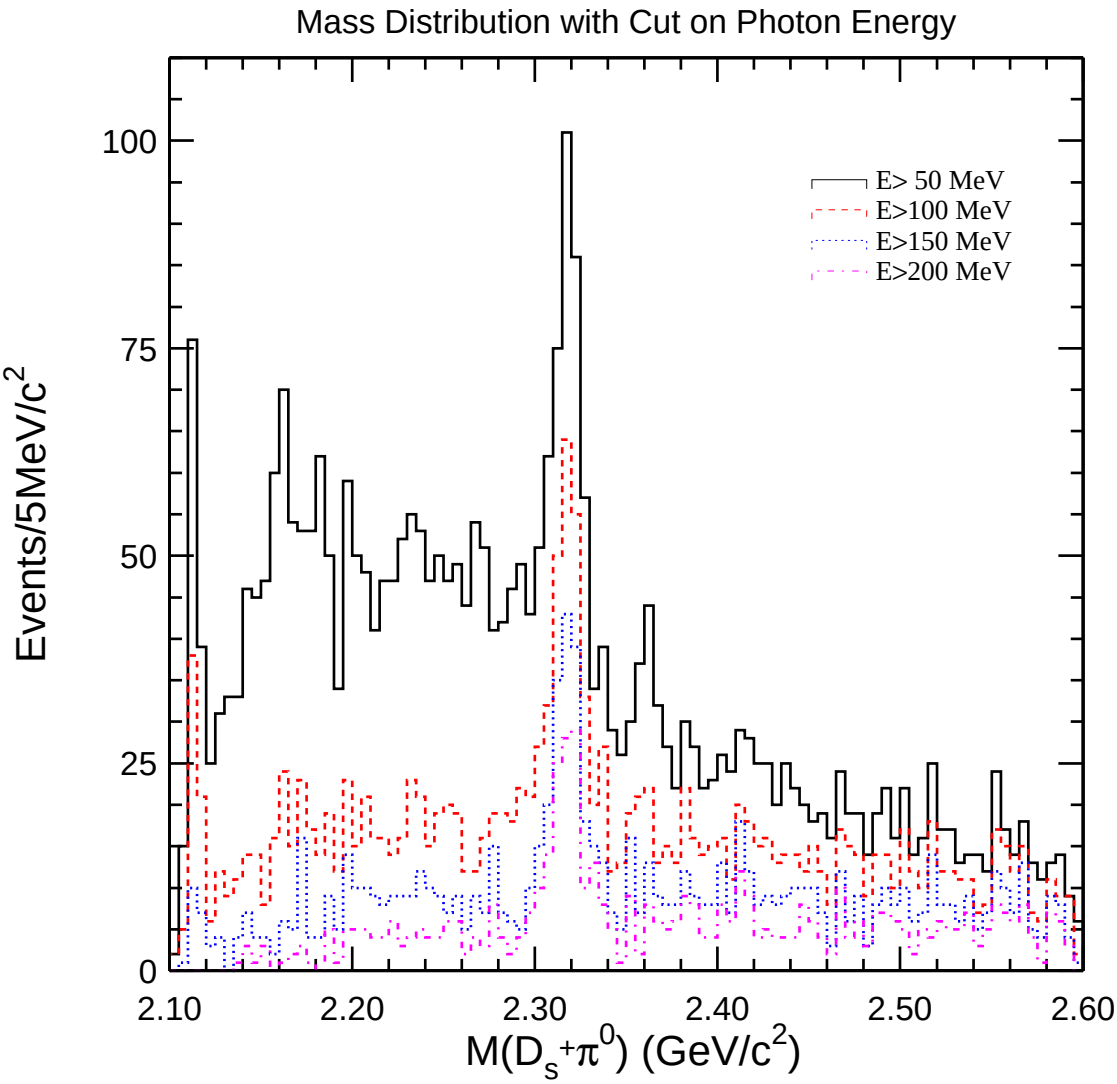

Figure 3.7: The distribution of $M(D_s\pi^0)$ in CLEOII+II.V data with different photon energy cuts applied to both photons of the π^0 daughter.

It is possible that we mis-identify a pion as a kaon, and by doing so we generate a peak at 2.32 GeV/c^2 as a reflection from other known particles. We study this effect by assigning our kaon candidate the pion mass or vice versa, and see what the mass spectra look like. We first look at the SGKADI in Figure 3.8 to see that the

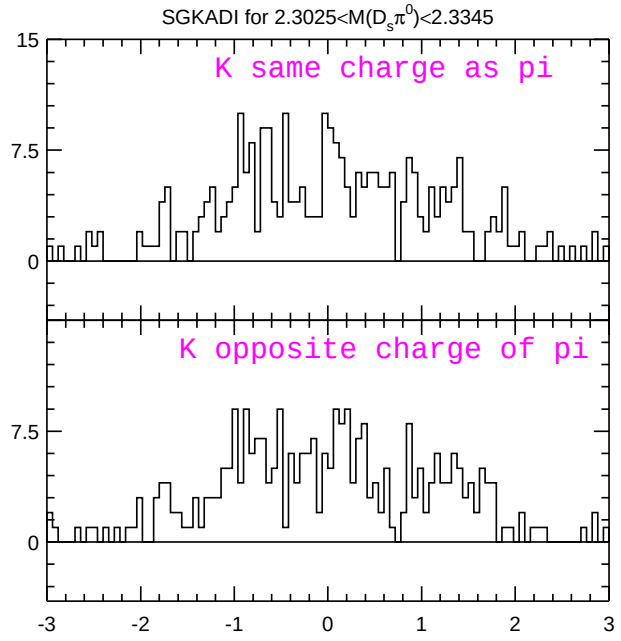

Figure 3.8: The distribution of SGKADI for kaons.

kaon candiates are kaons in the mass region of 2.3025< $M(D_s\pi^0)$ <2.3345 GeV/c^2, and then make a cut at |SGKADI| $\leq$2.5. As a reminder, the quantity SGKADI is the number of standard deviations away the dE/dx measurement for a track is from the expected value for a kaon. Figure 3.9 shows the invariant mass distribution for which we replace the mass of none (top left set), one (top right) or both (bottom

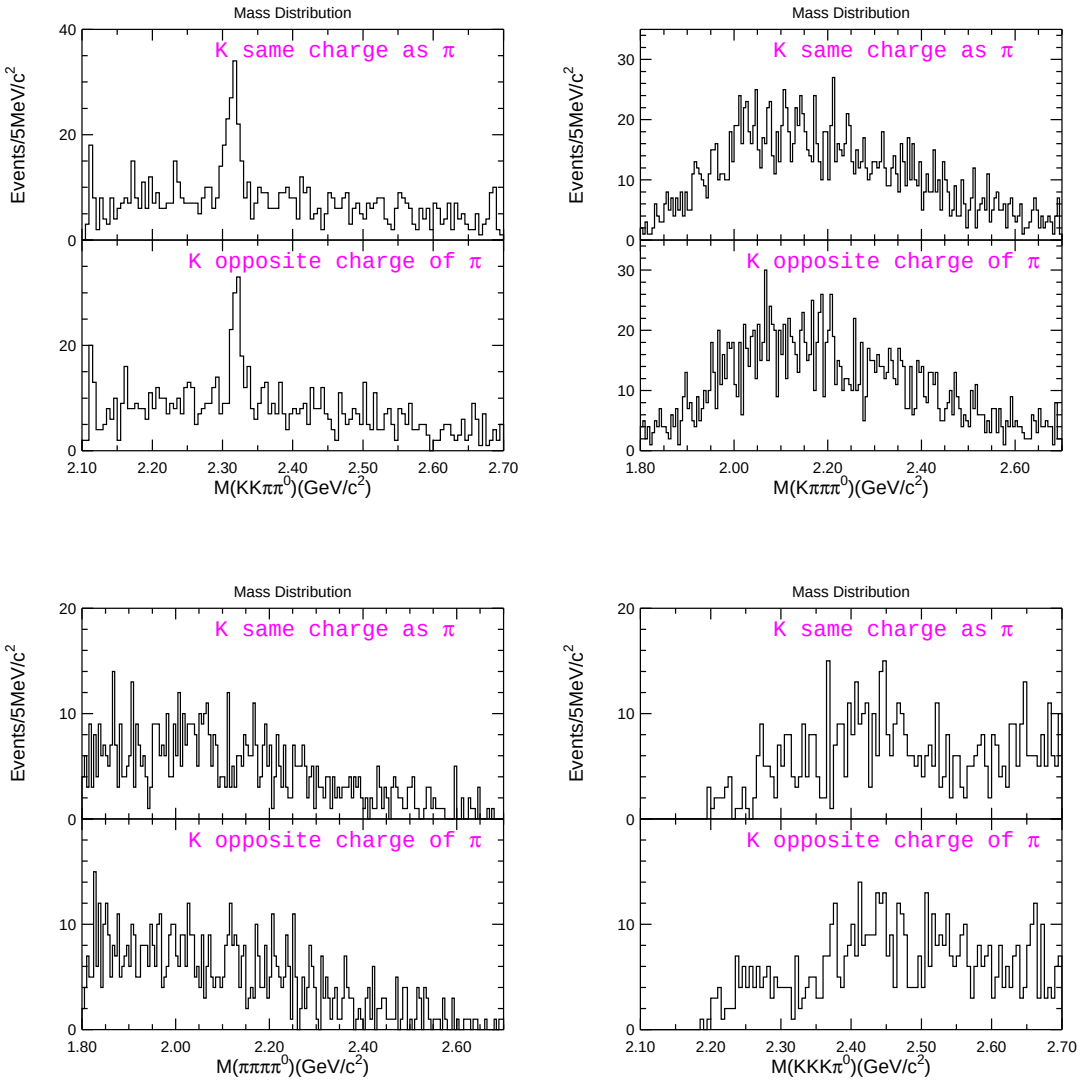

Figure 3.9: The mass distribution in CLEOII+II.V data. In each case, we replace the mass of none (top left set), one (top right) or both (bottom left) of the kaon candidates with the π mass. The bottom right plot replaces the mass of the pion candidate with the kaon mass.

left) of the kaon candidates with the π mass. There were no narrow enhancements in the $M(D_s\pi^0)$ spectrum near 2.32 GeV/c^2 observed, except at the first case without any mass substitution for the kaon. Therefore, we can conclude that the peak at 2.32 GeV/c^2 can not be generated by mis-assignment of particle masses and not a reflection of other processes.

From a fit to the mass difference $\Delta M(D_s\pi^0)$ in Figure 3.10 to a Gaussian signal

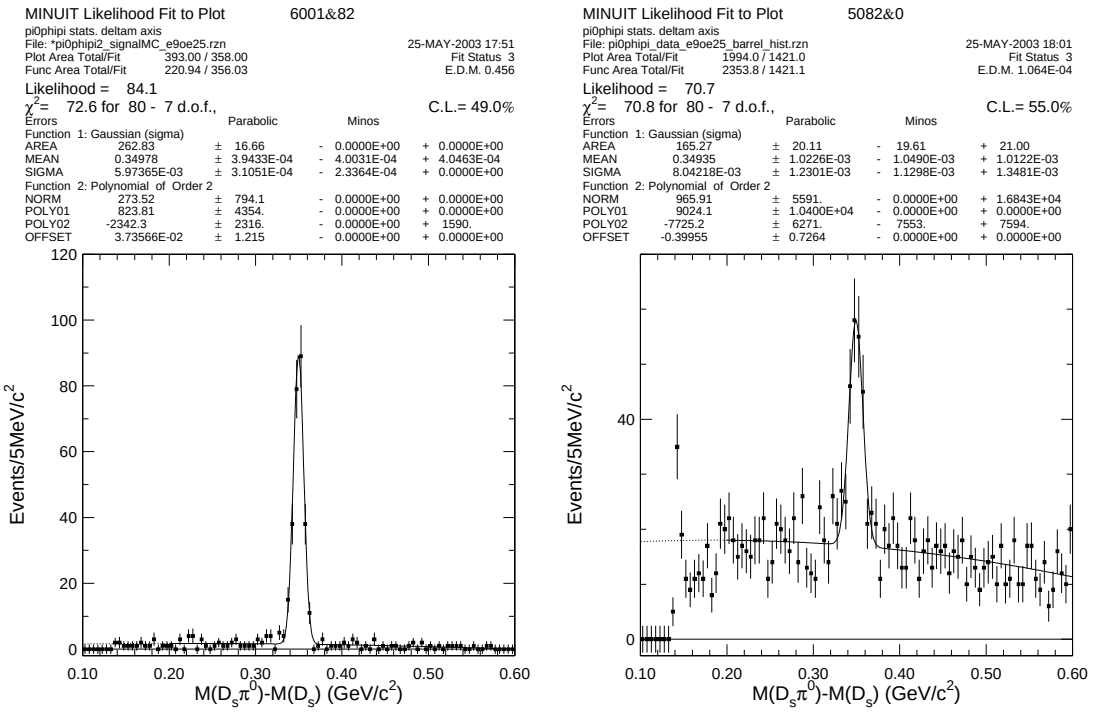

Figure 3.10: The fit to the mass difference distributions in $D^*_{sJ}(2317) \to D_s\pi^0$ signal MC (left) and data with single Gaussian (right).

shape and second-order polynomial background function, we obtain a yield of 165 ± 20 events in the peak near 350 MeV/c^2 allowing the mean and Gaussian width of the peak to float. The mean and Gaussian width from the fit are $\langle \Delta M(D_s\pi^0) \rangle = 349.4 \pm$

1.0 MeV/c^2 and $\sigma = 8.0^{+1.3}_{-1.1}$ MeV/c^2, where the errors are due to statistics only. The peak is somewhat broader than the expected mass resolution of 6.0 ± 0.3 MeV/c^2, determined from Monte Carlo simulations. The detection efficiency associated with the reconstruction of the full $D^*_{sJ}(2317)^+ \to D^+_s\pi^0$, $D^+_s \to \phi\pi^+$, $\phi \to K^+K^-$ decay chain is (9.73 ± 0.57) % for the portion of the $D^*_{sJ}(2317)^+$ momentum spectrum above 3.5 GeV/c, where this efficiency does not include the D_s and ϕ decay branching fractions.

We have performed a number of fits with different D_s mass windows and different shapes for the background. Table 3.1 summarizes the yields. We have chosen to

Table 3.1: Summary of the $D_s\pi^0$ yield as function of fit and selection variations.

D_s Mass Window	Background Polynomial	Yield	ΔM	Gaussian Width
$1.955 - 1.979$	3rd Order	146 ± 19	349.4 ± 1.0	7.5 ± 1.2
$1.955 - 1.979$	2nd Order	152 ± 19	349.3 ± 1.0	7.8 ± 1.2
$1.9565 - 1.9805$	3rd Order	157 ± 20	349.5 ± 1.0	7.6 ± 1.2
$1.9565 - 1.9805$	2nd Order	165 ± 20	349.4 ± 1.0	8.0 ± 1.2
Choice		165 ± 26	349.4 ± 1.0	8.0 ± 1.3

use the mass window and background description that matches the one used in the analysis of the background (Section 3.4). Systematic uncertainties are estimated to be ± 16 on the yield and ± 0.6 on the width added in quadrature with the statistical uncertainty to take into account variations among the results.

A peak in the $D_s\pi^0$ mass spectrum confirms the existence of the $D^*_{sJ}(2317)^+$ resonance, and we further showed that it cannot be explained as reflections from

decays of known particles. Our measurements of the mean mass difference and width of the peak are consistent with the values obtained by BaBar [13] for the $D^*_{sJ}(2317)^+$ resonance. We discuss the width, as well as systematic errors in the measurements of the mass and width of the $D^*_{sJ}(2317)$ later in this chapter.

3.3 Searches for $D^*_{sJ}(2317)$ in Other Decay Modes

Having confirmed the new narrow resonance, we explore the decay dynamics of the $D^*_{sJ}(2317)$ by searching for other strong decay and electromagnetic decay modes. We have searched in the decay modes $D_s\gamma$, $D^*_s\gamma$, $D_s\pi^+\pi^-$, and $D^*_s\pi^0$ as described in the following subsections.

3.3.1 Decays to $D_s\gamma$

If the $D^*_{sJ}(2317)$ is indeed a 0^+ $L = 1$ $c\overline{s}$ meson, as has been suggested [17], the $D^*_{sJ}(2317) \to D_s\gamma$ is forbidden by parity and angular momentum conservation. We verify this property by performing the search of the $D^*_{sJ}(2317)$ in the $D^+_s\gamma$ final state.

To search for states decaying to $D^+_s\gamma$, we have formed $D^+_s\gamma$ combinations by selecting photons of energy greater than 150 MeV for events containing $D^+_s \to \phi\pi^+$ candidates as in the $D_s\pi^0$ analysis. We require that the photon candidates are in the angular region $|cos\theta| < 0.71$, and they are not not matched to any tracks and are not split-offs from hadronic interaction in the calorimeter. We also veto photons that can be paired with another photon such that the invariant mass $M(\gamma\gamma)$ is within two standard deviation of the π^0 mass. This is called "π^0 veto". We require that

the γ and ϕ are in the same hemisphere to reduce background based on a study done with MC. To suppress combinatoric backgrounds, we further require that the momentum of the $D_s\gamma$ candidate be greater than 3.5 GeV/c. The mass difference $\Delta M(D_s\gamma) = M(D_s\gamma) - M(D_s)$ spectrum for this sample is plotted on a logarithmic scale in Figure 3.11, illustrating that a large D_s^* sample can be obtained. From a sample of 600,786 $D_s^* \to D_s^+\gamma$, $D_s^+ \to \phi\pi^+$ MC events, the reconstruction efficiency is $(18.46 \pm 0.09)\%$ for the portion of the $D_s\gamma$ momentum above 3.5 GeV/c.

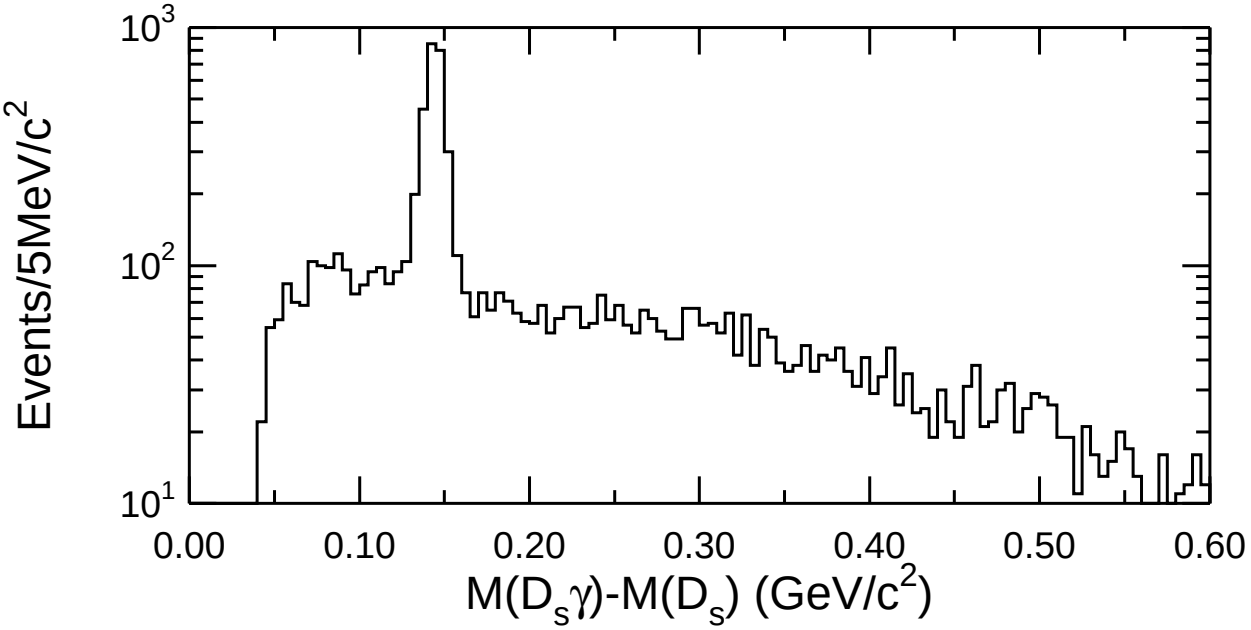

Figure 3.11: The mass difference $M(D_s\gamma) - M(D_s)$ in data. Note that the plot is on a logarithmic scale. The peak is due to the transition $D_s^{*+} \to D_s^+\gamma$.

Figure 3.11 also shows the region of the $\Delta M(D_s\gamma)$ spectrum where the $D_{sJ}^*(2317) \to D_s\gamma$ decay would appear. There is no evidence for a signal near 350 MeV/c^2 corresponding to a $M(D_s\gamma)$ in the vicinity of 2.32 GeV/c^2. Thus, we obtained an upper

limit for the decay $D_{sJ}^*(2317)^+ \to D_s^+\gamma$ by performing unconstrained fits to the ΔM spectra with widths fixed to MC values and the mean fixed to the extracted from the decay $D_s^+\pi^0$. The yield obtained from the fit is -18.9 ± 12.6 as shown in Figure 3.12. The central value for the area is used as the yield and the statistical error from the fit

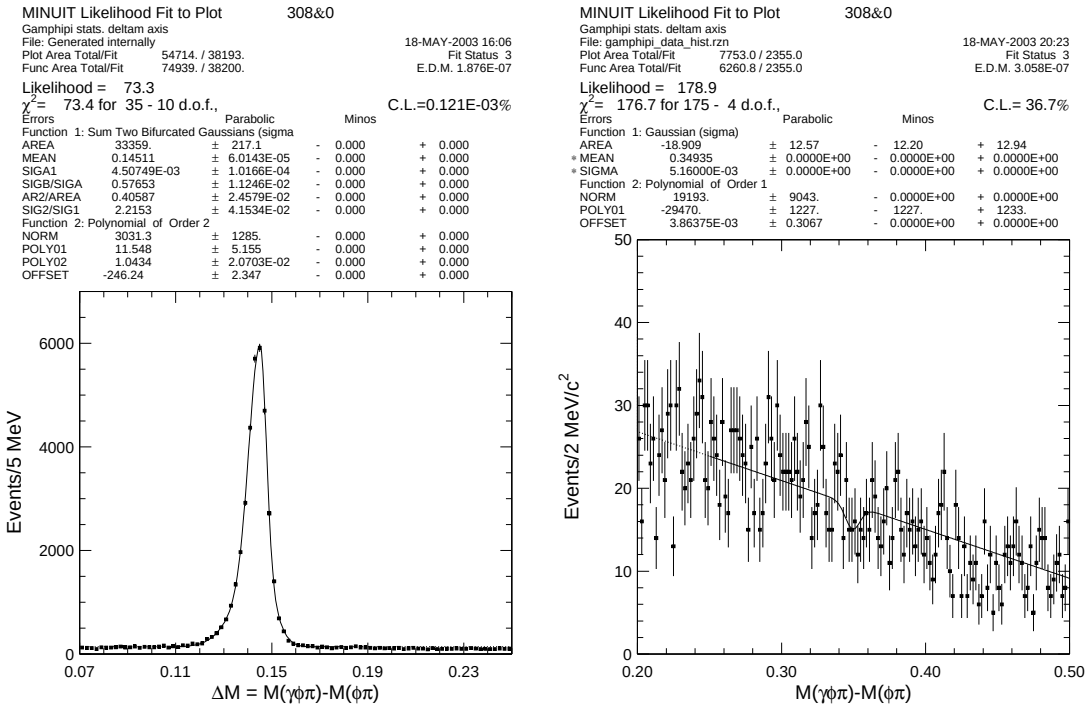

Figure 3.12: The fit to mass difference $M(\gamma\phi\pi) - M(\phi\pi)$ for $D_s^{*+} \to D_s^+\gamma$ signal MC (left) and $D_{sJ}^*(2317)^+ \to D_s^+\gamma$ in data (right).

added in quadrature with the difference when varying the width by one σ is the error on the yield. The uncertainty is dominated by the statistical error on the fitted yield and the limit on the relative rates are calculated assuming a Gaussian distribution with negative values not allowed[1]. We report the upper limit for $D_{sJ}^*(2317)^+ \to D_s^+\gamma$

[1]All the upper limits presented in this note use this method.

relative to $D_{sJ}^*(2317)^+ \to D_s^+\pi^0$ in Table 3.2.

3.3.2 Decays to $D_s^*\gamma$

The $D_{sJ}^*(2317)$ could decay via S-wave to $D_s^*\gamma$ and conserve parity and angular momentum. The isospin-violating decay $D_{sJ}^*(2317) \to D_s\pi^0$ is not as severely phase-space suppressed as in the case of the corresponding decay of the D_s^* where the electromagnetic decay dominates. Therefore, $D_{sJ}^*(2317) \to D_s\pi^0$ could compete with the electromagnetic decay or even dominate.

We search for the decay of $D_{sJ}^*(2317)^+ \to D_s^{*+}\gamma$ with $D_s^{*+} \to D_s^+\gamma$. The event selection for $D_s^+ \to \phi\pi^+$ is also the same as these in the $D_s\pi^0$ analysis, except a cut on $P(D_s^*\gamma) > 3.5$ GeV/c. We combine a D_s candidate with a photon candidate to form D_s^{*+}. The requirements on the photon candiates are the same as those in Section 3.3.1 except an additional cut $E_\gamma > 50$ MeV on the photon candidate decayed from the D_s^*. Note that the photon from the $D_{sJ}^*(2317)$ decay is consistently required to have energy greater than 150 MeV. Finally, we select $D_s\gamma$ combinations where the mass difference $\Delta M(D_s\gamma)$ is consistent with D_s^{*+} within 13 MeV/c^2 (2.5σ), or between 0.1308 and 0.1568 GeV/c^2.

The broad peak in the $\Delta M(D_s^*\gamma)$ spectrum in Figure 3.13 near 150 MeV/c^2 is due to a random photon being combined with the D_s^+ candidate to form the D_s^* candidate in the real $D_s^{*+} \to D_s^+\gamma$ decays, and the actual photon from this transition being combined with the D_s^* candidate to form the D_{sJ}^* candidate. There is no significant peak in this spectrum near 205 MeV/c^2, where a signal from $D_{sJ}^*(2317)$ decay would be expected.

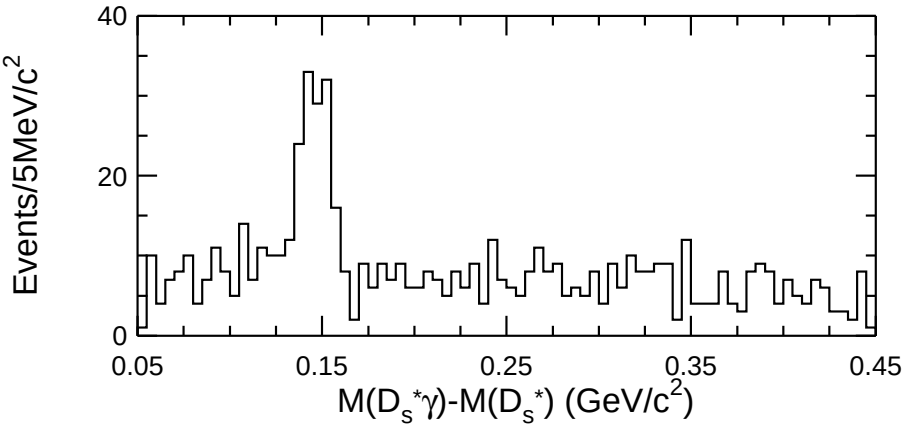

Figure 3.13: The spectrum of the mass difference $\Delta M(D_s^*\gamma) = M(D_s^*\gamma) - M(D_s^*)$ for $D_s^*\gamma$ candidates.

To obtain an upper limit for the decay $D_{sJ}^*(2317)^+ \to D_s^{*+}\gamma$, we first determine the reconstruction efficiency using a sample of 9957 signal MC events of $D_{sJ}^*(2317) \to D_s^*\gamma$, $D_s^* \to D_s\gamma$, $D_s \to \phi\pi$, $\phi \to K^+K^-$. From the fit in Figure 3.14, we obtained an efficiency of $(2.00 \pm 0.14)\%$ over the entire momentum spectrum, and $(7.01 \pm 0.48)\%$ for the portion of the $D_s^*\gamma$ momentum above 3.5 GeV/c.

Using the same method as the one described in Section 3.3.1, we reported the upper limit for $D_{sJ}^*(2317)^+ \to D_s^{*+}\gamma$ relative to $D_{sJ}^*(2317)^+ \to D_s^+\pi^0$ in Table 3.2.

3.3.3 Decays to $D_s\pi^+\pi^-$

The $D_s\pi^+\pi^-$ final state is kinematically allowed. The decay $D_{sJ}^*(2317) \to D_s\pi^+\pi^-$ conserves isospins, but is suppressed by the OZI rule. Parity and angular momentum conservation forbid the decay of a 0^+ state to three particles with 0^- each. Therefore,

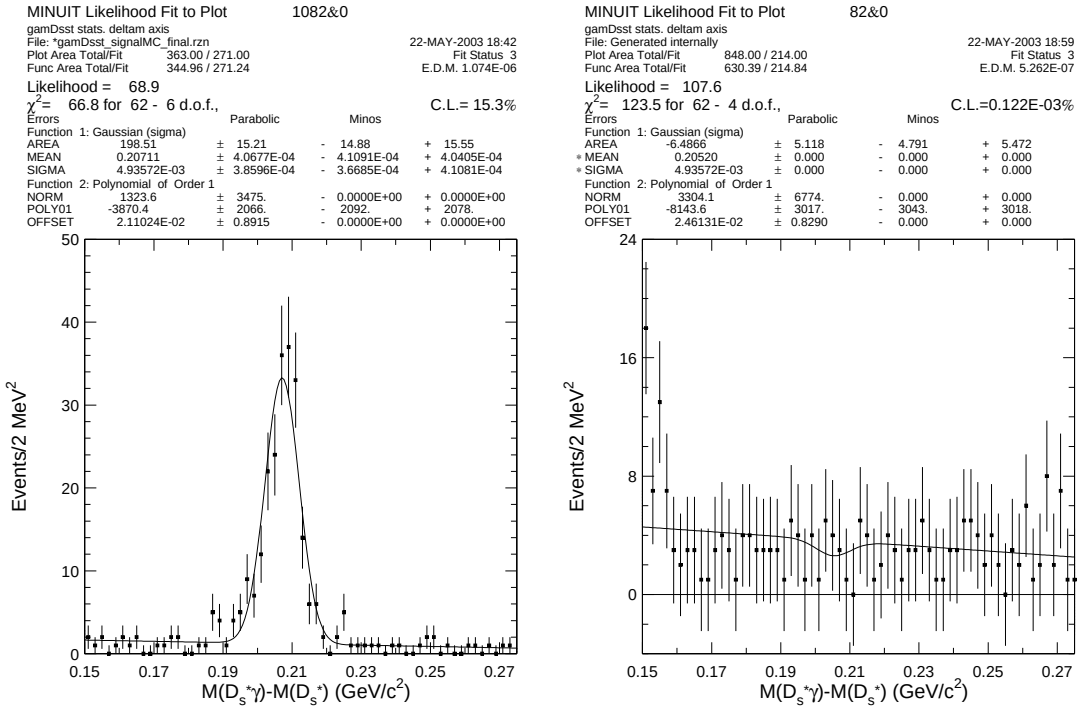

Figure 3.14: The mass difference $\Delta M(D_s^*\gamma)$ for $D_{sJ}^*(2317)^+ \to D_s^{*+}\gamma$, $D_s^{*+} \to D_s^+\gamma$, $D_s^+ \to \phi\pi^+$, $\phi \to K^+K^-$ signal MC (left) and CLEOII+II.V data (right).

observation of the $D^*_{sJ}(2317) \to D_s\pi^+\pi^-$ would provide strong evidence against the interpretation of the $D^*_{sJ}(2317)$ as a 0^+ meson.

For the $D_s\pi^+\pi^-$ final state, we combine the D_s candidates with two oppositely charged tracks identified as pions. The event selection criteria for $D_s^+ \to \phi\pi^+$, $\phi \to K^+K^-$ are the same as those in the $D_s\pi^0$ analysis described in Section 3.2.1. For combinations that satisfy these requirements, the mass difference $\Delta M(D_s\pi\pi) = M(D_s\pi\pi) - M(D_s)$ is plotted in Figure 3.15 where no significant peak is evident in the vicinity of 350 MeV/c^2.

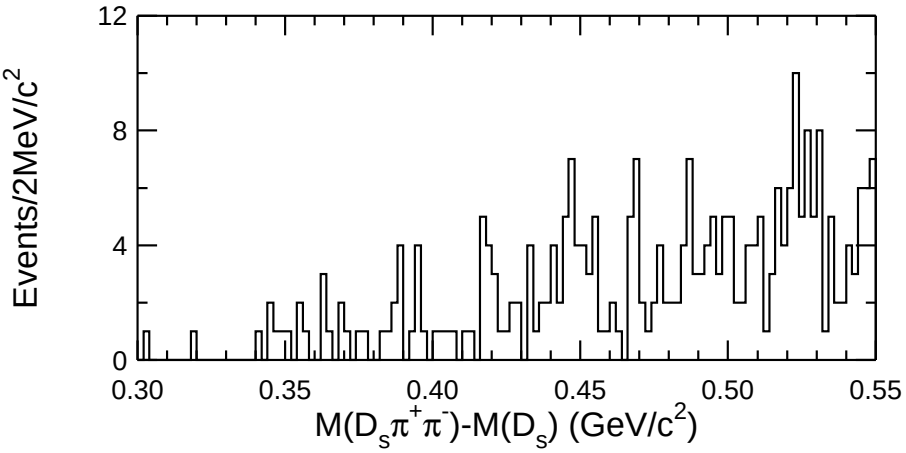

Figure 3.15: The mass difference $\Delta M(D_s\pi\pi) = M(D_s\pi\pi) - M(D_s)$ for $D_s^+\pi^+\pi^-$ candidates, as described in the text.

To determine the reconstruction efficiency and the expected resolution, we use 9963 signal MC events of $D^*_{sJ}(2317)^+ \to D_s^+\pi^+\pi^-$, $D_s^+ \to \phi\pi^+$, $\phi \to K^+K^-$. From a fit to $\Delta M(D_s\pi\pi)$ in Figure 3.16, we obtained an efficiency of $(5.67 \pm 0.23)\%$ over the entire momentum spectrum, and $(19.79 \pm 0.75)\%$ for the portion of the $D_s\pi^+\pi^-$

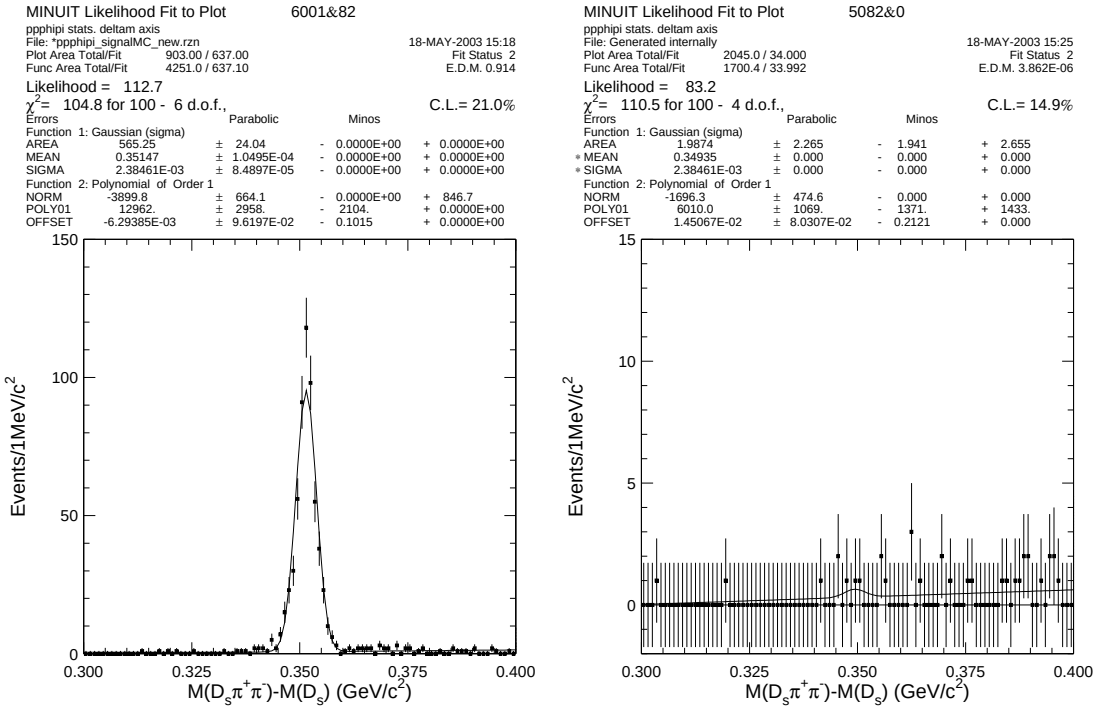

Figure 3.16: The mass difference $\Delta M(D_s\pi\pi)$ for $D^*_{sJ}(2317)^+ \to D_s^+\pi^+\pi^-$, $D_s^+ \to \phi\pi^+$, $\phi \to K^+K^-$ signal MC (left) and CLEOII+II.V data (right).

momentum above 3.5 GeV/c.

We use the same method as the one described in Section 3.3.1 to obtain an upper limit for $D_{sJ}^*(2317)^+ \to D_s^+\pi^+\pi^-$ relative to $D_{sJ}^*(2317)^+ \to D_s^+\pi^0$ listed in Table 3.2.

3.3.4 Decays to $D_s^*\pi^0$

The decay $D_{sJ}^*(2317)^+ \to D_s^+\pi^0$ is kinematically allowed although it is forbidden by parity and angular momentum conservation if $D_{sJ}^*(2317)$ is a 0^+ $L = 1$ $c\overline{s}$ meson.

The search of $D_{sJ}^*(2317)^+ \to D_s^+\pi^0$ was carried out with slightly different track quality requirements and π^0 reconstruction from those decay modes described above. The detailed selection criteria which are different from those in Section 3.2.1 are described in an internal note [34] for CLEO. As a cross-check, we have shown in Figure 3.17 that the mass spectra agree well for the different track selections. The differences are negligible. Thus, we can trust that studies done with the two sets of selection criteria yield consistent results.

The energy of photons selected for reconstruction of the $D_s^{*+} \to D_s^+\gamma$ decay is required to be greater than 50 MeV, same as the requirement for the D_s^* candidates involved in Section 3.3.2. We do not perform the π^0 veto on the photon candidates used in the D_s^{*+} reconstruction in order to maintain efficiency for this final state. The D_s^* candidates are then combined with a π^0 candidate reconstructed from two photons where the invariant mass of the di-photon is within $-3.0\sigma < M(\gamma\gamma) - M(\pi^0) < 2.5\sigma$. The $D_s^*\pi^0$ candidates are required to have momenta above 3.5 GeV/c to reject large amount of combinatorial background at lower momentum.

There is no peak at $\Delta M(D_s^*\pi^0) \sim 205$ MeV/c^2 in Figure 3.18 where we expect

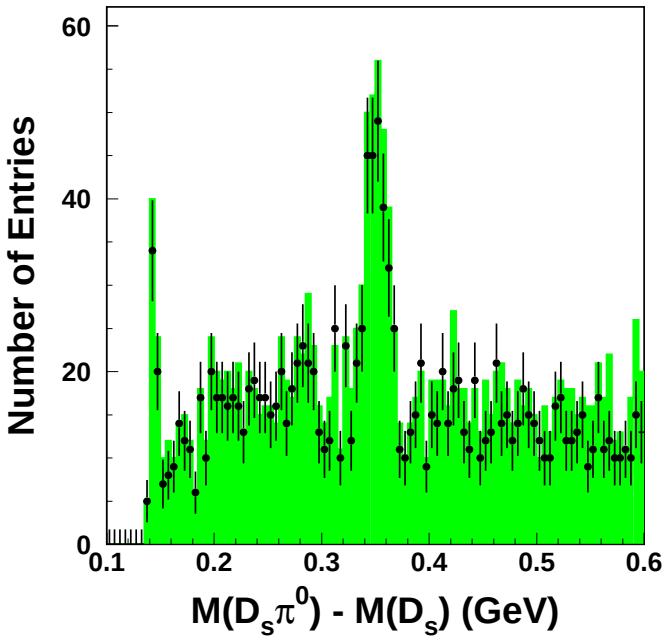

Figure 3.17: The $D_s\pi^0$ mass spectrum with slightly different track selections. The difference between the data points and the shaped histogram is due to different track selections

there would be if the $D_{sJ}^*(2317)^+$ decays to $D_s^{*+}\pi^0$. However, a significant narrow peak is evident near 350 MeV/c^2 in $\Delta M(D_s^*\pi^0)$ which suggests another new resonance with a mass near 2.46 GeV/c^2. Section 3.4 will discuss this new resonance in more detail.

3.3.5 Summary of Different Decay Modes for $D_{sJ}^*(2317)$

Table 3.2 summarizes the upper limits on the branching fractions of the decay modes searched but no signals observed in Section 3.3 relative to the observed $D_s^+\pi^0$ mode. The normalization for these limits is based on the determination that $(81.7 \pm 5.7)\%$ of the observed yield of $165 \pm 20[stat.] \pm 16[sys.]$ events in the peak of the $\Delta M(D_s\pi^0)$ spectrum in Figure 3.4 are attributable to $D_{sJ}^*(2317) \to D_s\pi^0$ decay after accounting for the background contributions as discussed in Section 3.4.1. The ± 16 events for systematic uncertainties are estimated by varying selection criteria and the parametrization of signal and background shape used in the fit to Figure 3.4.

3.4 Observation of a New State at 2.463 $\mathbf{GeV/c^2}$

In Section 3.3.4 where we search for the $D_s^{*+}\pi^0$ final state, we observe a peak at $\langle \Delta M(D_s^*\pi^0) \rangle = 349.8 \pm 1.3$ MeV/c^2 in Figure 3.18(a). A fit to the peak is performed by using a Gaussian signal function plus a second order polynomial background function. The fit yields a total of 55 ± 10 events and a Gaussian width of 6.1 ± 1.0 MeV/c^2 for the peak, consistent with the mass resolution of 6.6 ± 0.5 MeV/c^2 obtained from Monte Carlo simulations. The existence of this peak leads us to investigate the pos-

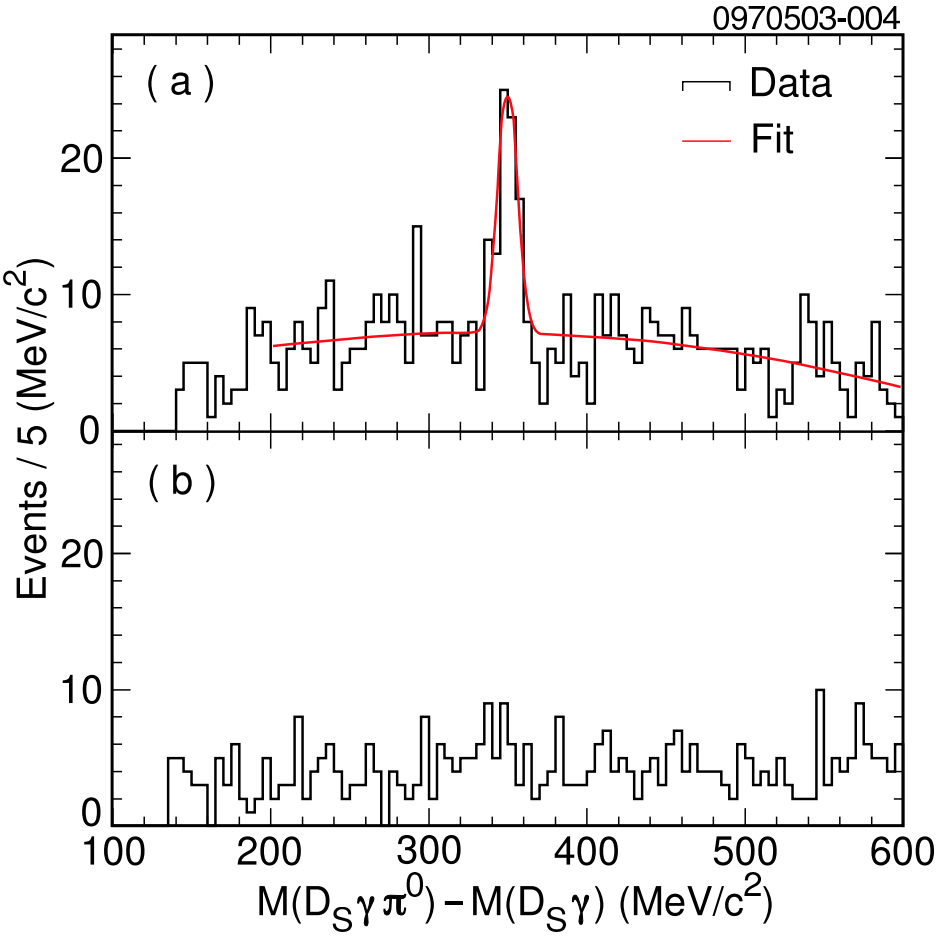

Figure 3.18: (a) The mass difference spectrum $\Delta M(D_s^*\pi^0) = M(D_s\gamma\pi^0) - M(D_s\gamma)$ for combinations where the $D_s\gamma$ system is consistent with D_s^* decay, as described in the text. (b) The corresponding spectrum where $D_s\gamma$ combinations are selected from the D_s^* side band regions.

Table 3.2: 90% CL upper limits on the ratio of branching fractions for $D^*_{sJ}(2317)$ to the decay modes shown relative to the $D_s^+\pi^0$ state. Also shown are the theoretical expectations [17], under the assumption that the $D^*_{sJ}(2317)$ is the lowest-lying 0^+ $c\overline{s}$ meson.

Final State	Yield	Efficiency	Limit (90% CL)	Prediction
$D_s^+\pi^0$	135 ± 23	$(9.7 \pm 0.6)\,\%$	—	
$D_s^+\gamma$	-19 ± 13	$(18.5 \pm 0.1)\,\%$	< 0.052	0
$D_s^{*+}\gamma$	-6.5 ± 5.2	$(7.0 \pm 0.5)\,\%$	< 0.059	0.08
$D_s^+\pi^+\pi^-$	2.0 ± 2.3	$(19.8 \pm 0.8)\,\%$	< 0.019	0
$D_s^{*+}\pi^0$	-1.7 ± 3.9	$(3.6 \pm 0.3)\,\%$	< 0.11	0

sibility of a second narrow resonance with a mass near 2.46 GeV/c^2 that decays to $D_s^{*+}\pi^0$. We denote the postulated particle as the $D_{sJ}(2460)^+$.

3.4.1 Analysis of Cross Feed between $D_s^+\pi^0$ and $D_s^{*+}\pi^0$ Samples

The kinematics of the $D_s^+\pi^0$ and $D_s^{*+}\pi^0$ decays are very similar, and it is possible that they can reflect into one another. For example, the $D_{sJ}(2460)$ will generate a peak in $\Delta M(D_s\pi^0)$ at the same region as the $D^*_{sJ}(2317)$ signal if the photon from the D_s^* decay is not observed. We refer to the background events from this scenario as a "feed down" contribution from the $D_{sJ}(2460)$ state. The probability of feeding down is $(84\pm4\pm10)\%$, where the first error is statistical and the second is due to systematic errors. This includes the probability of the $D_{sJ}(2460)$ feeding down to $D^*_{sJ}(2317)$ as well as the photon finding efficiency. The feed down from the $D_{sJ}(2460)$ results in

smearing of the width for real $D^*_{sJ}(2317)$ decays which is $\sigma = 14.9 \pm 0.4$ MeV/c^2 according to Monte Carlo simulations shown in Figure 3.19.

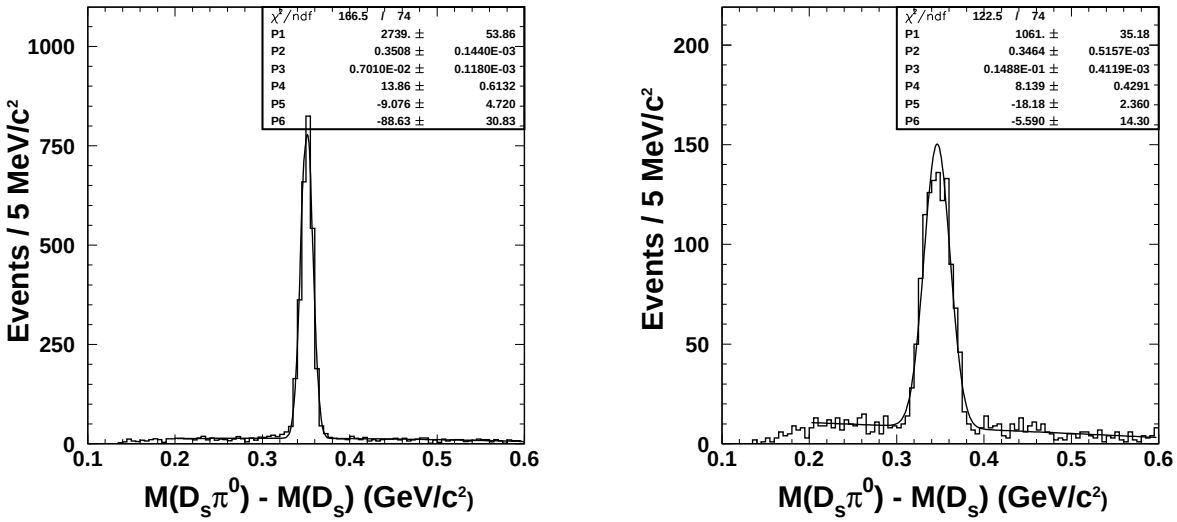

Figure 3.19: The mass difference spectra $\Delta M(D_s\pi^0)$ using $D^*_{sJ}(2320)^+ \rightarrow D^+_s\pi^0$ (left) and $D_{sJ}(2460)^+ \rightarrow D^{*+}_s\pi^0$ (right) signal MC. We have demonstrated that the width for $D^*_{sJ}(2317)^+ \rightarrow D^+_s\pi^0$ would be broader if there is feed down from $D_{sJ}(2460)$.

The $D^*_{sJ}(2317)$ will generate a peak in $\Delta M(D_s\pi^0)$ if a random photon combined with a D_s candidate makes a D^*_s and thus the $D^*_{sJ}(2317)$ is being reconstructed as $D_{sJ}(2460)$. We refer the $D^*_{sJ}(2317)^+ \rightarrow D^+_s\pi^0$ decay as a feed up to the $D_{sJ}(2460)^+ \rightarrow D^{*+}_s\pi^0$ signal region. This happens for $(9.1 \pm 0.7 \pm 1.5)\%$ of the reconstructed decays and also results in smearing of the width according to a Monte Carlo simulation of $D^*_{sJ}(2317)^+ \rightarrow D^+_s\pi^0$ production. The first error in the probablity is due to limited Monte Carlo statistics while the second is due to systematic

uncertainties associated with the modeling of extra photons in the simulations, and the fraction of such combinations that are counted by the fit to the $\Delta M(D_s^*\pi^0)$ distribution as contributing to the Gaussian signal. Figure 3.20 shows that the width of the mass difference $\Delta M(D_s^*\pi^0)$ would be broader if $D_{sJ}^*(2317)^+ \to D_s^+\pi^0$ events are reconstructed as $D_s^{*+}\pi^0$.

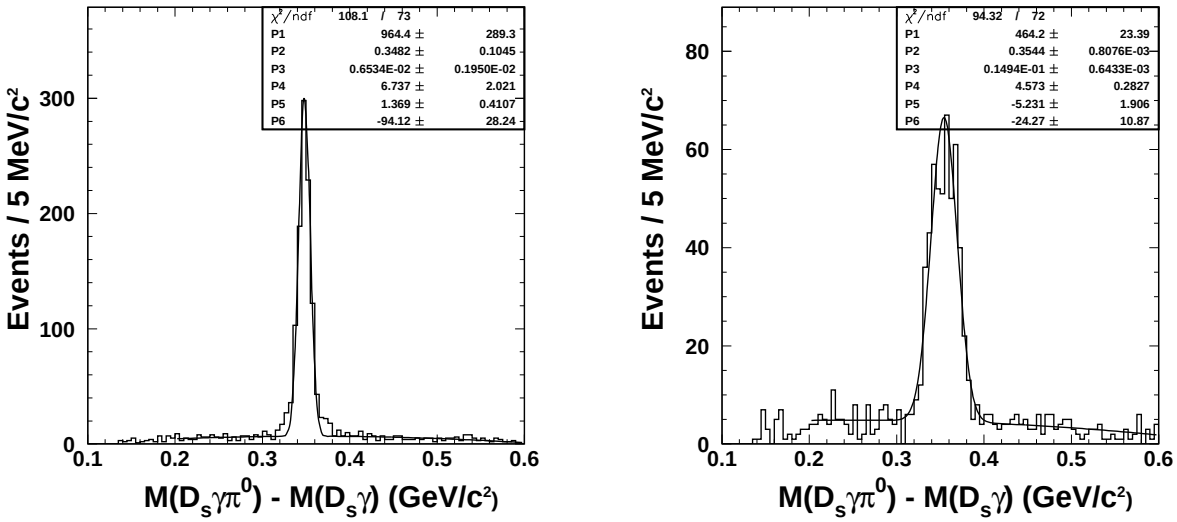

Figure 3.20: The mass difference spectra $\Delta M(D_s^*\pi^0)$ using $D_{sJ}(2460)^+ \to D_s^{*+}\pi^0$ (left) and $D_{sJ}^*(2320)^+ \to D_s^+\pi^0$ (right) signal MC. We have demonstrated that the width for $D_{sJ}(2460)^+ \to D_s^{*+}\pi^0$ would also be broader if there is feed up from $D_{sJ}^*(2320)$.

We can calculate the number of real $D_{sJ}^*(2317)^+ \to D_s^+\pi^0$ decays reconstructed in our data, denoted as R_0, as well as the number of real $D_{sJ}(2460)^+ \to D_s^{*+}\pi^0$ decays, denoted as R_1, using the unfolding method to take into account of the cross-feed

probabilities. The following linear equations relate the real to observed numbers:

$$N_0 = R_0 + f_1 R_1 \tag{3.1}$$

$$N_1 = R_1 + f_0 R_0 \,, \tag{3.2}$$

where N_0 and N_1 are the numbers of events extracted from a fit to the mass difference spectra $\Delta M(D_s\pi^0)$ and $\Delta M(D_s^*\pi^0)$ respectively, and R_0 and R_1 are the number of real decays produced times the efficiency to observe them in the corresponding signal decay modes. The coefficient f_0 is the probability that a $D_{sJ}^*(2317)$ feeds up to and is reconstructed as $D_s^*\pi^0$ while f_1 is the probability that a $D_{sJ}(2460)$ feeds down to and is reconstruced as $D_s\pi^0$.

We obtain $N_1 = 55.3 \pm 10.1$ for the number of events in the $D_s^*\pi^0$ final state from the fit to the peak in Figure 3.18(a) described above. For N_0, it is desirable to obtain a $D_s\pi^0$ sample selected with criteria that most closely match those used to select $D_s^*\pi^0$ combinations, and that is enriched in $D_{sJ}^*(2317)$ decays relative to feed down from $D_{sJ}(2460)$ decays. Thus we apply the same selection criteria that were used for the $D_s^*\pi^0$ sample, but without selecting the photon from the $D_s^* \to D_s\gamma$ transition. To extract the number of $D_{sJ}^*(2317) \to D_s\pi^0$ events, we fit the peak in the $\Delta M(D_s\pi^0)$ distribution to a Gaussian with its width fixed to the Monte Carlo expectation for $D_{sJ}^*(2317)$ decays. In this fit, a significant fraction of feed down contribution is counted as part of the combinatoric background rather than as signal. We obtain $N_0 = 189.5 \pm 18.9$ candidates which include the feed up contribution. The observed number of events as well as the mass difference and widths are summarized in Table 3.3.

Table 3.3: Observed numbers of events based on observed numbers and feed up and down.

Mode	Number Observed	ΔMass(MeV)	Gaussian Width (MeV)
$D_s\pi^0$	189.5 ± 18.9	350.5 ± 1.1	9.4 ± 0.9
$D_s^*\pi^0$	55.3 ± 10.1	349.8 ± 1.3	6.1 ± 1.0

As mentioned earlier, the probability $f_0 = 0.091 \pm 0.007 \pm 0.015$ for the probability that a reconstructed $D_{sJ}^*(2317) \to D_s\pi^0$ can be combined with a random photon to mimic a $D_{sJ}(2460) \to D_s^*\pi^0$ decay. This fraction counted by the fit is less than one due to the smearing of $\Delta M(D_s^*\pi^0)$ that results when an unrelated photon is added to the $D_s\pi^0$ system. The agreement between the data and Monte Carlo distributions in Figure 3.4 lends confidence in the modeling of extra photons. We assign a relative systematic uncertainty of 5% based on MC modeling of extra photons and on studies of combinations entering D_s^* side bands in data. To study the second source of systematic uncertainty, we have carried out fits to the $\Delta M(D_s^*\pi^0)$ distribution in which the width of the Gaussian signal function was fixed to $\pm 1\sigma$ relative to the central value obtained from the nominal fit. We assign a relative uncertainty on f_0 of 16% based on the resulting variation in event yields.

We obtain $f_1 = 0.84 \pm 0.04 \pm 0.10$ from Monte Carlo simulations as mentioned earlier for the feed down. If all $D_{sJ}(2460) \to D_s^*\pi^0$ decays with a reconstructed D_s plus π^0 combination were to be counted as $D_{sJ}^*(2317)$ decays, f_1 would simply be one divided by the acceptance for finding the photon from the $D_s^* \to D_s\gamma$ transition. However, because the $\Delta M(D_s\pi^0)$ distribution for the feed down background

is broadened, a significant fraction of these combinations are not counted as part of the Gaussian signal, instead being absorbed into the polynomial background. The contributions to the relative systematic error on f_1 are estimated to be 5% from the uncertainty on the photon-finding efficiency and 11% from the uncertainty on the probability of feed down, obtained by performing alternate fits to the $\Delta M(D_s\pi^0)$ distribution.

Solving for R_0 and R_1 from Equations 3.1 and 3.2 with other variables measured above, we find that $R_0 = 155 \pm 23$ events and $R_1 = 41 \pm 12$ events, where the uncertainties include both statistical and systematic sources. The non-zero events for R_1 demonstrate the existence of a state at 2463 MeV/c^2. We notice that the $D_{sJ}^*(2317)$ feed up background is only a minor background to the narrow peak for the $D_{sJ}(2460)$ observed in Figure 3.18(a). The significance of the signal for this state, accounting for statistical and systematic errors, is determined to be in excess of 5σ by computing the probability for the combinatoric background plus the feed up background to fluctuate up to give the observed yield in the signal region in Figure 3.18(a). A more detailed discussion regarding the significance of the $D_{sJ}(2460)$ is described in Section 3.4.2.

Using Equation 3.1 and the values obtained above, the fraction of real $D_{sJ}^*(2317)$'s of the number observed is

$$1 - \frac{f_1 R_1}{N_0} = 0.82 \pm 0.06. \tag{3.3}$$

Thus, the yield gives rise to the real yield, taking into account feed down from the $D_{sJ}(2460)$, for the $D_{sJ}^*(2317)$ of $(165 \pm 26) \times (0.82 \pm 0.06) = 135 \pm 23$. The efficiency for this selection is 0.0973 ± 0.0057 giving a yield over efficiency of 1326 ± 249 signal

events.

3.4.2 Further Evidence for the $D_{sJ}(2460)^+ \to D_s^*\pi^0$ Decay

Accounting of the cross-feed backgrounds leads to the conclusion that both the $D_{sJ}^*(2317)$ and the $D_{sJ}(2460)$ states exist. To provide further support for this conclusion, we use the D_s^* side band regions in the $D_s\gamma\pi^0$ data sample to estimate the feed up background in Figure 3.18(a) due to $D_{sJ}^*(2317)^+ \to D_s^+\pi^0$ plus random photon combinations. Only a small enhancement in the $M(D_s\gamma\pi^0) - M(D_s\gamma)$ distribution of Figure 3.18(b) is evident in the region of the $D_{sJ}(2460)$. Hence we demonstrate that only a small fraction of the background from $D_{sJ}^*(2317)$ decays contributes to the $D_{sJ}(2460)$ peak.

In addition, we have studied the lineshapes of the peaks to help untangle cross feed contributions. We performed a binned likelihood fit of the spectrum in Figure 3.18(a) to a Gaussian signal shape and a background function, which consists of a second-order polynomial function and the spectrum from the D_s^* side band region in Figure 3.18(b) with its normalization fixed. Figure 3.21 shows the fit to the $D_s^*\pi^0$ Signal where we allow all parameters to float, except for the sideband histogram. The fit returns a yield of 42 ± 10 for the $D_s^*\pi^0$ signal, which agrees very well with the 41 ± 11 events from the cross-feed calculation and with the 46 ± 12 events from the D_s side band subtracted fit as shown in Figure 3.22.

Also shown in the same Figure 3.21 is a fit where we fixed the number of signal events to be zero. The bottom plot in Figure 3.21 shows values of log likelihood function versus the number of signal events. From the change in the likelihood of

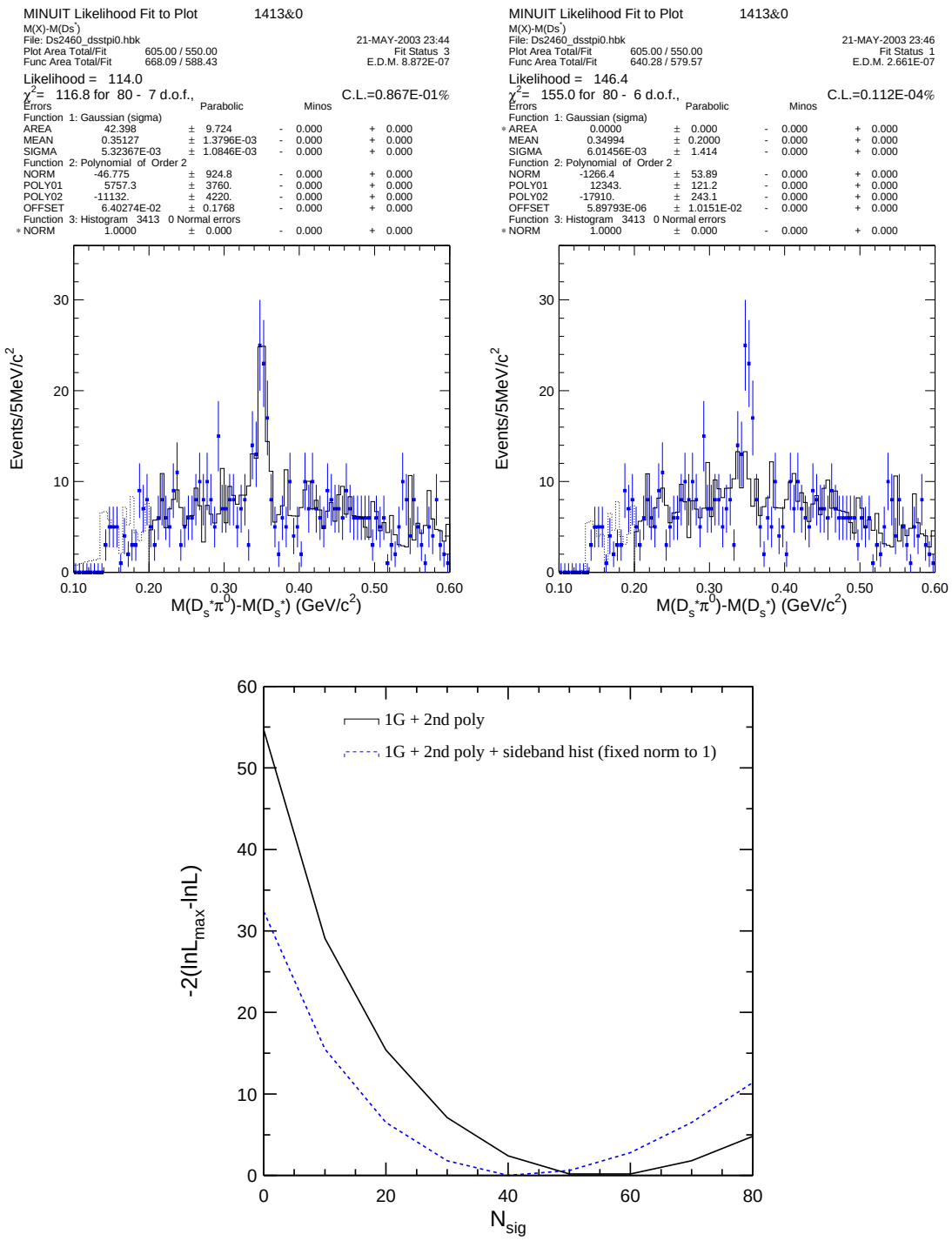

Figure 3.21: Finding out the significance of the $D_s^*\pi^0$ signal: (Top left) Fit with Gaussian function for signal, 2nd order polynomial function plus sideband spectrum for background; (Top right) Fit with same function but with number of signal fixed to be zero; (Bottom) Value of log likelihood function vs number of signals.

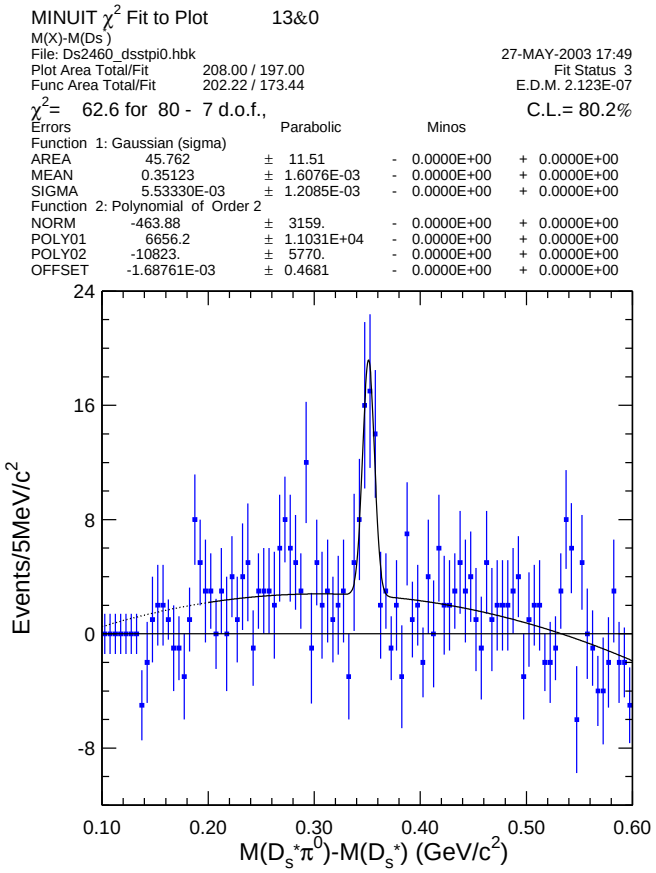

Figure 3.22: The mass difference spectra $\Delta M(D_s^*\pi^0)$ results from the subtraction of Figure 3.18(b) from Figure 3.18(a).

fits performed with and without the $D_{sJ}(2460)$ signal contribution, we infer that the statistical significance of the signal is $\sqrt{146.4 - 114} = 5.7\,\sigma$.

Finally we also find that the width of the $D_{sJ}(2460)$ peak in Figure 3.18(a) is $\sigma = 6.1 \pm 1.0$ MeV/c^2, consistent with the detector resolution. If the origin of this peak was feed up from $D^*_{sJ}(2317)^+ \to D^+_s\pi^0$ decays, then including random photons to form $D^*_s\pi^0$ candidates would result in smearing of the $\Delta M(D^*_s\pi^0)$ distribution, in the same way that the feed down background to the $D^*_{sJ}(2317)$ state is broadened as described in Section 3.4.1. Thus, the narrowness of the peak in Figure 3.18(a) also rules out the possibility that the peak is dominantly due to feed up from $D^*_{sJ}(2317)^+$ decays.

3.5 Searches for $D_{sJ}(2460)$ in Other Decay Modes

Similiarly to Section 3.3, we explore the decay dynamics of the $D_{sJ}(2460)$ by searching for other strong decay and electromagnetic decay modes. We have searched again in the decay modes $D_s\gamma$, $D^*_s\gamma$, $D_s\pi^+\pi^-$, and $D^*_{sJ}(2317)\gamma$ as described in the following subsections.

3.5.1 Decays to $D_s\gamma$

The event selection criteria are the same as those in Section 3.3.1. From a sample of 29,892 signal MC events for $D_s(2460)^+ \to D^+_s\gamma$, we obtained a reconstruction efficiency of $(19.8 \pm 0.4)\%$ for $P(D_s\gamma) > 3.5$ GeV/c obtained from fit to signal MC in Figure 3.23. We learned from signal MC that the width of the Gaussian is very wide.

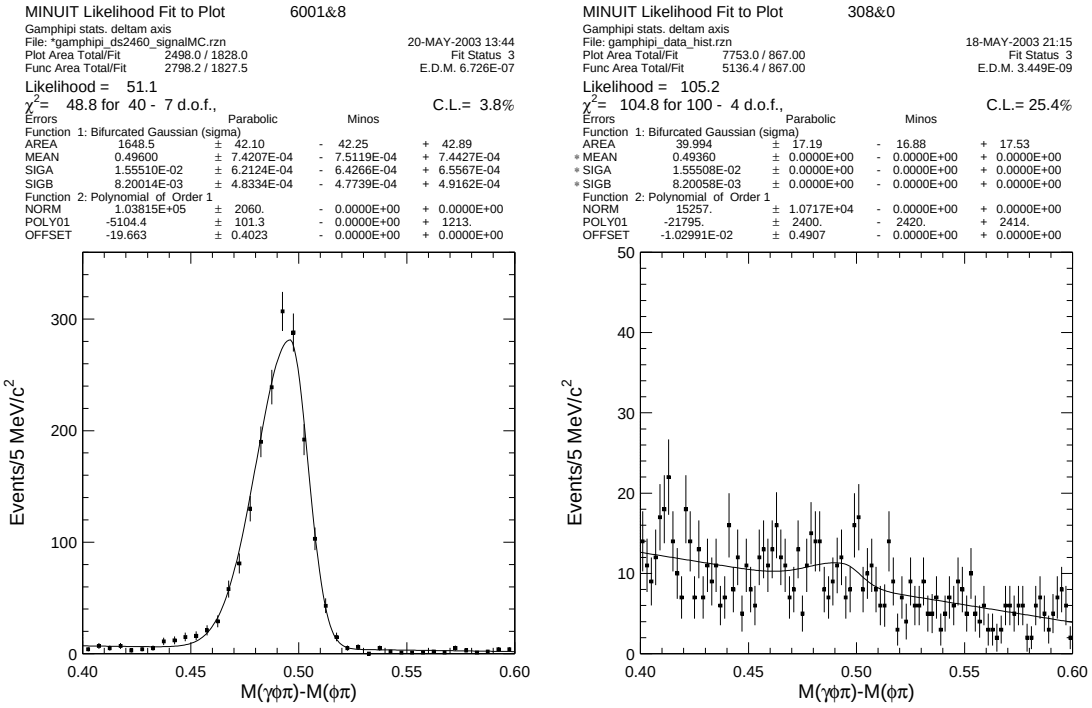

Figure 3.23: The fit to mass difference $M(D_s\gamma) - M(D_s)$ for $D_s(2460)^+ \to D_s^+\gamma$ signal MC (left) and data (right).

From a likelihood fit with a signal shape obtained from MC, we find 40 ± 17 events in the signal region for the data. An excess of combinations in the signal region becomes more evident in a coarser binning of the mass difference $M(D_s\gamma) - M(D_s)$ distribution as shown in Figure 3.24 . From fits performed with and without the signal

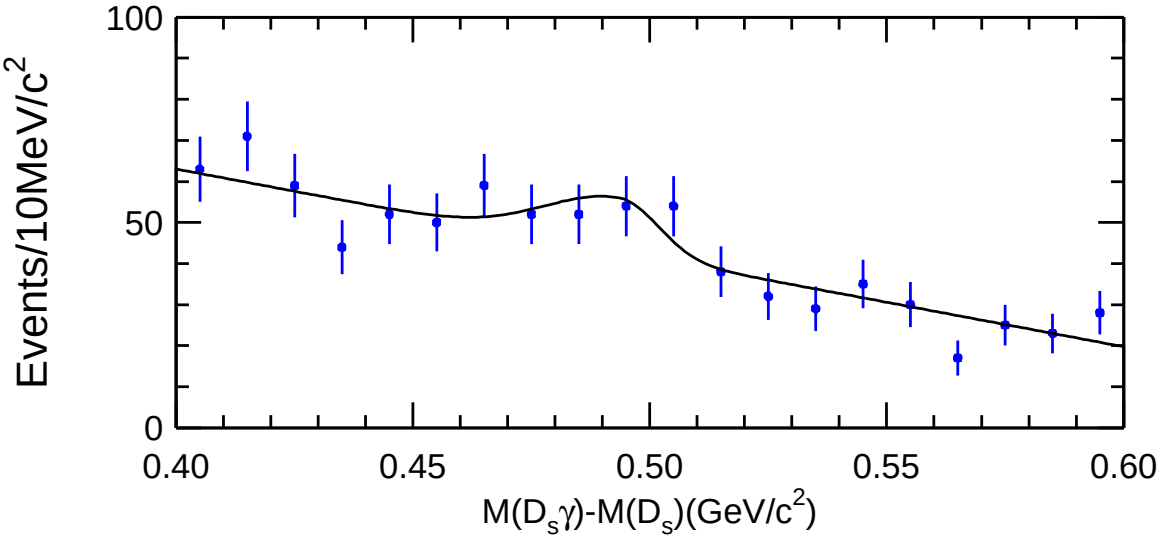

Figure 3.24: The mass difference $M(D_s\gamma) - M(D_s)$ in data. This plot shows the region (around 496 MeV) where we expect to see $D_s(2460)^+ \to D_s^+\gamma$ if this decay does happen.

Gaussian, we determine that the statistical significance of this excess is 2.4 standard deviations which is too small to claim as an observation. Therefore, we report an upper limit on the decay $D_{sJ}(2460)^+ \to D_s^+\gamma$ relative to $D_{sJ}(2460)^+ \to D_s^{*+}\pi^0$ listed in Table 3.4.

3.5.2 Decays to $D_s^*\gamma$

We search for the decay of $D_s(2460) \to D_s^*\gamma$ with $D_s^* \to D_s\gamma$, $D_s \to \phi\pi$, $\phi \to K^+K^-$. The event selection for $D_s^* \to D_s\gamma$ is the same as the mode described earlier in Section 3.3.2.

We use the D_s signal region $1.9565 < M(D_s) < 1.9805$ GeV/c^2, and D_s^* signal region where the $M(D_s^*) - M(D_s)$ is within ± 13 MeV of the PDG value [32]. To determine the reconstruction efficiency, we use a sample of 29,553 signal MC events of $D_s(2460) \to D_s^*\gamma$, $D_s^* \to D_s\gamma$, $D_s \to \phi\pi$, $\phi \to K^+K^-$. We measured an overall efficiency of $(2.52 \pm 0.09)\%$ over the entire momentum spectrum and $(9.14 \pm 0.32)\%$ for the portion of the $D_s^*\gamma$ momentum above 3.5 GeV/c. Figure 3.25 shows the fits and event yield used to obtain an upper limit on the decay $D_{sJ}(2460)^+ \to D_s^{*+}\gamma$ relative to $D_{sJ}(2460)^+ \to D_s^{*+}\pi^0$. When fitting to data, the mean of the Gaussian is fixed to measured value from the $D_s^*\pi^0$ mode, while the sigma is fixed to the MC fit value.

3.5.3 Decays to $D_s\pi^+\pi^-$

The event selection criteria are the same as those in Section 3.3.3. The reconstruction efficiency of $(19.47 \pm 1.48)\%$ and the expected resolution are obtained from signal MC events of $D_s(2460)^+ \to D_s^+\pi^+\pi^-$. Similarly, we fit the mass difference in Figure 3.26 for a yield to calculate an upper limit for $D_s(2460)^+ \to D_s^+\pi^+\pi^-$ relative to $D_{sJ}(2460)^+ \to D_s^{*+}\pi^0$ listed in Table 3.4.

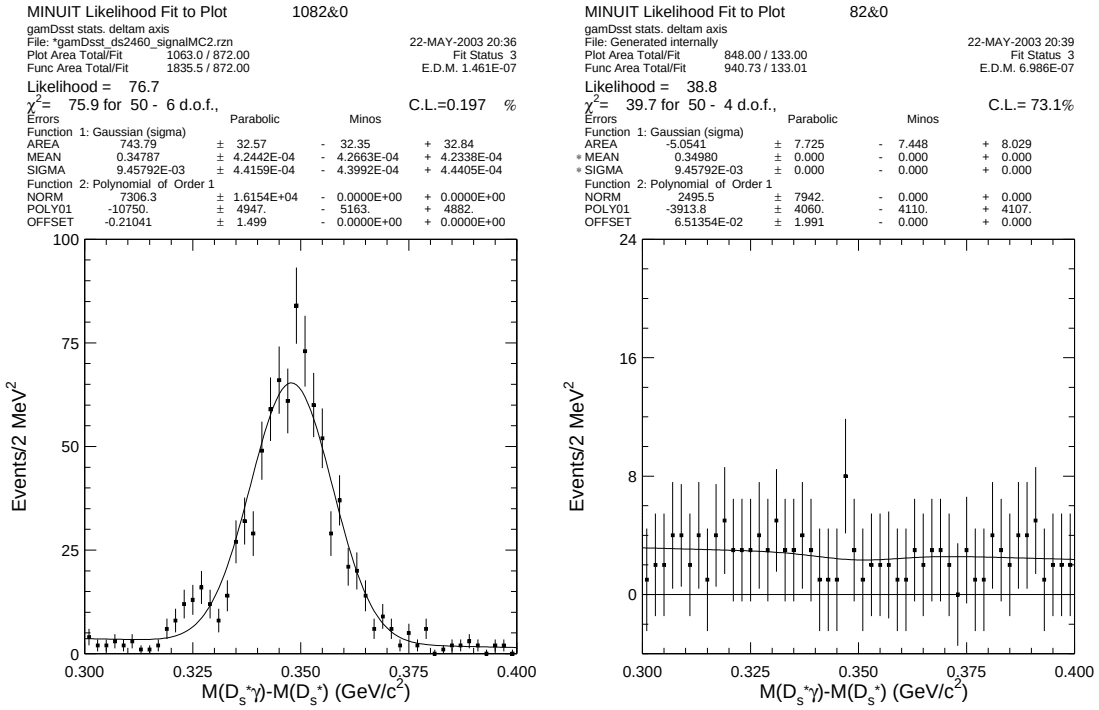

Figure 3.25: $D_s(2460)^+ \to D_s^{*+}\gamma$, $D_s^{*+} \to D_s^+\gamma$, $D_s^+ \to \phi\pi^+$, $\phi \to K^+K^-$ in signal MC (left) and CLEOII+II.V data (right).

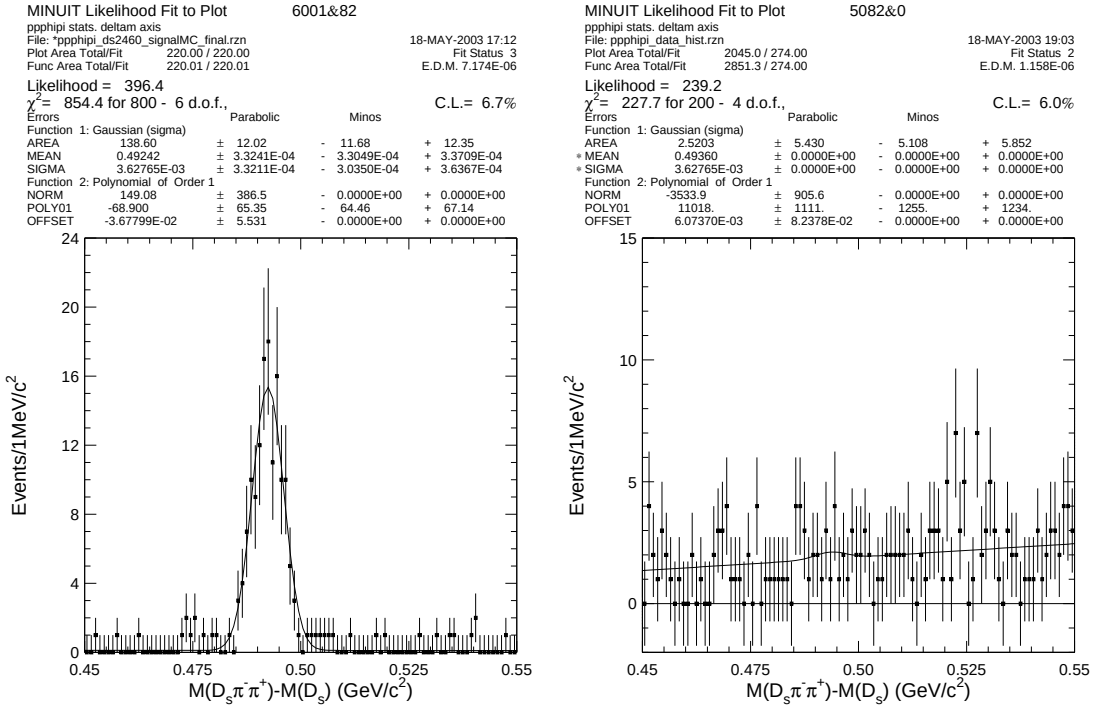

Figure 3.26: $D_s(2460)^+ \to D_s^+\pi^+\pi^-$, $D_s^+ \to \phi\pi^+$, $\phi \to K^+K^-$ in signal MC (left) and CLEOII+II.V data (right). When fitting data, the mean is fixed to the value extracted from $D_s\pi^0$, and the sigma of the Gaussian is fixed according to the MC fit values.

3.5.4 Decays to $D^*_{sJ}(2317)\gamma$

If the $D_{sJ}(2460)^+$ is a 1^+ state, then it is also possible for it to undergo a P-wave radiative decay to $D^*_{sJ}(2317)^+\gamma$ [35]. We searched but found no evidence for $D_{sJ}(2460)^+ \to D^*_{sJ}(2317)^+\gamma$. The detailed description of this search in our $D_s\gamma\pi^0$ sample is documented in the internal note [34] for CLEO. The 90% C.L. upper limit for this mode is also included in Table 3.4.

3.5.5 Summary of Different Decay Modes for $D_{sJ}(2460)$

If the $D^*_{sJ}(2317)$ was the $J^P = 0^+$ $c\bar{s}$ meson as proposed, $D_{sJ}(2460)$ might be the other missing $J^P = 1^+$ $c\bar{s}$ state. For a state with $J^P = 1^+$, the $D_s\pi^+\pi^-$ decay mode, as well as both radiative decay modes $D_s\gamma$ and $D^*_s\gamma$ are allowed. From the searches of these decay modes described in previous sections, we find no evidence of decays to any of these final states. We summarize the limits obtained on these decays, relative to $D^*_s\pi^0$, in Table 3.4.

Szczepaniak [18] suggests that the resonance at 2.32 GeV/c^2 is a $D\pi$ atom. If this theory is true, we should be able to observe structures in $D^+_s\pi^-$ final state. Unlike $D^+_s\pi^0$, $D^+_s\pi^-$ can not be strong decay products due to the quark content, $c\bar{s}\bar{u}d$. CLEO [34] searched for the $D^+_s\pi^-$ and $D^{*+}_s\pi^-$ decay modes, but there is no significant peak at for the M($D_s\pi$)$-$ M(D_s) spectrum. Thus the $D_s\pi$ atom model is unlikely to be the nature of $D^+_s\pi^0$ and $D^{*+}_s\pi^0$ resonances.

Table 3.4: 90% CL upper limits on the ratio of branching fractions for $D_{sJ}(2460)$ to the decay modes shown relative to the $D_s^{*+}\pi^0$ state. Also shown are the theoretical expectations from Ref. [17], under the assumption that the $D_{sJ}(2460)$ is the lowest-lying 1^+ $c\overline{s}$ meson.

Final State	Yield	Efficiency	Limit (90% CL)	Prediction
$D_s^{*+}\pi^0$	41 ± 11	$(6.0 \pm 0.2)\,\%$	—	
$D_s^{+}\gamma$	40 ± 17	$(19.8 \pm 0.4)\,\%$	< 0.49	0.24
$D_s^{*+}\gamma$	-5.1 ± 7.7	$(9.1 \pm 0.3)\,\%$	< 0.16	0.22
$D_s^{+}\pi^+\pi^-$	2.5 ± 5.4	$(19.5 \pm 1.5)\,\%$	< 0.08	0.20
$D_{sJ}^{*}(2317)\gamma$	3.6 ± 3.0	$(2.0 \pm 0.1)\,\%$	< 0.58	0.13

3.6 Properties of the $D_{sJ}^{*}(2317)^+$ and $D_{sJ}(2460)^+$ States

After untangling of the cross contamination for the two narrow resonances, we are now ready to further address properties of the $D_{sJ}^{*}(2317)^+$ and $D_{sJ}(2460)^+$ States.

3.6.1 Mass and Width of the $D_{sJ}^{*}(2317)^+$

In Section 3.2.2, our measurement of the width for the peak in Figure 3.4 is $\sigma = 8.0^{+1.3}_{-1.1}$ MeV/c^2, somewhat larger than our mass difference resolution, $\sigma = 6.0 \pm 0.3$ MeV/c^2. The difference in resolution is consistent with predictions from Monte Carlo simulations where we include both $D_{sJ}(2460)$ and $D_{sJ}^{*}(2317)$ production. Approximate 18% of the observed $D_s^{+}\pi^0$ decays in the $D_{sJ}^{*}(2317)$ signal region enter as feed down from the $D_{sJ}(2460)$ state, resulting in smearing of the width (14.9 ± 0.4

MeV/c^2) as discussed in Section 3.4.1

After eliminating the feed down background from the $D_{sJ}(2460)$, we should be able to obtain a better measurement of the mass and natural width for the $D^*_{sJ}(2317)^+$. One approach to do so is to perform a binned likelihoood fit in the mass spectrum for $\Delta M(D_s\pi^0)$ with two Gaussians in Figure 3.27, one for the $D^*_{sJ}(2317)$ signal, and one to account for the feed down from the $D_{sJ}(2460)$. Allowing the means and widths of both Gaussians to float as shown in the second plot of Figure 3.10, we measure $\overline{\Delta M}$ for the $D^*_{sJ}(2317)$ to be 350.0 ± 1.2 MeV/c^2 with a width of 6.0 ± 1.2 MeV/c^2. The mean and width for the feed down contribution are 344.9 ± 6.1 MeV/c^2 and 16.5 ± 6.3 MeV/c^2, respectively. The two Gaussian fit gives an area of 107 ± 35 and 81 ± 39 for the narrow and wide Gaussian, respectively. In comparison, we have 165 ± 26 $D^*_{sJ}(2317)$ events and 55 ± 10 $D_{sJ}(2460)$ events reconstructed, and using the feed down and up rates from Section 3.4.1 we get 135 ± 23 real $D^*_{sJ}(2317)$'s, which is in agreement with the two Gaussian fit.

We have also carried out fits in which one or both of the widths of the Gaussians were fixed to values determined by the Monte Carlo. In all cases the results were consistent with the results from the fit described above. We have also tried to obtain a purer $D^*_{sJ}(2317)$ sample by vetoing combinations with photons that can be combined with the D_s candidate to form a D^*_s, thereby removing some of the feed down background from the $D_{sJ}(2460)$. This veto marginally improves the $D_s\pi^0$ signal when we fit with two Gaussians, and the mass and width change by only a small fraction of the statistical uncertainty. The systematic uncertainty for $\langle \Delta M(D_s\pi^0) \rangle$ receives contributions from uncertainties in the characterization of the $D_{sJ}(2460)$ feed down and

MINUIT Likelihood Fit to Plot 5082&0
pi0phipi stats. deltam axis
File: pi0phipi_data_e9oe25_barrel_hist.rzn 19-MAY-2003 09:10
Plot Area Total/Fit 1994.0 / 1421.0 Fit Status 3
Func Area Total/Fit 2568.5 / 1421.0 E.D.M. 1.245E-08

Likelihood = 66.7
χ^2= 66.6 for 80 - 10 d.o.f., C.L.= 59.4%

Errors		Parabolic	Minos	
Function 1: Gaussian (sigma)				
AREA	106.94	± 35.38	- 39.41	+ 0.0000E+00
MEAN	0.35003	± 1.2474E-03	- 1.2027E-03	+ 1.3577E-03
SIGMA	5.97283E-03	± 1.1838E-03	- 1.1336E-03	+ 1.3571E-03
Function 2: Gaussian (sigma)				
AREA	81.261	± 39.28	- 0.0000E+00	+ 39.82
MEAN	0.34490	± 6.0795E-03	- 0.0000E+00	+ 0.0000E+00
SIGMA	1.65240E-02	± 6.3016E-03	- 0.0000E+00	+ 0.0000E+00
Function 3: Polynomial of Order 2				
NORM	-3.30482E+05	± 4627.	- 0.0000E+00	+ 0.0000E+00
POLY01	81207.	± 556.4	- 0.0000E+00	+ 0.0000E+00
POLY02	-4934.5	± 65.46	- 0.0000E+00	+ 0.0000E+00
OFFSET	-8.1395	± 0.1286	- 0.0000E+00	+ 0.0000E+00

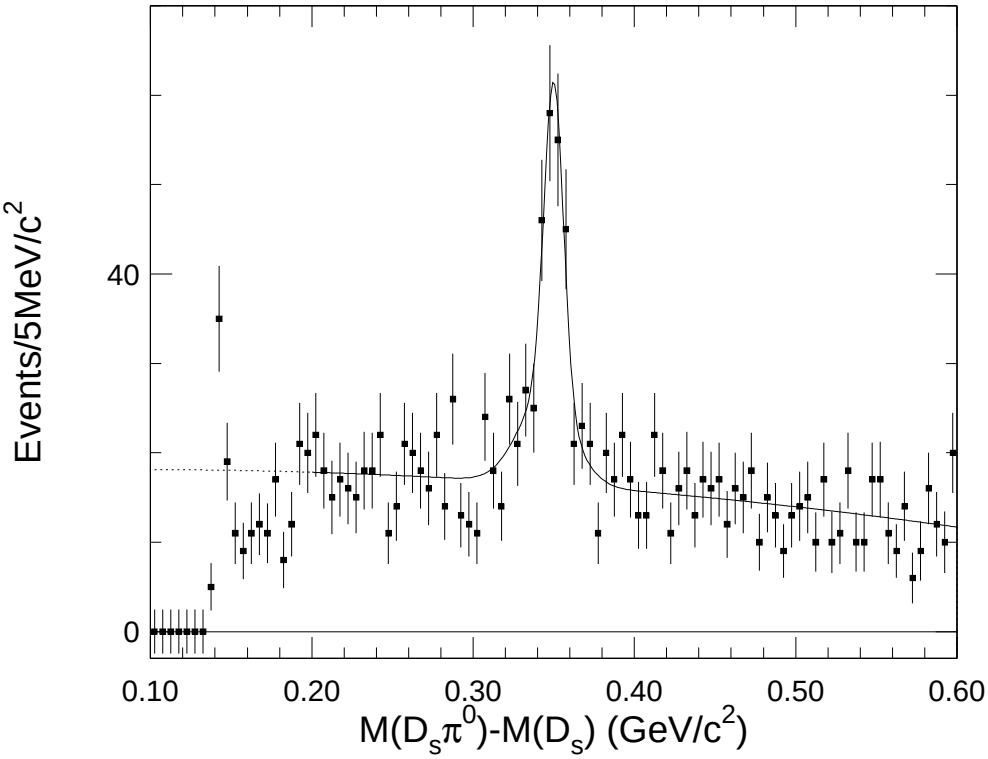

Figure 3.27: The fit to the mass difference distributions in $D^*_{sJ}(2317) \to D_s\pi^0$ data with two Gaussian.

from uncertainties in the modeling of the energy resolution of the calorimeter. We estimate the total systematic error on the mass difference to be 1.0 MeV/c^2. Based on these studies, we limit the natural width of the $D_{sJ}^*(2317)$ to be $\Gamma < 7$ MeV at the 90% confidence level (C.L.).

3.6.2 Mass and Width of the $D_{sJ}(2460)^+$

From the fit to the side band subtracted distribution in Figure 3.22 reported in Section 3.4.2, we obtain $\langle \Delta M(D_s^*\pi^0) \rangle = 351.2 \pm 1.7 \pm 1.0$ MeV/c^2 for the mass difference between the $D_{sJ}(2460)$ and the D_s^*. The first error is statistical and the second is the systematic uncertainty which is the same as that presented in the previous section for the $D_{sJ}^*(2317) - D_s$ mass difference. From our fits to data and Monte Carlo $\Delta M(D_s^*\pi^0)$ distributions, we also infer a 90% C.L. upper limit on the natural width (Γ) of the $D_{sJ}(2460)^+$ state to be 7 MeV. Based on the event yields and detection efficiencies given above, we can determine the production rate times branching fraction for the $D_{sJ}(2460)$ state to that of the $D_{sJ}^*(2317)$. We find this to be approximately 40% for momenta above 3.5 GeV/c.

3.7 Conclusions and Discussion

In summary, we have confirmed the existence of the new narrow resonance, known as the $D_{sJ}^*(2317)$, that was first observed by the BaBar experiment. Like BaBar, we observe this state in the $D_s^+\pi^0$ decay mode with a mass near 2.32 GeV/c^2. We have performed studies to demonstrate that the peak in the $D_s^+\pi^0$ mass spectrum

attributed to this state is not a kinematic reflection from other known particles. We have set upper limits on other decay modes of this state as summarized in Table 3.2. We have measured the mass splitting of this state with respect to the D_s meson to be 350.0 ± 1.2 [stat.] ± 1.0 [syst.] MeV/c^2, and we find its natural width to be $\Gamma < 7$ MeV at 90% C.L.

We have also observed and established the existence of a second new narrow state with a mass near 2.46 GeV/c^2 decaying to $D_s^{*+}\pi^0$, which we have denoted as the $D_{sJ}(2460)$ meson. We have demonstrated that the signal for this decay cannot be interpreted as a reflection from the $D_{sJ}^*(2317)^+ \to D_s^+\pi^0$ decay. We have set upper limits on other decay modes of the $D_{sJ}(2460)$ as summarized in Table 3.4. We have measured the mass splitting of this state with respect to the D_s^* meson to be 351.2 ± 1.7 [stat.] ± 1.0 [syst.] MeV/c^2. The natural width of this state is found to be $\Gamma < 7$ MeV at 90% C.L.

The existence of the $D_{sJ}(2460)$ [36] has been confirmed by the BaBar [37] and Belle [38] collaborations. Furthermore, with a larger data sample, Belle [39] first observed and BaBar [40] later confirmed $D_{sJ}(2460) \to D_s\gamma$ and measured the helicity angular distribution for the decay $B \to DD_{sJ}(2460)$ with $D_{sJ}(2460) \to D_s\gamma$. This is a strong support for its interpretation as a 1^+ $c\bar{s}$ state because the helicity angle distribution rules out a $J = 2$ assignment. BaBar [41] and Belle [38] both observed $D_{sJ}(2460)^+ \to D_s^+\pi^+\pi^-$, which is allowed if the $D_{sJ}(2460)$ is a 1^+ state. Since the $D_{sJ}(2460)$ mass lies above the kinematic threshold for decay to DK (but not for D^*K), the narrow width suggests this decay does not occur. Since angular momentum and parity conservation laws forbid a 1^+ state from decaying to two pseudoscalars,

this provides additional evidence for the compatibility of the $D_{sJ}(2460)$ with the $J^P = 1^+$ hypothesis.

Furthermore, if we take the difference between the two mean mass differences reported above, we obtain $\delta(\Delta M) = (351.2 \pm 1.7) - (350.0 \pm 1.2) = 1.2 \pm 2.1$ MeV/c^2 for the difference between the $1^+ - 1^-$ and $0^+ - 0^-$ mass splittings, where the dominant uncertainty is due to statistics. The results are compatible with models [17, 24] based on HQET and chiral symmetry that the 1^+ and 0^+ states are the chiral partners of the 1^- and 0^- states, with the same mass splitting.

In the simplest interpretation of these results, both new particles are bound states of a charm quark c and an anti-strange quark $\overline{s}$ with $D^*_{sJ}(2317)$ being the 0^+ member of the lowest-lying P-wave $c\overline{s}$ multiplet and $D_{sJ}(2460)$ as the 1^+ partner of the 0^+ state, both with light quark angular momentum of $j = 1/2$. If this interpretation is correct, we have completed the spectroscopy of low-lying $c\overline{s}$ mesons. The experimental observation of this "parity-doubling" effect has significant implications for the spectroscopy of heavy hadrons, as well as practical implications for studies of B meson decays to charm.

CHAPTER 4

Leptonic Decays of D_s Mesons

4.1 Experimental Status of Leptonic D_s Decay

There has been a total of seven reported measurements of f_{D_s}, ranging from 190 to 450 MeV as shown in Table 4.1. The first indication of $D_s \to \mu\nu$ was presented in

Table 4.1: Summary of measurements of the decay constants for the D_s.

Experiment	Observed events	Published f_{D_s} (MeV)
ALEPH (2002) [42]	553 ± 93	$285 \pm 19 \pm 40$
Beatrice (2000) [43]	18	$323 \pm 44 \pm 36$
CLEO (1998) [44]	182 ± 22	$280 \pm 19 \pm 28 \pm 34$
E653 (1996) [45]	$23.2 \pm 6^{+1.0}_{-0.9}$	$194 \pm 35 \pm 20 \pm 14$
BES (1995) [46]	3	$430^{+150}_{-130} \pm 40$
CLEO (1994) [47]	39 ± 8	$344 \pm 37 \pm 52 \pm 42$
WA75 (1993) [48]	8	$232 \pm 45 \pm 52$

1992 by the WA75 collaboration [48] in a fixed-target experiment with a π^- beam at the European Center for Nuclear Research (CERN). The first measurement from

an e^+e^- colliding experiment is CLEO's measurement [47] with $2.13fb^{-1}$ of data in 1994. Based on a similar measurement technique with $4.79fb^{-1}$ of data, including the previous subset of data, CLEO [44] made an improved measurement for the ratio $B(D_s \to \mu\nu)/B(D_s \to \phi\pi) = 0.173 \pm 0.023 \pm 0.035$. Using Eq. 1.1 and Eq. 1.3 along with the D_s lifetime and the other quantities shown in the equations, f_{D_s} was extracted to be 280±19±28±34 MeV, which is the most precise existing measurement. The first error is statistical, the second is the experimental systematic error. The third error reflects the uncertainty in the knowledge of the absolute branching fraction for $D_s \to \phi\pi$, which was used as the normalization mode to infer the number of produced D_s mesons.

The E653 collaboration at Fermilab used an emulsion target and muon trigger to observe events in a fixed-target experiment. The normalization mode $D_s \to \phi\mu\nu$ was used to obtain the branching fraction for $D_s \to \mu\nu$ and $D_s \to \tau\nu$ and then extract f_{D_s}.

Another measurement was made by the BES Collaboration [46]. They fully reconstructed D_s meson produced at threshold in the e^+e^- collisions, and obtained f_{D_s} to be $430^{+150}_{-130} \pm 40$ MeV based on one actual $D_s \to \mu\nu$ event together with two $D_s \to \tau\nu$ events, assuming $\tau - \mu$ universality. The first errors are statistical; the second are systematic resulting from uncertainties in lepton mode detection efficiencies, background estimates, and the D_s lifetime.

The latest measurement is from the ALEPH Collaboration [42] based on a sample of $e^+e^- \to Z \to c\bar{c}$ decays. Their measurement of $f_{D_s} = 285 \pm 19 \pm 40$ combined results from two analyses of $D_s \to \tau\nu$ and a $D_s \to \mu\nu$ analysis. This measurement

is also limited by the uncertainty on the absolute scale of branching fractions for hadronic D_s decays.

Both statistical and systematic uncertainties in the reported measurements for the decay rates are large; therefore, a better measurement is needed to extract CKM information precisely. The measurements made by WA75, E653, CLEO, and ALEPH described above depend heavily on normalization, so their systematic uncertainty are subject to the contribution from the normalization mode. The technique used in the BES measurement does not require a normalization mode, but is subject to statistics. CLEO-c will be producing D_s mesons at threshold for higher statistics, and will be able to make a more precise measurement. Until then, we are limited by both systematic and statistical uncertainties. Nevertheless, the goal of the analysis is to reduce systematic errors with the additional $9fb^{-1}$ of $\Upsilon(4S)$ data available for analysis.

4.2 Analysis Method for $D_s \to \mu\nu$

4.2.1 General Approach

We start by replicating the methods used in the previous CLEO measurement [44] for $D_s \to \mu\nu$, and then we implement new optimized strategies to investigate systematic uncertainties and suppress background.

Using a neutrino reconstruction method based on missing energy and momentum to be discussed in detail in section 4.2.4, we identify a sample of $D_s^{*+} \to \gamma D_s^+$, $D_s^+ \to \mu^+\nu_\mu$ candidates, for which both the muon and photon can be detected.

Neutrinos cannot be measured directly, therefore we reconstruct them by using the conservation of momentum and energy, and assume that the missing momentum and energy are from a neutrino.

With information from the lepton, photon, and neutrino, we can fully reconstruct the decay chain $D_s^{*+} \to \gamma D_s^+$, $D_s^+ \to \mu^+\nu$[1], and calculate the mass difference between the D_s^* and the D_s candidate systems:

$$\Delta M = M(\gamma\mu\nu) - M(\mu\nu). \tag{4.1}$$

By using the mass difference as a signal, the relatively large errors from the neutrino reconstruction will mostly cancel. The ΔM distribution for the signal events should peak at $M(D_s^*) - M(D_s) \approx 143.8 MeV/c^2$ [1]. The signal shape and efficiency are studied using Monte Carlo sample as discussed in Section 4.2.7.

Muons provide a very distinct signature for the weak leptonic decay; however, the signal is subject to tremendous backgrounds from semileptonic decays of B and D mesons. We will use the electron data to estimate these backgrounds, assuming lepton universality noting that the $D_s \to l\nu$ is distinct by virtue of the helicity suppression. Furthermore, another source of background is the misidentification of hadrons as leptons. Section 4.2.6 will discuss in detail the background estimation.

To obtain the signal yield, we perform fits to the mass difference distribution using the signal and background function determined from either Monte Carlo or data whenever possible. To avoid biasing the analysis, we do not look at the muon data until the selection criteria are determined and when we are ready to perform

[1] Charge conjugations are implied throughout.

fits. Combining the results of the fits in Section 4.4 and the normalization mode $D_s^* \to \gamma D_s, D_s \to \phi\pi$ discussed in Section 4.3, we will be able to measure the ratio of the branching fraction $B(D_s^+ \to \mu^+\nu_\mu)/B(D_s^+ \to \phi\pi^+)$, from which the pseudoscalar decay constant f_{D_s} can be extracted.

4.2.2 Data Samples

The analysis discussed in this note is based on a sample of $13.4 fb^{-1}$ of e^+e^- collisons collected between 1990 and 1999 with the CLEO II detector [30] at the Cornell Electron Storage Ring (CESR). Among the datasets, $4.7 fb^{-1}$ was taken with the CLEOII configuration, and $8.7 fb^{-1}$ with the CLEOII.V configuration. This data sample is about three times larger than the subset of data used in the previous CLEO analysis in 1998. It is worth mentioning that the previous CLEO analysis was based on the CLEOII detector configuration with an earlier version of the event reconstruction software packages, in particular employing different track reconstruction and parameter fitting algorithms.

The Monte Carlo Samples

Samples of Monte Carlo (MC) events are generated to study the mass difference ΔM signal and background shapes, to evaluate detection efficiency, as well as for use in neutrino reconstruction cross-checks and lepton studies as discussed in later sections. Table 4.2 is a summary of all the MC samples we generated for this analysis. The momentum of all particles in CLEOII signal generator-level MC events without any cuts applied is shown in Figure 4.1. Keep in mind that there is no detector simulation

Table 4.2: Summary of Monte Carlo samples used in this analysis.

Mode	Events generated		Purpose/Comments
	CLEOII	CLEOII.V	
$D_s^* \to \gamma D_s, D_s \to \mu\nu$	284,090	351,778	signal shape and efficiency
$D_s^* \to \pi^0 D_s, D_s \to \mu\nu$	16,697	35,418	π^0 background shape
$D_s^* \to \gamma D_s, D_s \to \phi\pi$	452,850	520,530	normalization mode
$D^{*0} \to \gamma D^0$, $D^0 \to K^-\pi^+$	321,162	344,265	neutrino cross-check
$D^{*0} \to \pi^0 D^0$, $D^0 \to K^-\pi^+$	250,743	529,919	neutrino cross-check
$D \to K_L^0 l\nu$	149,985	0	phase space and external bremsstrahlung
$D^{*+} \to \pi^+ D^0$, $D^0 \to K^-\pi^+$	250,141	345,157	neutrino cross-check, decay in flight
Direct $D_s \to \mu\nu$	170,000	0	background shape
$D_s^{*+} \to D_s^+\gamma$, $D_s^+ \to \tau\nu$, $\tau \to \mu\nu\bar{\nu}$	10,163	0	background shape

taking place at the generator-level yet. To study background, we used the generic continuum MC samples with equivalent luminosities of $14.3 fb^{-1}$ for CLEOII and $26.3 fb^{-1}$ for CLEOII.V.

Although MC plays an important role in the analysis, wherever possible, the actual data are used to evaluate quantities needed to derive physical results from the yield of detected $D_s \to \mu\nu$ candidate decays. In the cases where this is not possible and one must rely on the Monte Carlo (i.e., acceptance for neutrino reconstruction), cross-checks are performed using control samples selected from the CLEO data which provide validations of the MC and/or a means of evaluating systematic uncertainties associated with reliance on the MC.

Tuning the Production Spectrum for MC Generation

Initial disagreements on the neutrino reconstruction efficiency prompted checks on the Monte Carlo modeling of D^{*0} and D_s^* production spectra. As a result, we generated our signal and special purpose MC samples with tuned values for Lund symmetric

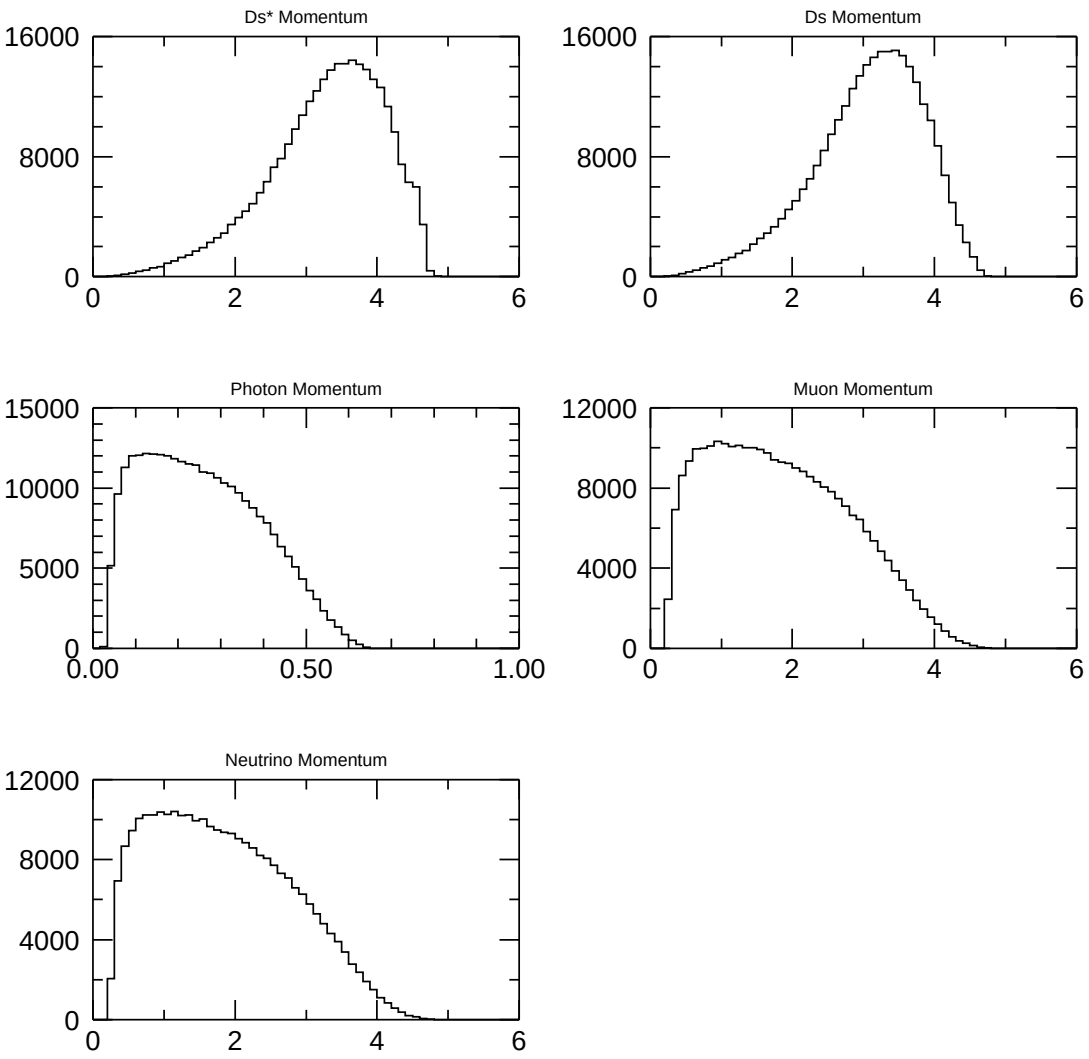

Figure 4.1: The distribution of momenta (in GeV/c) for CLEOII signal MC at the generator-level.

fragmentation function in the JETSET Monte Carlo simulation program. For the D^{*0} samples, we used parameters derived by studies of D^{*0} production in CLEO [49]: `LUNDAA` $= 0.18$, `LUNDBB` $= 0.40$, and `MSPIN(3)` $= 0.63$, where `LUNDAA` and `LUNDBB` are two parameters offered in `JETSET` for quark and gluon hadronization while `MSPIN(3)` is the probability that a meson be generated as a vector meson. For the D_s^* samples, we used `LUNDAA` $= 0.2$, `LUNDBB` $= 0.9$, and `MSPIN(3)` $= 0.63$. These `JETSET` parameters at the generator-level had been tuned to match MC to data for the D_s^* momentum spectrum using the $D_s^{*+} \to \gamma D_s^+$, $D_s^+ \to \phi\pi^+$ sample. In order to obtain an optimized set of parameters, we generated MC samples with various LUND parameters, and fit each of the D_s^* momentum (reconstructed $P_{\gamma\phi\pi}$) for $P_{\gamma\phi\pi} > 2.4$ GeV to that from data. We systematically varied one of the three parameters (`LUNDAA`, `LUNDBB`, and `MSPIN(3)`) and iterated until we found a set of LUND parameters that minimize the chi-square when fitting to data. Figure 4.2 shows the spectra before and after tuning. After all analysis cuts for the $D_s^{*+} \to \gamma D_s^+$, $D_s^+ \to \phi\pi^+$ mode, Figure 4.3 compares the reconstructed D_s and D_s^* momenta for signal MC, continuum MC and data. The generic continuum MC sample was not generated with the correct production parameters, resulting in a very different spectrum; Meanwhile, as a result of the tuning, we were able to obtain the momentum spectra from $D_s^{*+} \to \gamma D_s^+$, $D_s^+ \to \phi\pi^+$ MC samples that agree with the data. We studied the residual effect of MC and data production spectra by reweighting the MC samples, as described in Section 4.4.2.

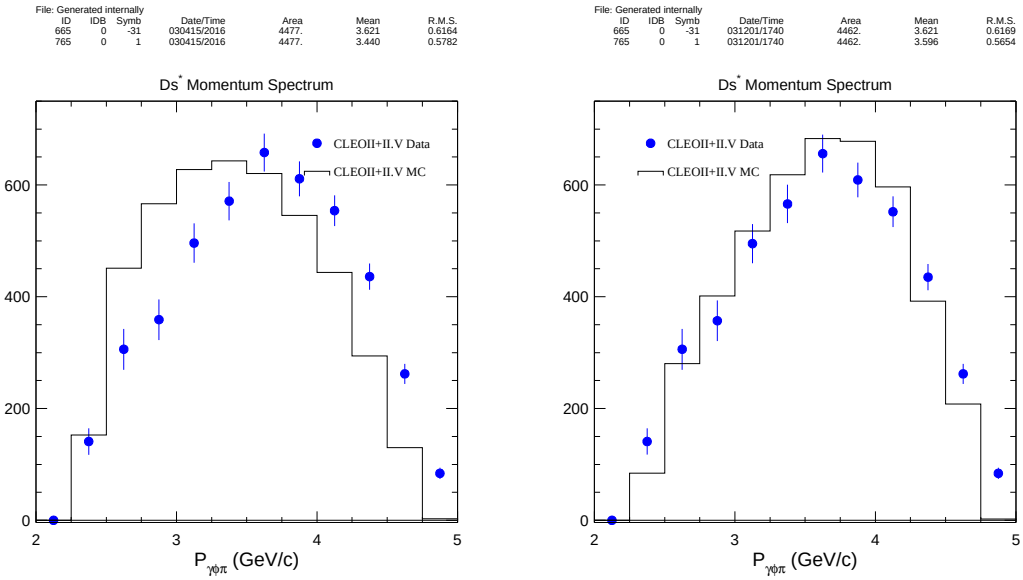

Figure 4.2: The fully reconstructed D_s^* momentum spectrum (with ΔM sideband subtracted) for MC compared to data before (left) and after (right) tuning the LUND parameters. Note that we have relaxed the selection criteria here in order to display the whole spectrum.

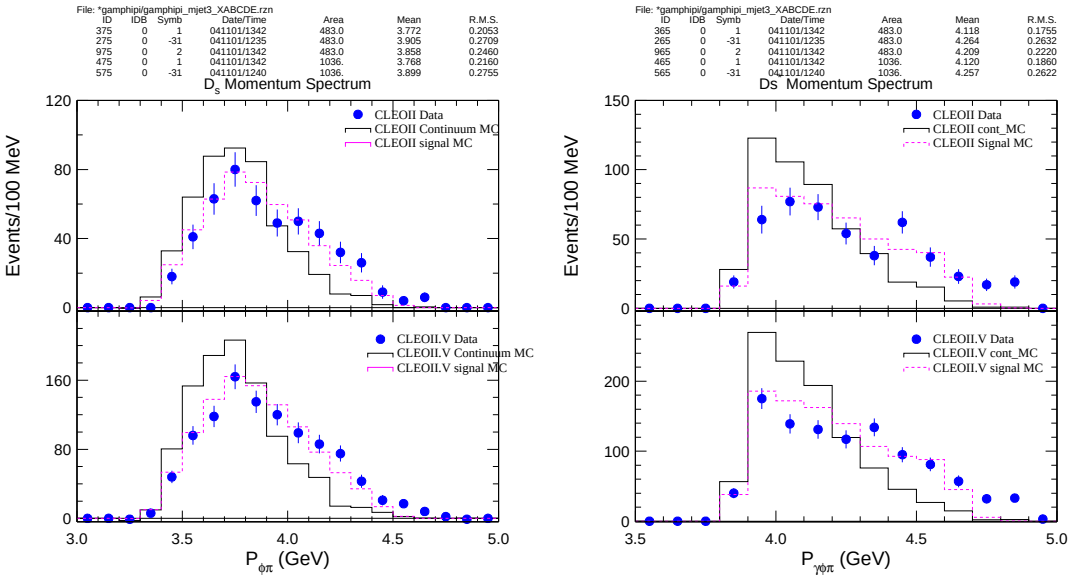

Figure 4.3: The fully reconstructed, background subtracted D_s and D_s^* momentum spectra for MC compared to data, after all analysis cuts mentioned in Section 4.3. Note that the continuum MC was not tuned to model the charmed quark fragmentation accurately. The area of the continuum MC distribution has been normalized to the yield obtained from the data.

4.2.3 Event Selection Criteria

The event selection criteria followed the approach taken by the previous CLEO analysis, but with additional tuning and optimization. We select identified hadronic events that contain a lepton and a photon candidate. We define a "good" reconstructed track as one that satisfies the same track quality cuts as those in Chapter 3 Section 3.2.1. We require there are at least 5 charged good tracks satisfying the quality cuts described above or at least 3 charged good tracks and 6 neutral energy clusters to reject events with low multiplicity quantum electrodynamics (QED) background events. To remove backgrounds from two-photon physics, events with missing transverse momentum $P_t < 0.3$ GeV/c are rejected. This requirement reduced the signal efficiency by about 9.7%. The requirement of the second Fox_Wolfram moment [50] being smaller than 0.8 is imposed to suppress $\tau^+\tau^-$ pair and other QED events with high jettiness.

We identify the lepton candidate by first requiring a good track with $|cos\theta| \leq 0.85$, and then apply lepton identification to reject hadron tracks. For muon identification, we require the track to have penetrated at least seven interaction lengths of absorber material, with all chambers at shallower depths also having hits spatially correlated with the track. To identify electrons, we require the track to satisfy a requirement on the ratio of likelihoods for consistency with electrons versus other paricles. This likelihood ratio (called `R2ELEC`) is determined from the measurements of energy loss in the DR and E/p where E is energy measured in the calorimeter and p is the track momentum obtained from the curvature measurement. We require this likelihood to be greater than 3. We require the momentum of the lepton to be at least 2.4 GeV/c to

suppress backgrounds from B meson decays. We also require there to be one and only one identified lepton in an event to reduce the possibility of multiple neutrinos in the event. The lepton identification efficiencies are $(85 \pm 1)\%$ and $(89 \pm 2)\%$, respectively for muon and electron [44].

The low-momentum photon coming from the decay of the D_s^* must have a photon-like energy deposition shape and have energy deposition in the calorimeter above 180 MeV in the good barrel region $|cos(\theta_\gamma)| < 0.71$. In addition, we need to make sure the showers are not matched to any tracks and are not split-offs from hadronic interaction in the calorimeter. To reduce random photon background, we combine our transition photon candidate with a random photon, and see if they form a π^0. Using this information, we can veto π^0 by rejecting photons that have invariant masses within two standard deviation of the π^0 mass. So as to avoid rejecting transition photons that accidentally combine with a random photon to form a π^0 candidate, we only reject photons for which $cos(\theta_{cm}) \leq 0.63$ where $cos(\theta_{cm})$ is the decay angle of the π^0 candidate (that is the angle between the direction of emission of the transition photon candidate in the π^0 candidate's rest frame, and the π^0 propagation direction in the laboratory frame).

The following selection requirements are results of cut optimization discussed in section 4.2.5. In rest frame of D_s^*, we require cosine of angle $Cos(\theta_{\gamma D_s^*})$ between the photon and the D_s^* direction in the lab be larger than -0.6. To make sure the photon and muon candiates are in the same decay hemisphere and as so to reduce random photon and muon combinations, we require $Cos(\theta_{\gamma\mu}) \geq 0.45$ for the angle between the muon and the photon. To suppress combinatoric backgrounds, the D_s^* candidates are

required to have a scaled momentum $P_{\gamma\mu P_{miss}}/E_{Beam} > 0.735$ GeV/c after the D_s mass constraint. We require the missing mass squared $M^2_{miss} \equiv (E^2_{miss} - p^2_{miss}) < 1$ GeV^2. If the neutrino reconstruction is perfect, and all particles other than the neutrino from $D_s \to \mu\nu$ are detected, then $M^2_{miss} = 0$. A diagonal cut on charge*$Cos(\theta_{P_{lepton}}) \leq$ 1.343+1.143*charge*$Cos(\theta_{P_{miss}})$ is aimed at rejecting radiative bhabha events. The quantities $P_{\gamma\mu P_{miss}}$, M_{miss} and $Cos(\theta_{P_{miss}})$ all depend on neutrino reconstruction, which is described in Section 4.2.4.

4.2.4 Neutrino Reconstruction

We begin the neutrino reconstruction by selecting good tracks and showers for use in the calculation of missing momentum and energy. Several methods have been developed at CLEO to effectively reconstruct the neutrino in an event. One way is to use the entire event [44], and to calcuate the missing momentum and energy by

$$\begin{aligned} \overrightarrow{p}_{miss} &= -\sum_i \overrightarrow{p}_i, \\ E_{miss} &= 2E_{beam} - \sum_i E_i, \end{aligned} \tag{4.2}$$

where $\overrightarrow{p}_i$ and E_i are the 3-momentum and energy respectively of the i^{th} track or shower, and E_{beam} is the beam energy. We then use the $\overrightarrow{p}_{miss}$ and E_{miss} as the neutrino momentum and energy, respectively. Another way to compute the missing momentum and energy is (hereafter referred to as "half-event" method) by using the

hemisphere of the event that contains the signal D_s^+ candidate with

$$\begin{aligned} \overrightarrow{p}_{miss} &= \overrightarrow{p}_{thrust} - \sum_i \overrightarrow{p}_i, \\ E_{miss} &= E_{beam} - \sum_i E_i. \end{aligned} \tag{4.3}$$

Here, the direction of $\overrightarrow{p}_{thrust}$ is given by the thrust axis of the event, and its magnitude $|\overrightarrow{p}_{thrust}|$ is estimated by

$$p_{thrust}^2 = E_{beam}^2 - M_{jet}^2, \tag{4.4}$$

where M_{jet} is the average mass of a charm quark jet. Therefore, the neutrino reconstructed from the missing momentum relies on the determination of the thrust axis orientation and the use of the average jet mass. To improve the resolution on the neutrino kinematics we finally apply a kinematic constraint on the system so that $M(\mu\nu) = M(D_s)$. For this analysis, the half-event method is used (rather than the entire-event method) because of the larger acceptance. Studies of both methods had been documented in an analysis [51] of $D \to \mu\nu$.

We use an average jet mass for each event calculated by $M_{jet} = \sqrt{\Sigma {E_i}^2 - \Sigma \vec{P}_i^2}$ where i indicates the i^{th} detected track or shower. Not all particles are detected in an event, and this is especially true for the case of $D_s \to \mu\nu$. Therefore, the jet mass calculated will not be accurate if the event contains missing particles. We have studied the average jet mass in comparing data and MC to demonstrate that the jet mass is simulated in the MC sample. First as a cross check, we find a sample of events with a $D^0 \to K\pi$ that comes from a D^{*0}, and calculate the thrust for each of these events. We choose this sample because all particles from the decay can be

detected. Second, we calculate the invariant mass of the tracks and isolated showers that are in the D^0 hemisphere with respect to the thrust axis. Finally, we use the MC tagged events and background subtracted events to verify that the reconstructed events have more or less the same average jet mass for CLEOII MC and data in the case of $D^0 \to K^-\pi^+$ (see the second plot in Figure 4.4). For generator-level MC events, we calculate M_{jet} by summing over the momenta and energies for the top level particles from the virtual photon only. The first plot in Figure 4.4 shows the average m_{jet} as a function of the μ momentum (crosses), in comparison to that from $D_s^+ \to \phi\pi^+$ (squares, diamonds, and triangles). The M_{jet} from reconstructed events tends to be lower than that from true M_{jet} obtained from generator-level quantities for $D_s^+ \to \phi\pi^+$. If we fit the data points from CLEOII+II.V (and exclude the first and last points in fitting) in Figure 4.4 to a linear function, we get $M_{jet} = 3.58 - 0.25P_\mu$ using generator-level quantities. Based on the cross-check study done above, we can trust the MC in simulating the jet mass, and use the fitted fuction of M_{jet} obtained above for use in data. A study of how the jet mass affects the neutrino reconstruction is shown in Section 4.4.2.

Finally, we use the D_s mass constraint to correct the reconstructed neutrino momentum. Figure 4.5 shows the relationship between the muon and neutrino momentum vectors and the constraint surface imposed by the D_s invariant mass. The error associated with the lepton track is relatively small compared to the reconstructed neutrino, so we adjust the neutrino vector relative to the muon to satisfy the D_s invariant mass. The corrected neutrino momentum is the vector sum of the $\overrightarrow{p}_\nu^{meas}$ obtained from missing momentum and the minimum displacement vector $\overrightarrow{d}$ mea-

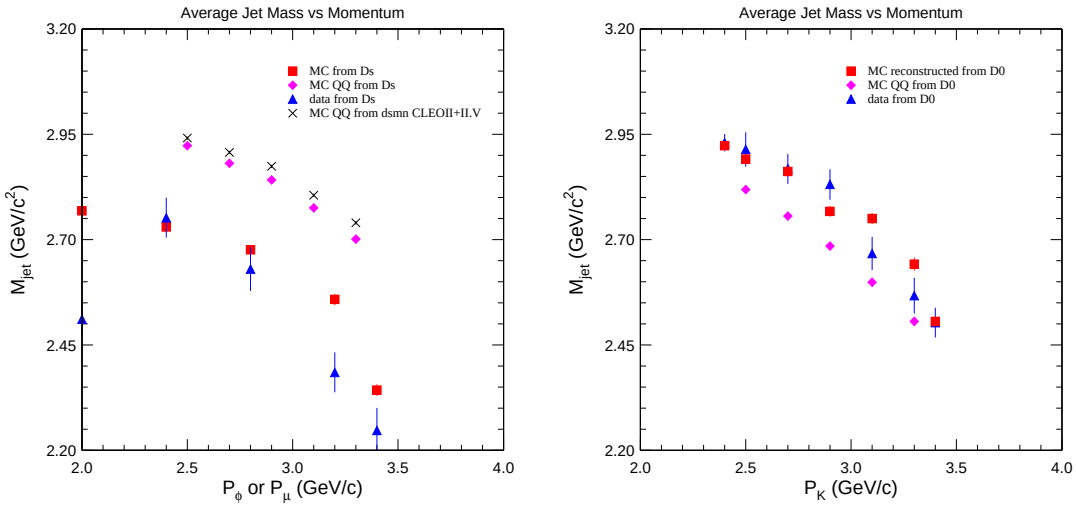

Figure 4.4: The plot on the left shows the m_{jet} as a function of P_ϕ or P_μ (at generator-level only for $D_s^+ \to \mu\nu$) using CLEOII signal MC and CLEOII data for $D_s^{*+} \to \gamma D_s^+$, $D_s^+ \to \phi\pi^+$. Also shown is the comparison to m_{jet} as a function of P_K in the case of $D^{*0} \to \gamma D^0$, $D^0 \to K^-\pi^+$.

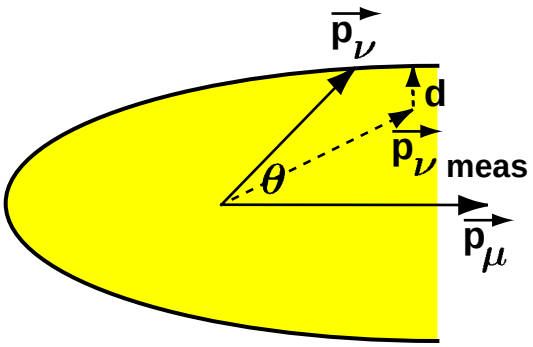

Figure 4.5: The D_s mass constraint ellipsoid. (Diagram taken from Ref. [44])

sured from $\overrightarrow{p}_{\nu}^{meas}$ to the surface of the ellipsoid. Figure 4.6 shows that the resolution for the signal shape is indeed better after applying the D_s mass constraint.

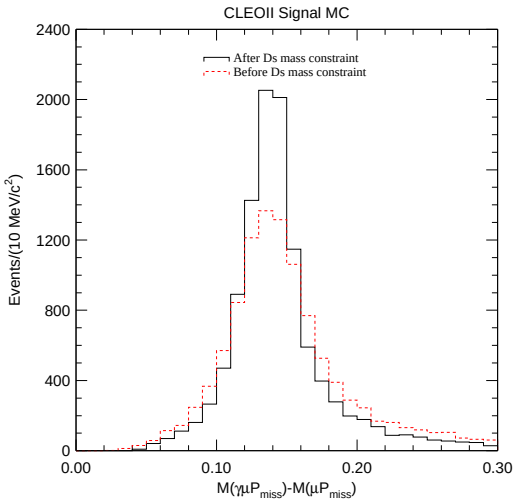

Figure 4.6: A comparison of the mass difference before and after D_s mass constraint.

When reconstructing the missing momentum, we need to eliminate extra tracks and showers produced by secondary physics processes, such as pion decay and hadronic interactions in the calorimeter. We use `Splitf` [52], a software package developed by CLEO to identify clusters of energy deposition in the calorimeter that are likely to be debris from a hadronic interaction. As mentioned earlier, events with more than one lepton are rejected due to the presence of multiple neutrinos that will result in errors in the calculation of missing momentum and energy.

4.2.5 Cut Optimization for Background Suppression

Based on the previous CLEO measurement, we expect the sample of selected $D_s \to \mu\nu$ candidates to be dominated by background processes. Consequently, a simple figure of merit that characterizes the expected statistical significance of the signal event yield in our data sample is S^2/B where S is the number of expected signal events (determined from signal MC samples) and B is the expected number of background events (determined from continuum MC). Although we do not know the number of expected signal events very precisely, we can compare the relative merit of different selection criteria by comparing the corresponding values of S^2/B.

By maximizing S^2/B to optimize signal and suppress background, we have found the optimal cuts $Cos(\theta_{\gamma D_s^*}) > -0.6$ for the angle between the photon and the D_s^* direction in the lab, and $Cos(\theta_{\gamma\mu}) \geq 0.45$ for the angle between the muon and the photon. We also found that the reconstructed D_s^* momentum is optimized at $P_{\gamma\mu P_{miss}} \geq 3.9$ GeV/c. However, there is a significant difference in the fraction of the number of reconstructed decays of the different types from the subsets of data and signal MC samples corresponding to different beam energy conditions, as shown in Table 4.3. Because the D_s^* momentum spectrum depends on the beam energy, we decided to cut on the scaled momentum $P_{\gamma\mu P_{miss}}/E_{Beam} > 0.735$. The 2-D scatter plots at the left of Figure 4.7 are P_{miss} vs. $P_{\gamma\mu P_{miss}}$ for the background and signal events in CLEOII continuum MC. We explored cuts in P_{miss} vs. $P_{\gamma\mu P_{miss}}$, but we did not find any benefits in doing so. After a cut on $P_{\gamma\mu P_{miss}}/E_{Beam} > 0.735$, the bottom right plot shows that there is an advantage in cutting on M^2_{miss} as it helps us optimize signal, and the optimized cut is determined to be $M^2_{miss} < 1$ GeV^2.

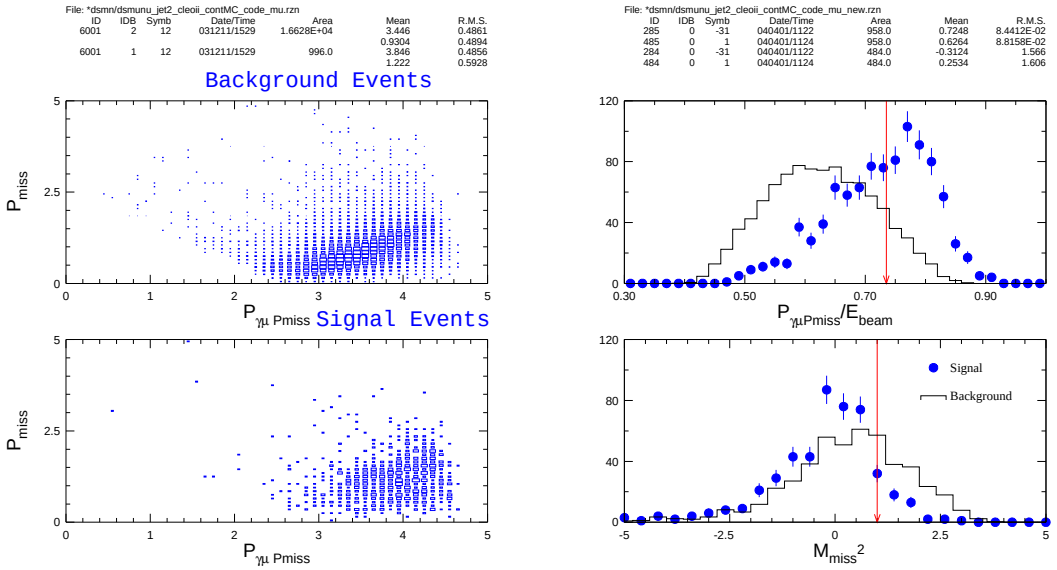

Figure 4.7: The distribution of the background suppression variables for tagged signal and background events in CLEOII continuum MC. We tag (for signal events) or anti-tag (for background) the muon and photon. The plot for M_{miss} is after applying the cut on $P_{\gamma\mu P_{miss}}/E_{Beam}$. The verticle red lines indicate where the cut values $P_{\gamma\mu P_{miss}}/E_{Beam} > 0.735$ and $M^2_{miss} < 1$ GeV^2 are.

Table 4.3: The ratio for the number of reconstructed decays of the different types from the subsets of data and signal MC samples corresponding to different beam energy conditions.

Sample		CLEOII	CLEOII.V
$D^{*0} \to \gamma D^0, D^0 \to K\pi$	data	1.94 ± 0.10	2.57 ± 0.11
	MC	2.14 ± 0.04	2.29 ± 0.04
$D^{*0} \to \pi^0 D^0, D^0 \to K\pi$	data	1.89 ± 0.09	2.38 ± 0.08
	MC	2.19 ± 0.05	2.16 ± 0.03
$D_s^* \to \gamma D_s, D_s \to \phi\pi$	data	1.86 ± 0.11	2.11 ± 0.09
	MC	2.00 ± 0.02	2.12 ± 0.02

If we did not apply the diagonal cut, there would still be some more QED background events passing our cut requirements as shown in Figure 4.8 where we look at the charge correlation for the lepton as well as the ΔM distribution in three regions of charge*$Cos(\theta_{lepton})$. QED events would peak closer to +1 for charge*$Cos(\theta_{lepton})$ since there is a charge correlation for the production of QED processes such as $e^+e^- \to e^+e^-$ or $e^+e^- \to \mu^+\mu^-$. In this case, we study the electron mode rather than the muon mode because of three reasons: (1) the background will be more prominent in electrons, (2) we need the electron sample to be background free if we are to use it to estimate the lepton universality background for the $D_s\mu\nu$ candidates, and (3) we do not want to bias the analysis by looking at the muon data before determining cuts. An excess peak at the high value of charge*$Cos(\theta_{P_{lepton}})$ for the electron mode in CLEOII data indicates QED background contaminations; while as there is no QED

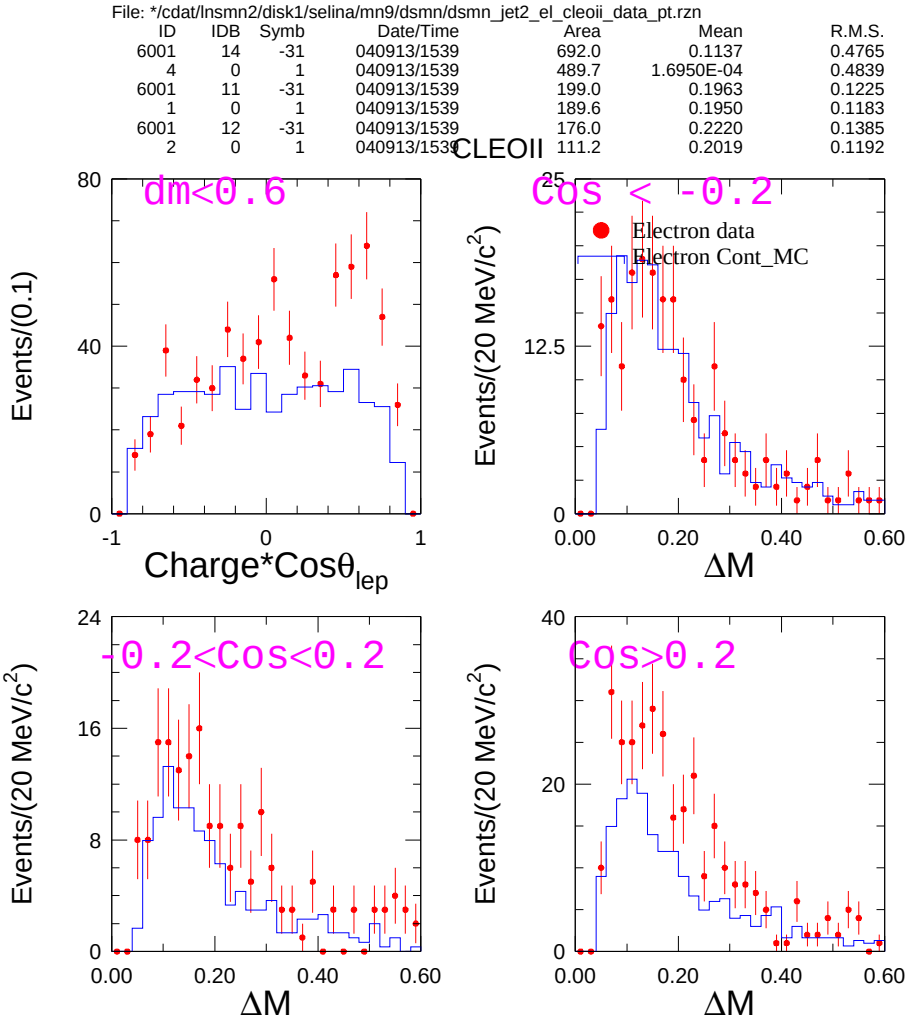

Figure 4.8: A plot of charge*$Cos(\theta_{P_{lepton}})$ on the top left corner for $\Delta M < 0.6$ GeV for the electron mode in CLEOII data and continuum MC. The other three plots are distribution of ΔM in three regions of charge*$Cos(\theta_{P_{lepton}})$.

events in continuum MC and thus the distribution of charge*$Cos(\theta_{P_{lepton}})$ is flat. For charge*$Cos(\theta_{lepton}) > 0.2$, the ΔM for data has an excess over continuum MC which confirms that most of the excess is due to QED background events. We found that a diagonal cut on charge*$Cos(\theta_{P_{lepton}}) \leq 1.343+1.143$*charge*$Cos(\theta_{P_{miss}})$ as drawn in Figure 4.9 would remove most of the QED events and only reduce the signal efficiency by about 2.3-2.7%. Figure 4.10 shows that after the diagonal cut, both the charge*$Cos(\theta_{P_{lepton}})$ and mass difference come to a better agreement in the electron mode for data and MC.

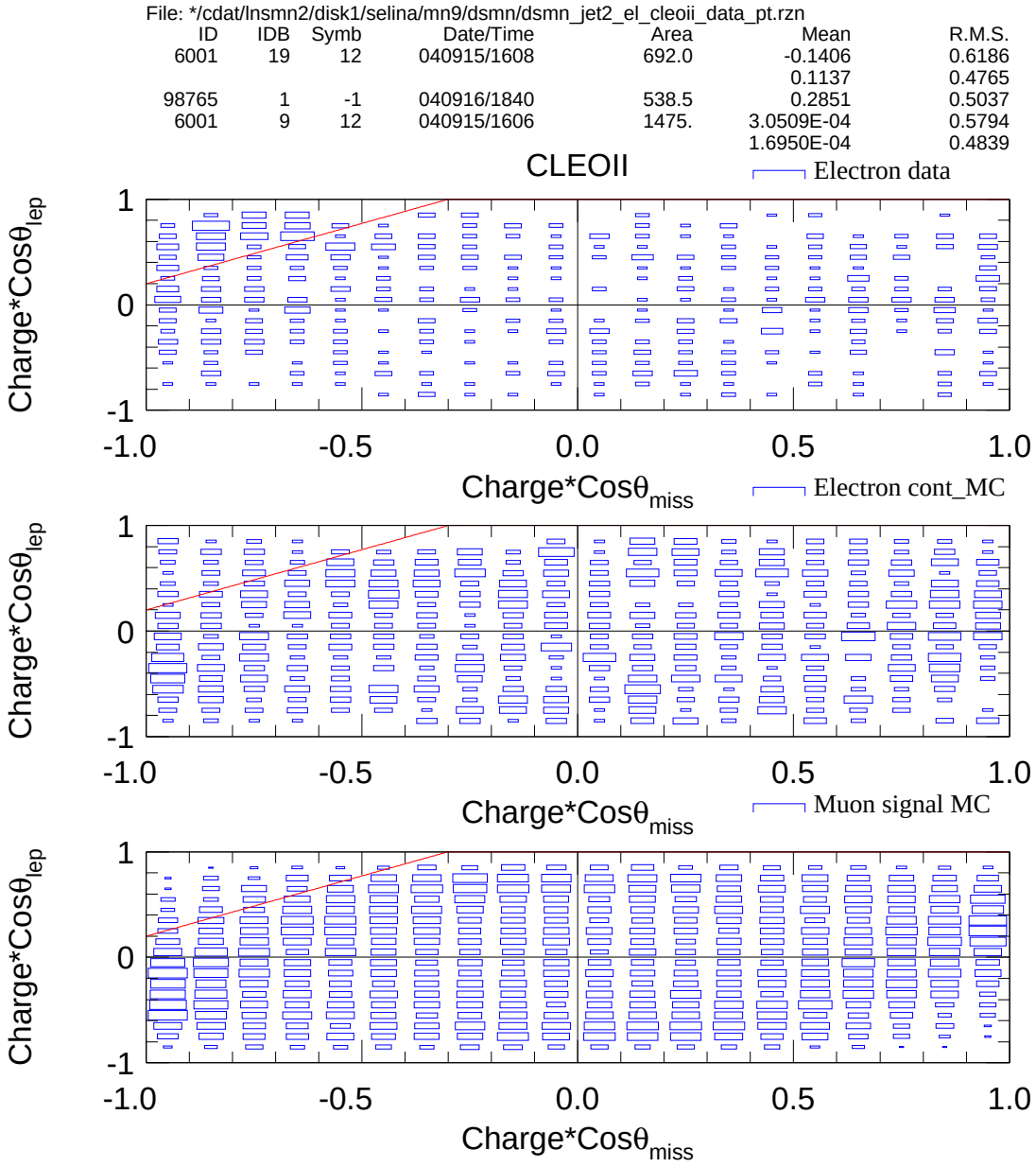

Figure 4.9: The 2-D plots of charge*$Cos(\theta_{P_{lepton}})$ vs. charge*$Cos(\theta_{P_{miss}})$ for the electron mode in CLEOII data (top) and continuum MC (middle), and for the muon mode in signal MC (bottom). The diagonal red lines indicate where the cut values are.

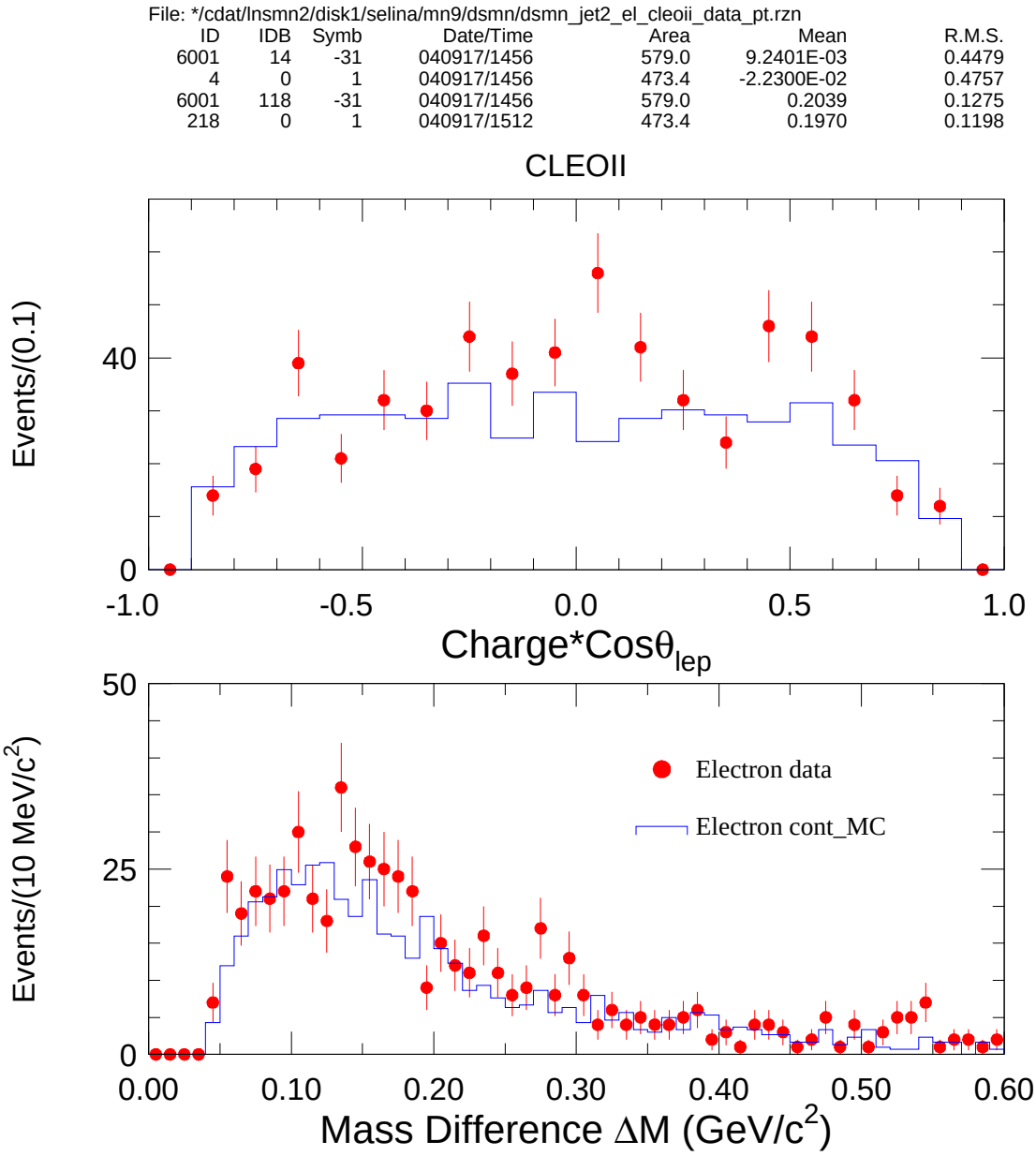

Figure 4.10: The distribution of charge*$Cos(\theta_{P_{lepton}})$ (top) and mass difference (bottom) after the diagonal cut for the electron mode in CLEOII data and continuum MC.

4.2.6 Background Estimation

The main background sources are of the following types: (1). processes with real leptons that obey lepton universality, mainly semileptonic decays; (2). processes with fake leptons (hadrons misidentified as leptons); and (3). processes with real leptons that do not obey lepton universality (such as $D_{(s)} \to \mu\nu$ direct production from the c quark fragmentation). To understand the physics backgrounds and their contributions, we use a sample of simulated generic $e^+e^- \to q\bar{q}$ continuum events, as well as some special-purpose MC simulations of particular background processes.

Real Leptons

Due to helicity suppression, the electronic width is negligible compared to the muonic width in the leptonic D_s^+ decays. Hence, we can repeat the same precedure, but selecting electrons rather than muons, so as to estimate backgrounds assuming lepton universality. By doing so, we obtain a quantitative measurement of the background level associated with real leptons from other decay processes such as semileptonic decays. The background modes that fall in the region between $0 < \Delta M < 0.3$ GeV/c^2 are listed in Table 4.4.

However, we need to take into account of the relative normalization of muon to electron samples in order to estimate the real lepton background level. Electron identification is about 4% more efficient than the muon identification in data, so we need to scale down the electron yield by this amount. The $D \to K_L^0 l\nu$ is the dominant background mode because it has a relative large branching fraction ($\sim$ 3.4%) and also because K_L^0 has a long life time so that it does not decay in our

Table 4.4: The background modes in CLEOII+II.V Continuum MC. Note: we haven't taken into account of lepton fakes and mu/el normalization yet.

	$0 < \Delta M < 0.3$ GeV		
Mode	μ mode	e mode	$\mu - e$ mode
$D_{(s)} \to K^{(*)} l\nu$	1426	1231	195 ± 52
$D \to \pi l\nu$	441	362	79 ± 28
$D_s \to \eta l\nu$	197	148	49 ± 19
$D_s \to \tau\nu, \tau \to l\nu\nu$	356	274	82 ± 25
$D \to \tau\nu, \tau \to l\nu\nu$	17	17	0 ± 6
$D^* \to \pi^0 D, D \to \mu\nu$	198	0	198 ± 14
$D^0 \to K^0 \pi l\nu$	5	0	5 ± 2
$D \to \eta l\nu$	37	41	-4 ± 9
$D^0 \to \rho K$ (K mis-id as lepton)	138	15	123 ± 12
$D \to \pi^0 K^0 l\nu$	9	16	-7 ± 5
$\eta \to \mu^+ \mu^- \gamma$	47	8	39 ± 7
$D_s^* \to \pi^0 D_s, D_s \to \mu\nu$	55	0	55 ± 7
$D_s \to \mu\nu$ direct production	192	0	192 ± 14
$D \to \mu\nu$ direct production	81	0	81 ± 9
$D^* \to \gamma D, D \to \mu\nu$	13	0	13 ± 4
$D^0 \to K^- \pi^+$ (K mis-id as lepton)	246	13	233 ± 16
Others	3540	916	2624 ± 67
Total	6998	3041	3957 ± 100

detector, leaving only a lepton track similar to the case in our $D_s \to \mu\nu$ decays. A study of $D \to K^0_L l\nu$ MC events showed that the detected rate of muonic decays is higher than that for electronic decays by 19%, reflecting the differences between the two decay modes in their phase space factors and in energy loss due to internal and external bremsstrahlung. Furthermore, there is a 2.7% enhanced decay rate for electrons due to inner bremsstrahlung, according to theoretical calculations [53]. From the above sources, we determine that the mass difference for the electron spectrum needs to be scaled by a factor of 1.177 to reflect the differences between the electron and muon lepton universality backgrounds. We refer to this factor as a relative μ/e normalization.

Fake Leptons

For backgrounds that involve lepton fakes, we need to measure the probabilities for misidentifying a hadron of a given type as a muon or electron from control samples selected from data on the basis of kinematics only. This probability depends on the type of hadron (pion, Kaon, or proton). In order to calculate the total number of misidentified hadrons in our $D_s \to \mu\nu$ and $D_s \to e\nu$ candidate samples, we need to know what the particle fractions are.

We use three data samples as listed in Table 4.5 to determine the fake rates where we fit the mass difference $M(\pi^{(+/0)}K^-\pi^+) - M(K^-\pi^+)$ or $M(\gamma K^-\pi^+) - M(K^-\pi^+)$ to get the number of events that pass the basic cuts without lepton identification and that for hadrons identified as leptons. The fit function is a sum of bifurcated Gaussians for signal and a background function $c_1 e^{-c_0(x-x_0)}\sqrt{(x-x_0)}$. When fitting the

mass difference distribution for hadrons identified as leptons, we fixed the parameters obtained from the fit of the ΔM without lepton identifications, but allowed area of the Gaussian and the normalization of the background to float.

Table 4.5: The lepton fake rates (%) for $P > 2.4$ GeV/c in data with different data samples for $|cos(\theta)| < 0.85$ and the track penetrates at least 7 interaction lengths of absorber material. PID was only used on the candidate that is not performing lepton identification on. Since CEID use dE/dx information, it may bias our results if we use dE/dx in identifying the candidates.

CLEOII Data	K/μ	K/e	π/μ	π/e
$D^{*+} \to \pi^+ D^0, D^0 \to K^-\pi^+$	1.27 ± 0.16	0.01 ± 0.02	0.59 ± 0.11	0.09 ± 0.06
$D^{*0} \to \gamma D^0, D^0 \to K^-\pi^+$	1.32 ± 0.41	0.17 ± 0.12	0.88 ± 0.30	0.29 ± 0.18
$D^{*0} \to \pi^0 D^0, D^0 \to K^-\pi^+$	1.41 ± 0.27	-0.01 ± 0.02	0.82 ± 0.19	0.26 ± 0.11
Weighted average	1.31 ± 0.11	0.04 ± 0.02	0.70 ± 0.09	0.17 ± 0.05

CLEOII.V Data	K/μ	K/e	π/μ	π/e
$D^{*+} \to \pi^+ D^0, D^0 \to K^-\pi^+$	1.16 ± 0.11	< 0.02 at 90% C.L.	0.69 ± 0.09	0.06 ± 0.03
$D^{*0} \to \gamma D^0, D^0 \to K^-\pi^+$	1.04 ± 0.25	0.03 ± 0.09	0.72 ± 0.24	0.03 ± 0.10
$D^{*0} \to \pi^0 D^0, D^0 \to K^-\pi^+$	0.98 ± 0.15	< 0.02 at 90% C.L.	0.72 ± 0.13	0.04 ± 0.04
Weighted average	1.09 ± 0.09	0.01 ± 0.02	0.70 ± 0.07	0.05 ± 0.03

To obtain hadron fractions for the calulation of final fake rates, we apply the selection criteria for $D_s \to \mu\nu$ to count all hardon tracks (veto all leptons) that go into the distribution of $0 < \Delta M < 0.3$ GeV/c^2 in Continuum MC. The relative fractions of pions, kaons, and protons in the hadron data are estimated in Table 4.6

for hadron momentum $P > 2.4$ GeV/c.

Table 4.6: The hadron fraction in CLEOII.V continuum MC (running on equivalent luminosity of $12.5 fb^{-1}$). The errors are statistical.

Hadron	CLEOII continuum MC with all analysis cuts	CLEOII.V continuum MC with all analysis cuts
π	$51.6\% \pm 0.3\%$	$51.6\% \pm 0.3\%$
K	$36.6\% \pm 0.3\%$	$36.3\% \pm 0.2\%$
Proton	$11.6\% \pm 0.2\%$	$12.1\% \pm 0.1\%$

In order to study the contribution to the lepton fake rates from kaon and pion decay in flight, we use Monte Carlo events of $D^{*+} \to \pi^+ D^0$, $D^0 \to K^-\pi^+$. We applied muon identification on the tagged events, and then count events in the tail of the mass difference plot that do not appear in the D^0 mass peak that we didn't take into account of when looking for fakes. The decay in flight correction is the ratio of total number of events divided by (total number of events - events in the tail regions). Table 4.7 shows the decay in flight correction determined from this MC sample.

Table 4.7: The decay in flight correction determined using $D^{*+} \to \pi^+ D^0$, $D^0 \to K^-\pi^+$ MC sample.

Sample	*Kaon*	*Pion*
CLEOII	1.023 ± 0.009	1.014 ± 0.010
CLEOII.V	1.081 ± 0.017	1.046 ± 0.017

The total lepton fake rates are sumarized in Table 4.8 where we have used the results of the fake rates for data in Table 4.5, decay in flight correction obtained from MC in Table 4.7, and the hadron fraction estimated from continuumm MC in Table 4.6.

Table 4.8: Total lepton fake rates (%) determined for data. The errors are statistical.

Data	Total Muon fake rate before decay in flight correction	Total Muon fake rate after decay in flight correction	Total Electron fake rate
CLEOII	0.84 ± 0.06	0.86 ± 0.08	0.10 ± 0.03
CLEOII.V	0.76 ± 0.05	0.81 ± 0.05	0.03 ± 0.02

Others

For backgrounds with real lepton but do not obey lepton universality, they cannot be subtracted off from the electron mode. Most of these background modes are due to random photons or π^0. From studies done with continuum MC in Table 4.4, these background modes include: 1). Direct $D_{(s)} \to \mu\nu$ production; 2). $D_s^{*+} \to D_s^+\gamma$, $D_s^+ \to \tau\nu$ and $\tau \to \mu\nu\bar{\nu}$; and 3). π^0 background: $D_{(s)}^* \to D_{(s)}\pi^0$, $D_{(s)} \to \mu\nu$. We take into account of these backgrounds by studying their shape with the special purpose MC samples and using three background functions to describe them when performing fits to get the final yield. We assumed that the shape of direct production of $D_s \to \mu\nu$ is the same as that of $D \to \mu\nu$, and that $D_s^* \to D_s\pi^0$, $D_s \to \mu\nu$ has the same shape as $D^* \to D\pi^0$, $D \to \mu\nu$.

An alternative way to remove background from direct production of $D_s \to \mu\nu$

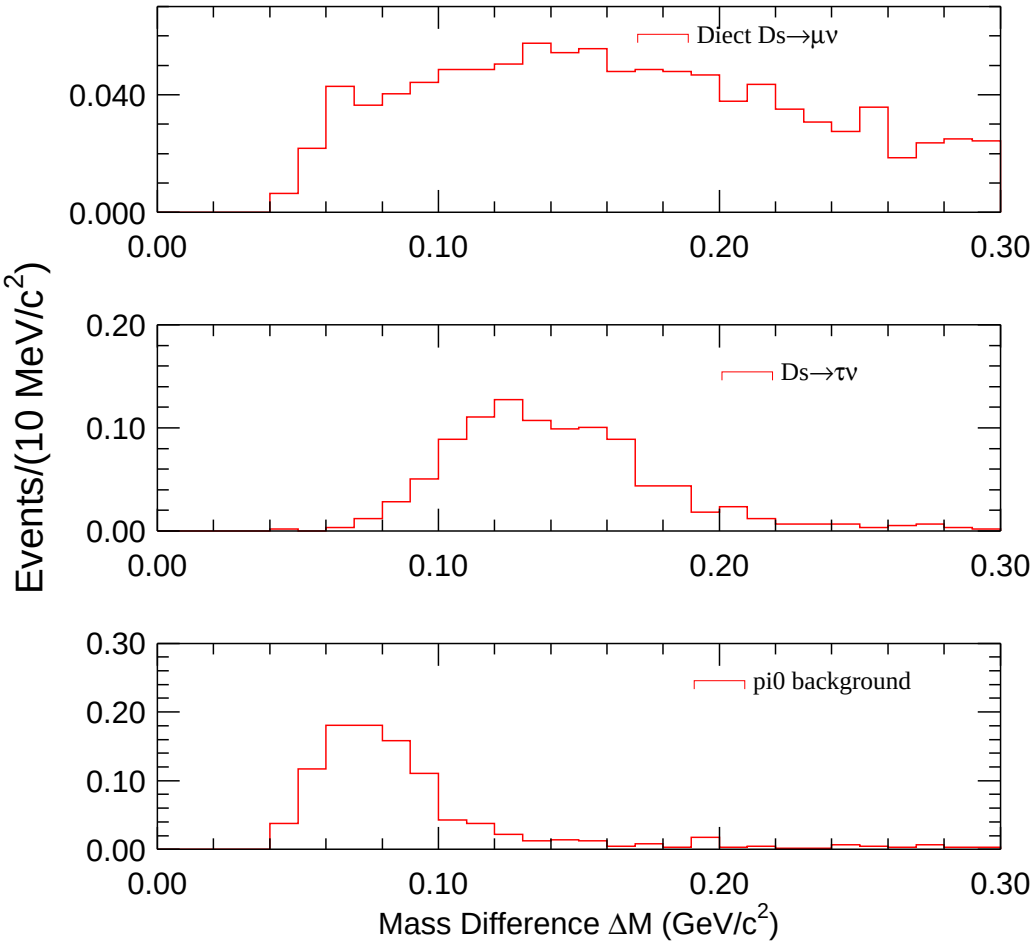

Figure 4.11: The mass difference for the following background modes: 1). Direct $D_s \to \mu\nu$ production; 2). $D_s^{*+} \to D_s^+\gamma$, $D_s^+ \to \tau\nu$ and $\tau \to \mu\nu\bar{\nu}$; and 3). $D_s^* \to D_s\pi^0$, $D_s \to \mu\nu$, where all of them are reconstructed as the signal mode $D_s^* \to \gamma D_s$, $D_s \to \mu\nu$.

where it has been combined with a random photon to mimic our signal events is to make a correction based on the D_s^* and D_s production ratio. To measure this production ratio, we select the D_s candidates by reconstructing the decay chain: $D_s^+ \to \phi\pi^+$, $\phi \to K^+K^-$; whileas the D_s^* candidates are selected from the sample with the above D_s candidates combined with a photon. We also require that the D_s momentum to be above 3.15 GeV/c which is choice based on the momentum spectrum shown in Figure 4.3. The other requirement is the invariant mass M_{KK} to be within 9 MeV/c^2 of the known ϕ mass. For D_s^* reconstruction, we added additional cuts on the photon such as π^0 veto, $P_\gamma \geq 0.18$, $cos\theta_\gamma\phi \geq 0$ so that they are similar to the requirements for the $D_s \to \mu\nu$ analysis. We also require that $M_{KK\pi}$ to be within 24 MeV/c^2 of the known D_s mass. The number of D_s candidates is obtained from a fit to the invariant mass of the $\phi\pi$, and the number of D_s^* is from a fit to the mass difference $\Delta M = M(\gamma\phi\pi^+) - M(\phi\pi^+)$. The production ratio D_s^*/D_s is then calculated by taking the ratio of efficiency-corrected number of D_s^* and number of D_s that is not from a D_s^*. The yield and efficiency for reconstructing D_s and D_s^* as well as the production ratio are shown in Table 4.9.

We vary the D_s momentum cut to see if there is any momentum dependent for the production ratio. Figure 4.12 is a plot of the production rate D_s^*/D_s as a function of D_s momentum cut. Based on study done with $D_s \to \phi\pi$, we take a weighted average for CLEOII and II.V data and determined the production rate D_s^*/D_s to be 1.00 ± 0.05. Therefore, we conclude that there is no need to make a correction for the production ratio.

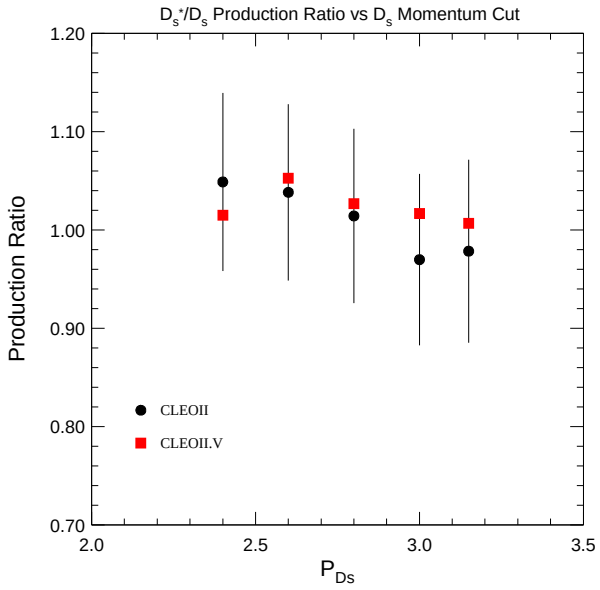

Figure 4.12: Production rate D_s^*/D_s as a function of D_s momentum cut for CLEOII and II.V data.

Table 4.9: A table shows the number of reconstructed D_s^* events $N_{D_s^*}$ and D_s events N_{D_s}, as well as their corresponding reconstruction efficiency $\epsilon_{D_s^*}$ and ϵ_{D_s}. The last row in the table shows the production ratio D_s^*/D_s for $P_{D_s} \geq 3.15$ GeV/c for CLEOII and II.V data.

	CLEOII MC	CLEOII.V MC	CLEOII data	CLEOII.V data
$N_{D_s^*}$	$40,334 \pm 229$	$49,115 \pm 255$	805 ± 34	$1,665 \pm 49$
N_{D_s}	$110,116 \pm 389$	$137,528 \pm 386$	$4,443 \pm 100$	$9,288 \pm 132$
$\epsilon_{D_s^*}$	$(8.91 \pm 0.04)\%$	$(9.44 \pm 0.04)\%$		
ϵ_{D_s}	$(24.32 \pm 0.06)\%$	$(26.42 \pm 0.06)\%$		
$\frac{D_s^*}{D_s}$			0.978 ± 0.093	1.007 ± 0.067

4.2.7 Signal Shape and Efficiency

We use a sample of signal Monte Carlo events to study the ΔM signal shape and to evaluate signal detection efficiency for $D_s^{*+} \to \gamma D_s^+$, $D_s^+ \to \mu^+ \nu$. We fit the signal shape to two Gaussians and a Chebyshev polynomial of third order (see Figure 4.13). The signal events are the sum of the two Gaussian areas, and we determined an overall efficiency of $(3.24 \pm 0.03)\%$ for CLEOII and $(3.45 \pm 0.03)\%$ for CLEOII.V signal MC. Note that we used CLEOII.V signal MC's shape to fit for CLEOII signal MC and allowed the areas to float. This provides a cross-check of signal shape as well as demonstration of similarity in detector response in the CLEOII and CLEOII.V configuration.

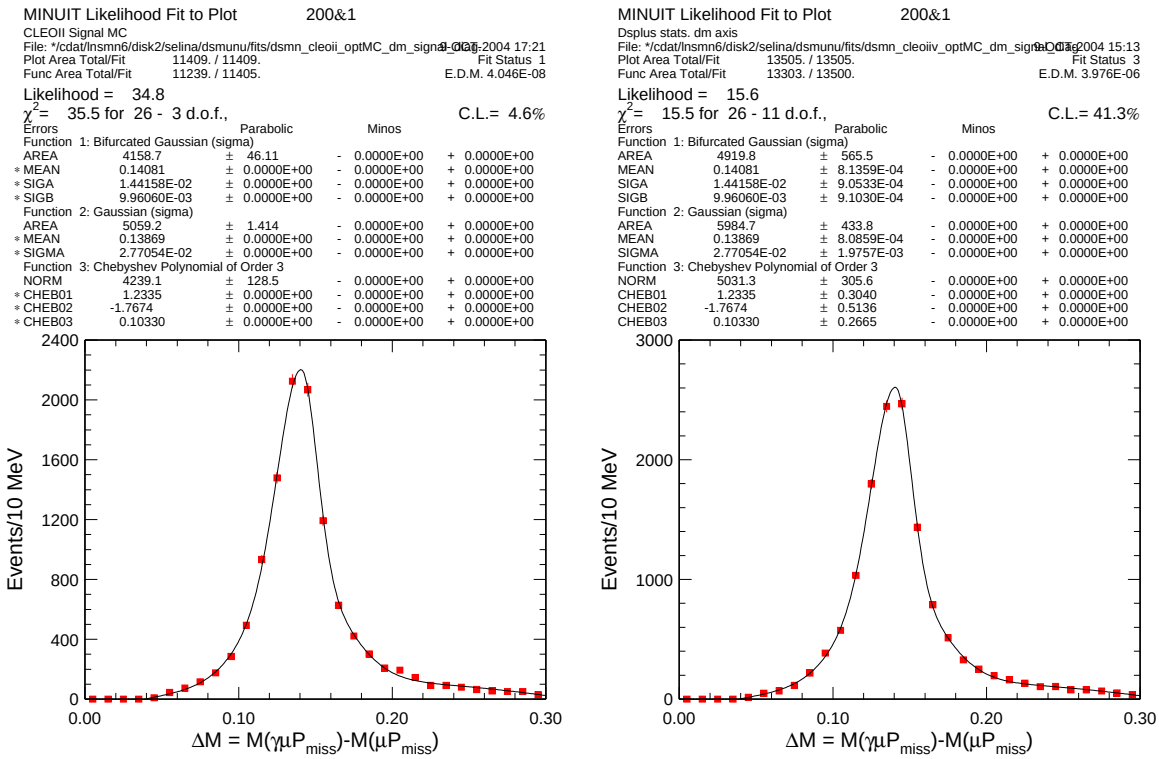

Figure 4.13: The fit to the mass difference after the D_s mass constraint for $D_s \to \mu\nu$ CLEOII and CLEOII.V signal MC.

4.3 Normalization Mode $D_s^+ \to \phi\pi^+$

We use $D_s^* \to \gamma D_s$, $D_s \to \phi\pi$, $\phi \to K^+K^-$ as the normalization mode because of the ease of three-track reconstruction as well as the elimination of some systematic uncertainties associated with the photon detection. We aim to impose requirements for the normalization mode that are as similar to the $D_s \to \mu\nu$ analysis as much as possible so that systematics cancel. The kaon and pion tracks are identified by requiring that the dE/dx information is consistent with the track hypothesis (π/K) within 3 standard deviations. To select the D_s^* candidates, we require $P(D_{\gamma\phi\pi}) \geq 3.15$ GeV/c. The photon candiate needs to have the same requirements as mentioned in section 4.2.3 and we also require that the γ and ϕ be in the same hemisphere. We require the invariant mass of M_{KK} to be within 9 MeV/c^2 of the known ϕ mass and $M_{\phi\pi}$ to be within 24 MeV/c^2 of the known D_s mass. We choose the D_s sideband regions to be $1.91 < M(\phi\pi) < 1.934$ GeV/c^2 and $1.998 < M(\phi\pi) < 2.022$ GeV/c^2 for sideband subtraction (see Figure 4.14).

We obtained the signal shape and efficiency from MC samples of $D_s^* \to \gamma D_s$, $D_s \to \phi\pi$, $\phi \to K^+K^-$. We fit for the signal with a sum of two bifurcated Gaussians and a background function of Chebyshev polynomial of second order. We then use the signal function from signal MC to fit the data where we allow the areas of the fit functions as well as the parameters for the background function to float. We found that the mean of the mass difference in data is higher than that in signal MC, so we float the mean of the Gaussian function as well. Figure 4.15 shows the fits to the mass difference $M(\gamma D_s) - M(D_s)$ after sideband subtraction for CLEOII and II.V

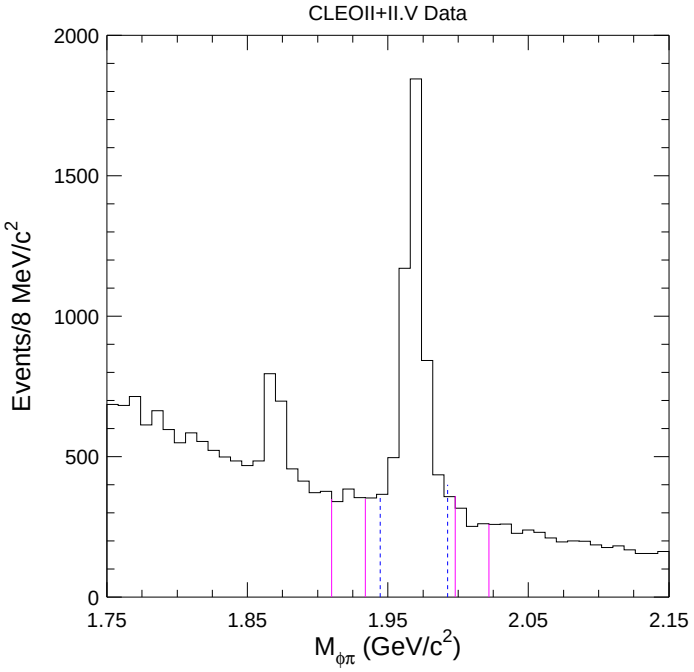

Figure 4.14: The distribution of $M(\phi\pi)$ before performing $M(D_s)$ sideband subtraction for $D_s^* \to \gamma D_s$, $D_s \to \phi\pi$, $\phi \to K^+K^-$ in CLEOII+II.V data where the sideband (between the solid verticle lines) and signal regions (between the dashed verticle lines) are marked.

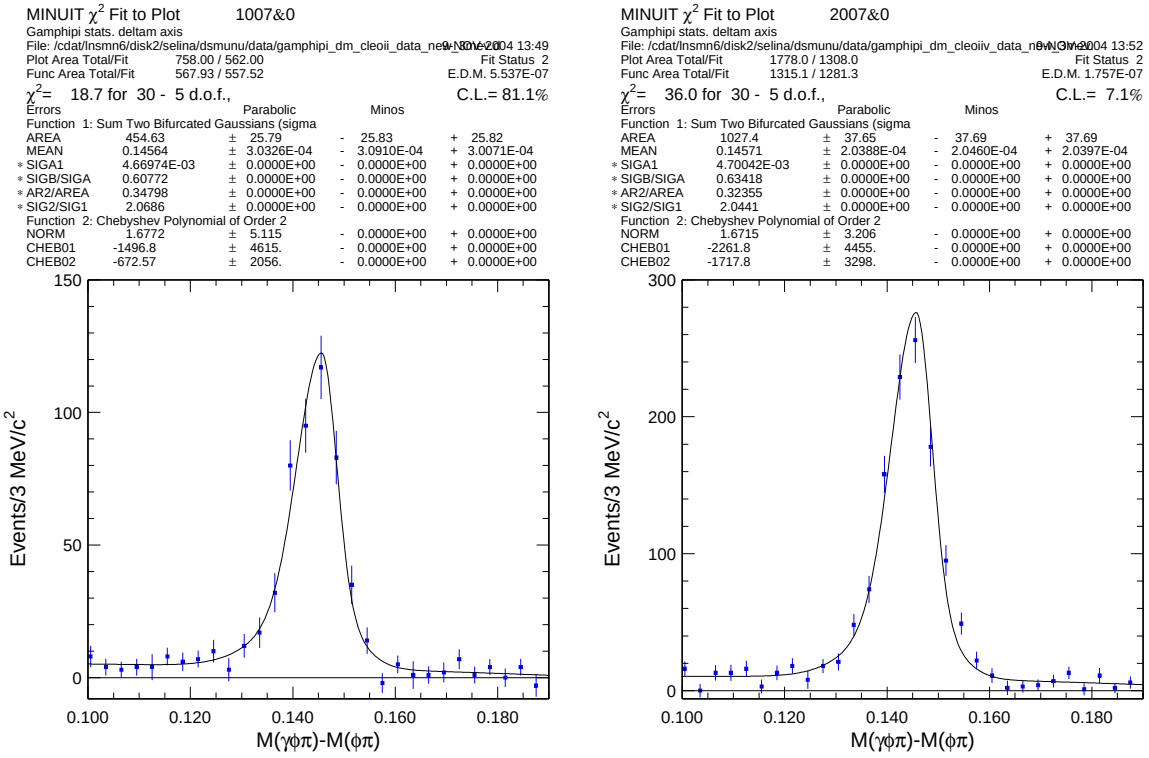

Figure 4.15: Fits to the mass difference for $D_s^* \to \gamma D_s$, $D_s \to \phi\pi$, $\phi \to K^+K^-$ after $M(D_s)$ sideband subtraction in CLEOII (left) and II.V (right) data.

data.

Table 4.10 summarizes for the overall reconstruction efficiency and signal yield. Note that the efficiency for CLEOII+II.V is the luminosity weighted average of that for CLEOII and CLEOII.V.

Table 4.10: Summary for efficiency and signal yield for the normalization mode $D_s^* \to \gamma D_s$, $D_s \to \phi\pi$, $\phi \to K^+K^-$.

	CLEOII	CLEOII.V	CLEOII+II.V
Overall efficiency	$(4.97 \pm 0.03)\%$	$(5.29 \pm 0.03)\%$	$(5.18 \pm 0.02)\%$
Number of reconstructed D_s^*	455 ± 26	1027 ± 38	1483 ± 46
Efficiency corrected yield	9155 ± 526	19414 ± 727	28629 ± 895

4.4 Results

We obtain the number of signal events for $D_s^{*+} \to \gamma D_s^+$, $D_s^+ \to \mu^+\nu$ from a fit to the mass difference $\Delta M = M(\gamma\mu\nu) - M(\mu\nu)$. We then extract the $D_s^+ \to \mu^+\nu$ decay width by normalizing to the efficiency corrected number of fully reconstructed $D_s^{*+} \to \gamma D_s^+$, $D_s^+ \to \phi\pi^+$ events.

4.4.1 Fit Results

We perform fits to the mass difference ΔM in the muon data by combining a signal shape obtained from signal MC and two background histogram functions. The first background function is determined from π^0 MC background shape (see Figure 4.11

or the shaped area in Figure 4.16). The second background function is obtained from a fit to the electron data as well as the lepton fakes. We use a scale factor of 1.177 for the μ/e normalization to scale up the electron data, and then combine the histogram with the ΔM distribution for the muon over electron excess fakes. Figure 4.16 shows the fit to the mass difference where the areas of all signal and background functions are allowed to float. This fit method gives us a total of 330 ± 61 signal events for CLEOII+II.V data.

Table 4.11 summarize the fit results for the CLEOII and CLEOII.V data sets separately as well as combined. Note that the efficiency for CLEOII+II.V is the luminosity weighted average of that for CLEOII and CLEOII.V.

Table 4.11: Summary for the overall reconstruction efficiency and signal yield for the normalization mode $D_s^* \to \gamma D_s$, $D_s \to \mu\nu$.

	CLEOII	CLEOII.V	CLEOII+II.V
Overall efficiency	$(3.24 \pm 0.03)\%$	$(3.45 \pm 0.03)\%$	$(3.38 \pm 0.02)\%$
Number of reconstructed D_s^*	99 ± 35	241 ± 51	330 ± 61
Efficiency corrected yield	3056 ± 1081	6986 ± 1480	9763 ± 1806

Using the results from $D_s \to \phi\pi$ in Table 4.10 and $D_s \to \mu\nu$ in Table 4.11 along with a branching ration of $(49.1 \pm 0.6)\%$ [1] for $\phi \to K^+K^-$, we obtained the ratio of the decay width for the two datasets in Table 4.12. The CLEOII and II.V luminosity weighted average is 0.172. Using the combined CLEOII and II.V combined datasets,

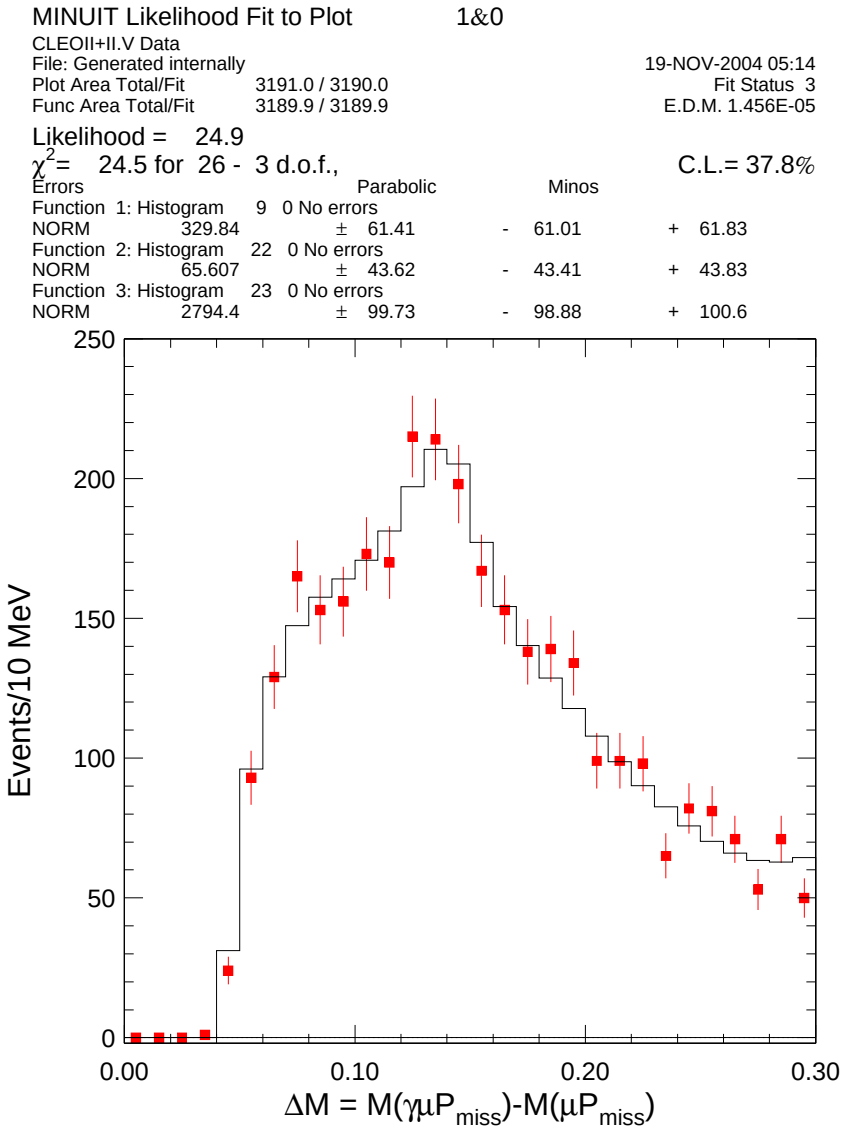

Figure 4.16: A fit to the mass difference for $D_s \to \mu\nu$ CLEOII+II.V data (data points) is shown in the black histogram. Function 1: signal; Function 2: $D_s^* \to D_s\pi^0$, $D_s \to \mu\nu$; Function 3: electron + excess muon over electron fakes.

Table 4.12: The ratio of the decay width $\Gamma(D_s \to \mu\nu)/\Gamma(D_s \to \phi\pi)$.

	CLEOII	CLEOII.V	CLEOII+II.V
Ratio	0.164 ± 0.059	0.177 ± 0.038	0.167 ± 0.031

the ratio of the decay width is measured to be

$$\frac{\Gamma(D_s \to \mu\nu)}{\Gamma(D_s \to \phi\pi)} = 0.167 \pm 0.031[stat.] \pm 0.011[syst.] \tag{4.5}$$

The systematic error is discussed in section 4.4.2.

4.4.2 Systematic Uncertainties

The systematic uncertainties on the width ratio of $\Gamma(D_s \to \mu\nu)/\Gamma(D_s \to \phi\pi)$ include contributions from the uncertainty in the measurement of detection efficiency, fitting, and $\phi\pi^+$ normalization. Table 4.13 shows the estimated systematic errors on the decay

Table 4.13: Estimated systematic errors on the decay width ratio.

Source of Error	Value	Size of Error (%)
Detection efficiency	$(3.38 \pm 0.11)\%$	3.3%
Selection criteria	–	2.6%
Fit Procedure	–	4.3%
$\phi\pi$ normalization	$58308 \pm 1957[stat.] \pm 1747[syst.]$	3.0%
Total systematic error		6.7%

width ratio. We now discuss the detailed estimate of systematics in the following

subsections. We also include discussion of other systematics studies done for this analysis such as lepton fake rates and μ/e normalization to which the result is immune since we allow the background normalization float.

Efficiencies

The uncertainty for detection efficiency mainly comes from the neutrio reconstruction efficiency. We performed a cross check study of the neutrino reconstruction using three independent samples: $D^{*0} \to \gamma D^0$, $D^0 \to K^-\pi^+$; $D^{*0} \to \pi^0 D^0$, $D^0 \to K^-\pi^+$; and $D_s^{*+} \to \gamma D_s^+$, $D_s^+ \to \phi\pi^+$. We first fully reconstruct the decay chains, and then delete the π^+ track and reconstruct it as a missing particle in all three cases. The event selection and basic cuts used for $D^0 \to K^-\pi^+$ are similar to that for $D_s \to \mu\nu$, except that we require the invariant mass $M_{K\pi}$ to be within 30 MeV/c^2 of the known D^0 mass. Similarly for the $D_s \to \phi\pi$ case, the only different requirements are the invariant mass M_{KK} to be within 9 MeV/c^2 of the known ϕ mass and $M_{KK\pi}$ to be within 24 MeV/c^2 of the known D_s mass. A comparison of data and MC for the cross-check of neutrino reconstruction is summarized in Table 4.14.

We also studied the effect of varying M_{jet} on the neutrino reconstruction efficiency as shown in Table 4.15. Based on what we learn in the case of $D_s^+ \to \phi\pi^+$ and $D^0 \to K^-\pi^+$ cases in Section 4.2.4, we use the jet mass $M_{jet}(P_\mu) = 3.58 - 0.25P_\mu$ which is obtained from generator-level quantities for $D_s \to \mu\nu$.

The reconstructed D_s^* momentum is most sensitive to the production spectrum. Since one of our neutrino reconstuction cuts is $P_{\gamma\mu P_{miss}}/E_{Beam}$, we would like to know how big an effect the spectrum has on the neutrino reconstruction efficiency.

Table 4.14: The neutrino reconstruction efficiency ϵ_ν in MC and data. $M_{jet}(P_K) = 3.80 - 0.388P_K$ is used in the $D^{(*0)}$ cases, and in the case of $D_s \to \phi\pi$ we use $M_{jet} = 2.94$ for $P_\phi \leq 2.94$, and $M_{jet} = 3.61 - 0.27P_\phi$ otherwise.

Data Sample	ϵ_ν MC	ϵ_ν Data	fractional difference
$D^{*0} \to \gamma D^0$, $D^0 \to K^-\pi^+$	$(59.4 \pm 0.3)\%$	$(56.1 \pm 1.1)\%$	$(5.6 \pm 1.9)\%$
$D^{*0} \to \pi^0 D^0$, $D^0 \to K^-\pi^+$	$(57.4 \pm 0.3)\%$	$(57.2 \pm 0.9)\%$	$(0.4 \pm 1.7)\%$
$D_s^* \to \gamma D_s$, $D_s \to \phi\pi$	$(24.0 \pm 0.1)\%$	$(23.8 \pm 0.8)\%$	$(0.8 \pm 3.4)\%$
Weighted average			$(2.5 \pm 1.2)\%$

Table 4.15: The neutrino reconstruction efficiency ϵ_ν for CLEOII MC and data with different values of M_{jet}.

Data sample	$M_{jet} = 3.84 - 0.372P_K$	$M_{jet} = 3.80 - 0.388P_K$	$M_{jet} = 3.2$
$D^{*0} \to \gamma D^0$, $D^0 \to K^-\pi^+$ MC	$54.4\% \pm 0.5\%$	$59.3\% \pm 0.5\%$	$27.4\% \pm 0.4\%$
$D^{*0} \to \gamma D^0$, $D^0 \to K^-\pi^+$ data	$54.0\% \pm 1.9\%$	$59.1\% \pm 1.9\%$	$26.8\% \pm 1.5\%$
$D^{*0} \to \pi^0 D^0$, $D^0 \to K^-\pi^+$ MC	$52.6\% \pm 0.6\%$	$57.4\% \pm 0.6\%$	–
$D^{*0} \to \pi^0 D^0$, $D^0 \to K^-\pi^+$ data	$53.8\% \pm 1.6\%$	$59.9\% \pm 1.6\%$	–

We reweight the momentum spectrum to study this effect. First, we obtained weights from fully reconstructed D_s^* momentum spectrum in $D_s^{*+} \to \gamma D_s^+$, $D_s^+ \to \phi\pi^+$ in MC and data. We then reweighted the D_s^* momentum spectrum for the $D_s \to \mu\nu$ MC. We varied the weights by $\pm 3\sigma$ and see how much an impact it has on the efficiency. We concluded that the uncertainty due to the production spectrum is $< 1.9\%$ at the 90% confidence level.

Finally from the studies done above, the comparison of neutrino reconstruction in MC and data give us a 2.5% uncertainty in the neutrino reconstuction efficiency. The production spectrum has an uncertainty of $< 1.9\%$ at the 90% confidence level. There is also a 1.2% uncertainty on the muon identification efficiency. Thus, we take a total of 3.4% uncertainty in the detection efficiency, and obtain a value of $(3.38 \pm 0.11)\%$ for overall detection efficiency.

Selection Criteria

We change the lepton momentum requirement from 2.4 GeV/c to 2.6 GeV/c, and perform a fit to the mass differece using the same method as in Section 4.4.1. We obtained an efficiency corrected yield of 10273 ± 2269[stat.] as compared to 9763 ± 1806. We take the systematic uncertainty to be one half of the difference between them which turns out to be 2.6%.

Real and fake leptons

If we were to subtract the electron data and excess muon fakes to get the fit result, then we would need to know the systematic uncertainty due to lepton fakes as well as

μ/e normalization. To determine the systematic uncertainty due to lepton fakes, we vary the lepton fake rates by $\pm 1\sigma$, and perform the fits to the mass difference again. This variation in muon fake rate results in a 10.6% change in signal yield while the electron fake rate has an effect of 4.0%.

For hadron fractions, we estimated the uncertainty by first calculating the muon fakes using the hadron fraction (π/K/p fractions =60%/27%/13%) reported in the CLEO 1998 measurement. The impact of the particle fractions on the lepton fakes is shown in Table 4.16. This leads to a 0.7% systematic error for particle fractions.

Table 4.16: The lepton fake rates calculated with different hadron fractions.

Hadron fractions	52%/36%/12%	60%/27%/13%	70%/20%/10%
Muon fake rate	0.83%	0.77%	0.75%
Electron fake rate	0.05%	0.06%	0.07%
Signal yield	314 ± 79	311 ± 80	310 ± 81

The μ/e normalization is 1.177 ± 0.02. We vary this by $\pm 1\sigma$, and perform the fits to the mass difference again. We would get a 4.4% variation in signal yield due to the μ/e normalization.

Fit Procedure

To estimate the uncertainty due to fits, we use different fit methods to see how much the signal yield varies. Table 4.17 shows results of different fits to the mass difference $\Delta M = M(\gamma\mu\nu) - M(\mu\nu)$. Therefore, we estimate the uncertainty to be 2.7% due to the fit method used.

Table 4.17: The number of reconstructed signal events from different fits to $\Delta M = M(\gamma\mu\nu) - M(\mu\nu)$. In all cases, the π^0 background fit function obtained from MC is used in additional to what is mentioned below.

Fit Method	Signal Events
Use direct $D_{(s)}$ production as background	315 ± 76
after subtracting electron and excess fakes	310 ± 54
Use the electron data + excess fakes histogram as background function	314 ± 79
Use a fit to the electron data + excess fakes as background function	330 ± 61

We vary the parameters of the background shape for the fit to the electron data and excess muon over electron fakes in order to see the effect of background shape to signal yield. This is estimated to be 3.4%.

We add the two uncertainties described above in quadrature, and estimate the systematic uncertainities due to the fit procedure is 4.3%.

Normalization Mode

The systematics due to the $\phi\pi$ normalization can be studied by changing the fit methods. We changed to a different fit method by fitting to the mass difference for the $M(D_s)$ signal region, rather than performing a sideband subtraction. With a detection efficiency of $(5.26 \pm 0.02)\%$ and 1551 ± 44 reconstructed events, we get the number of $D_s^* \to \gamma D_s, D_s \to \phi\pi$ events to be 60055 ± 1869[stat.]. We take the difference $60055 - 58308 = 1747$ to be the systematics for the normalization mode.

4.4.3 Cross-checks

We perform some cross-check studies to demonstrate that the result obtained in Section 4.4.1 is rebust.

Background Subtracted Fits

As a cross-check, we subtract the muon data from the background estimated using the electron data and the lepton fakes. To demostrate that the fit procedure works, we tested on continuum MC sample. Figure 4.17 shows for both continuum MC and data the electron histogram and excess muon over electron fakes, as well as the events remained after subtracting the physics background due to real and fake leptons. Figure 4.18 is a fit to the mass difference for the muon data after the background subtraction. The fit for continuum MC results in 1208 ± 135 events, consistent with the 1340 expected signal events. This gives us confidence for the result in data in Figure 4.18 which gives a total of 315 ± 76 signal events, consistent with the fit result of 330 ± 61 without background subtraction.

Kinematic Constraints

We can also use additional kinematic constraints to help suppress background. One way to do that is to make use of the reconstructed γ, μ and D_s four-vectors and their angles with respect to each other. The D_s 4-momentum is reconstructed from $\overrightarrow{P}_{D_s} = \overrightarrow{P}_{\mu} + \overrightarrow{P}_{\nu}$. (See section 4.2.4 for the neutrino reconstruction.) Figure 4.19 shows the coordinate system with $\overrightarrow{P}_{D_s}$ defined to be pointed along the z-axis, and $\overrightarrow{P}_{\mu}$ lies on the y-z plane. The α is the angle between μ and D_s, the γ is the angle

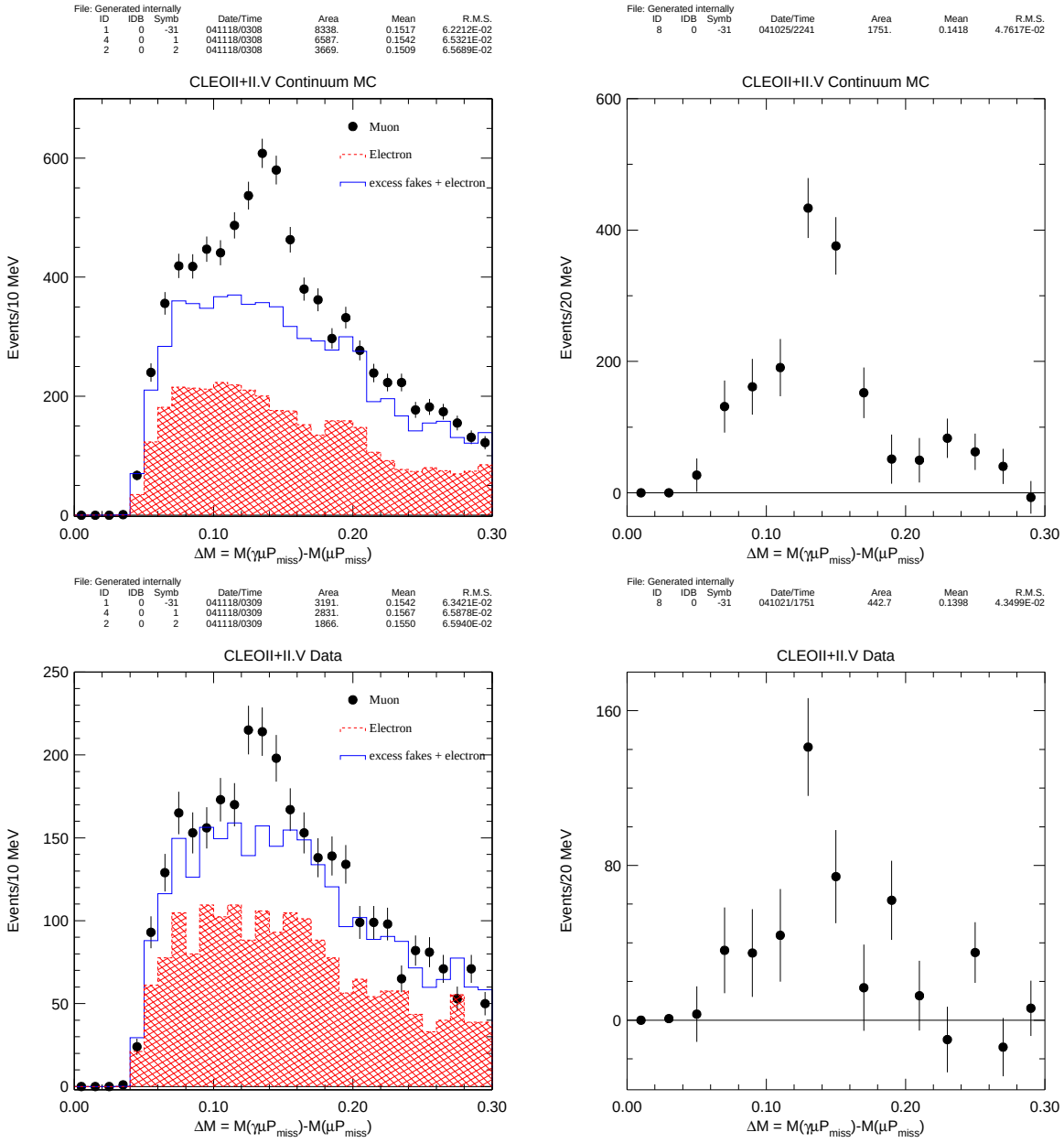

Figure 4.17: The plots on the left are the mass difference for CLEOII+II.V continuum MC (top) and data (bottom) for the muon and electron modes (after D_s mass constraint). The plots on the right shows the electron subtracted mass difference which includes signal events and background events that cannot be subtracted off by the electron modes. See Table 4.4 for background modes in continuum MC.

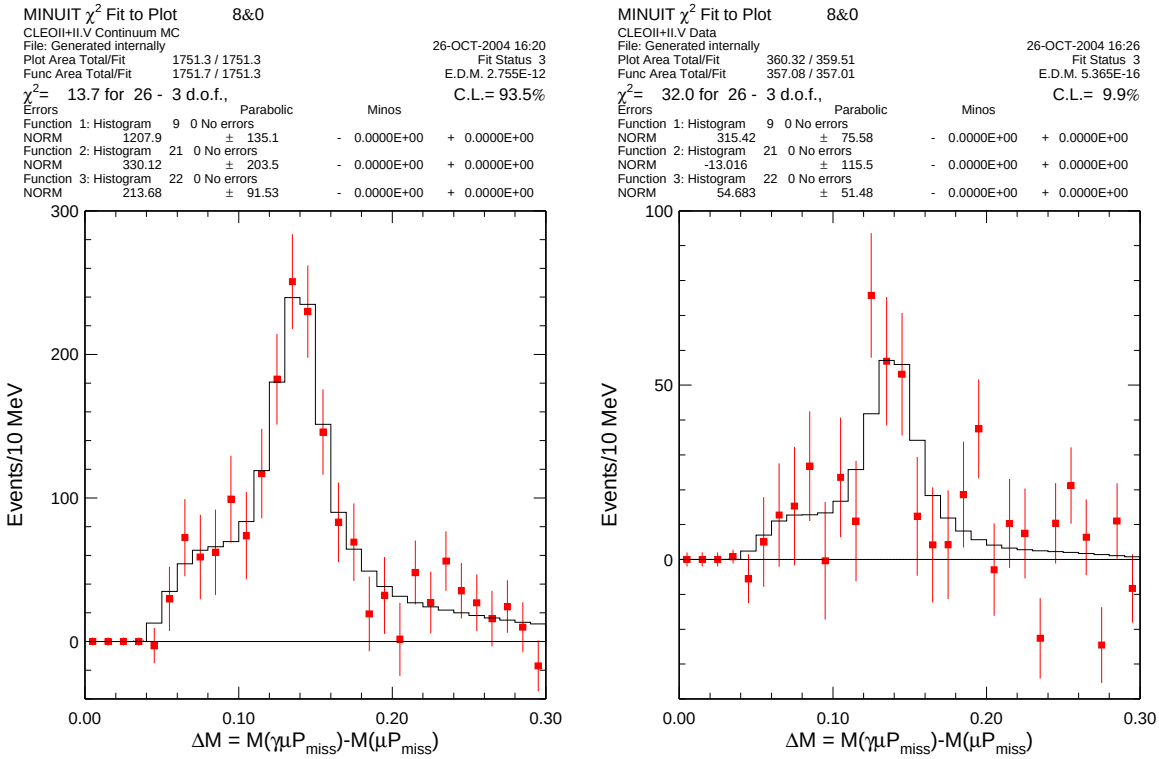

Figure 4.18: A fit to the mass difference for $D_s \to \mu\nu$ CLEOII+II.V continuum MC (left) and data (right). Function 1: signal; Function 2: $D_s^* \to D_s\pi^0$, $D_s \to \mu\nu$; Function 3: direct $D_s \to \mu\nu$ production.

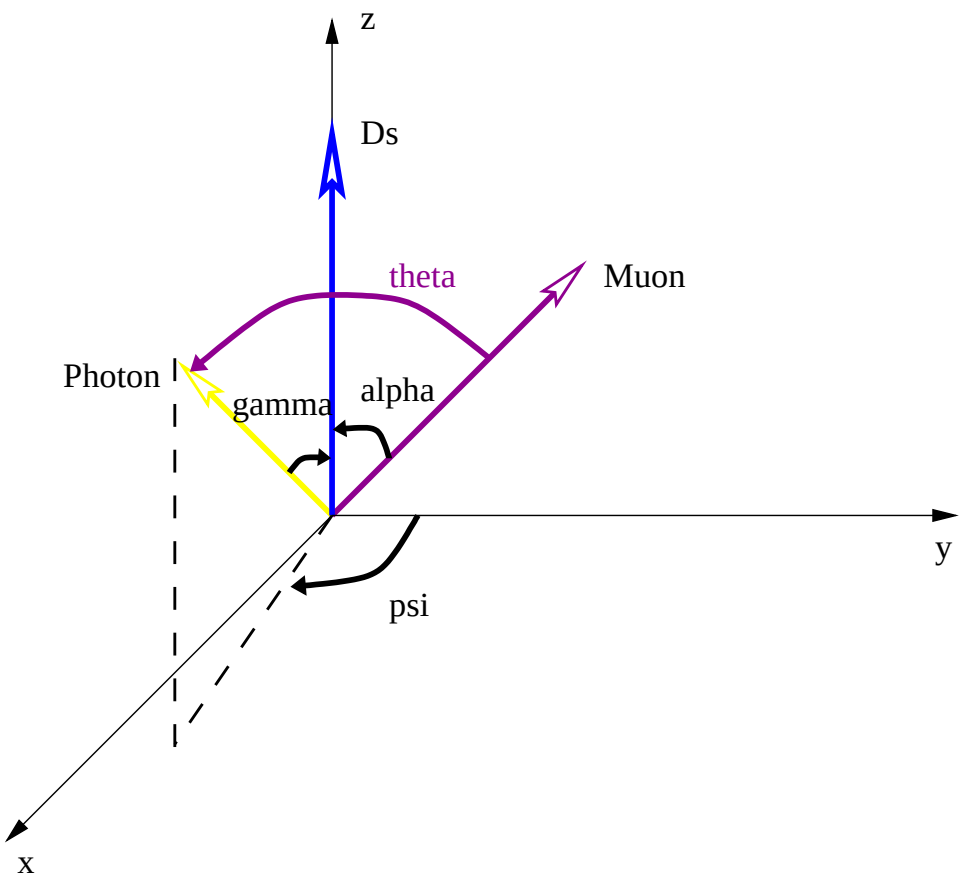

Figure 4.19: The coordinate system with P_{D_s} defined to be pointed along the z-axis. Muon is placed on the y-z plane. ψ is then the psi angle between the photon and the y-z plane.

between the photon and D_s, and the θ is the angle between photon and μ. By taking the dot product of the P_γ and P_μ unit vectors, we can calculate the ψ angle:

$$cos(\psi) = \frac{cos(\theta) - cos(\alpha)cos(\gamma)}{sin(\alpha)sin(\gamma)} \tag{4.6}$$

From conservation of energy and momentum, we can derive the following:

$$cos(\gamma) = \frac{2E_{D_s}E_\gamma - M^2_{D_s^*} + M^2_{D_s}}{2P_{D_s}P_\gamma} \tag{4.7}$$

$$cos(\alpha) = \frac{2E_{D_s}E_\mu - M^2_{D_s} - M^2_\mu}{2P_{D_s}P_\mu} \tag{4.8}$$

Note that these three angles only depend on the magnitudes of the momenta, the masses of the three particles: photon, muon, and D_s. Therefore, alternatively, we can make a guess of the D_s momentum by looping over some momentum range rather than obtaining the D_s momentum information from neutrino reconstruction. We take a step size of 5 MeV, and step through a range of D_s momentum to count number of steps that falls in the physical region of $-1 < cos(\gamma) < 1$ and $-1 < cos(\alpha) < 1$. We find that an effective constraint to suppress background is to require the D_s momentum be at least 500 MeV/c.

Figure 4.20 displays the muon data, electron data, and electron data plus excess muon over electron excess fakes. We notice that the backgrond shape is very different from the one without imposing this kinematic constraint in Figure 4.17. A fit is performed to the muon data without any background subtraction, and we obtain 421 ± 72 signal events. The fit functions included (1). a signal shape obtained from MC, (2). a fit function to the $D_s^* \to D_s\pi^0$, $D_s \to \mu\nu$ background, (3). a fit function to the electron data plus the muon over electron excess fakes. According to a MC study,

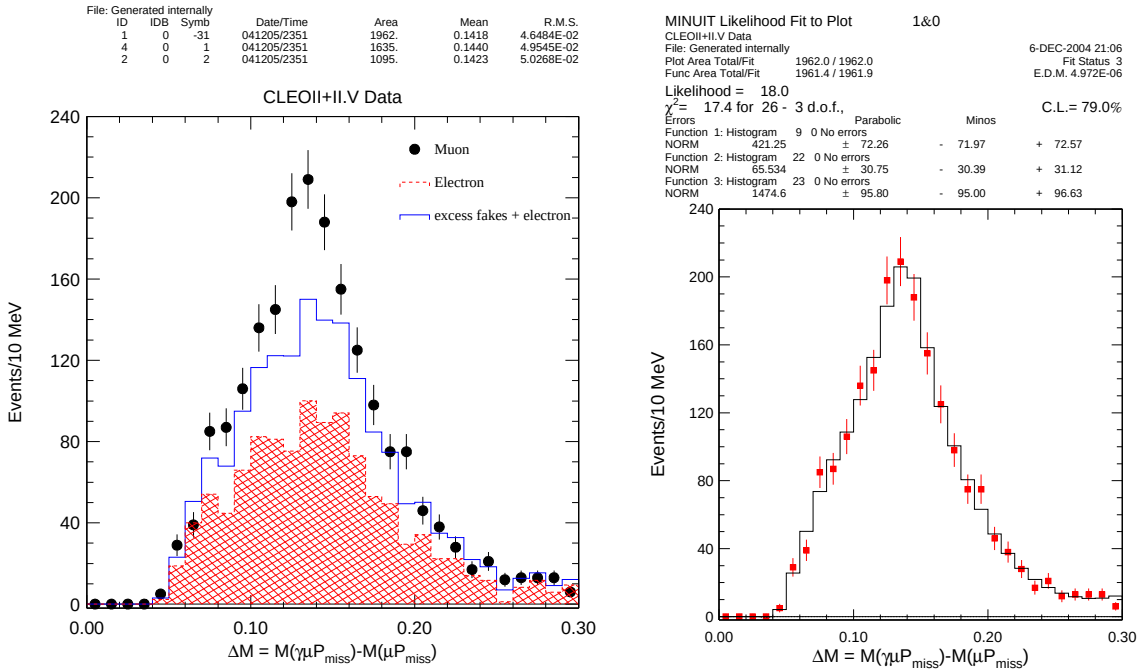

Figure 4.20: The plot on the left shows the mass difference for the muon data (points with error bars), the electron data (shaped histogram), and the electron data plus the muon over electron excess fakes (solid histogram). The plot on the right is a fit to the muon data using fit functions described in the text.

this kinematic constraint will only remove about a few % of signal events, which is smaller than the statistical uncertainty in the signal yield. Therefore, we conclude that the result obtained from imposing the kinematic constraints is consistent with the result of 330 ± 61 events in Section 4.4.1.

Figure 4.21 shows a fit to the mass difference after the muon data has been subtracted from the electron data and muon over electron excess fakes. The fit functions are a signal shape obtained from MC and a background function due to the $D_s^* \to D_s\pi^0$, $D_s \to \mu\nu$ decays. We obtain 319 ± 51 signal events from the fit. This is to compare with the 310 ± 54 events we obtained with the same fit method but without the kinematic constraints.

From the cross-checks performed above, we conclude that the signal yield is remained rebust with respect to various selection requirements and fit procedures.

4.5 Conclusions

In summary, the ratio of decay widths is measured to be $\Gamma(D_s \to \mu\nu)/\Gamma(D_s \to \phi\pi) = 0.167 \pm 0.031 \pm 0.011$. Inverting Equation 1.1, we can calculate the decay constant $f_{D_s} = (270 \pm 25 \pm 9 \pm 34)$ MeV using our measurement of the ratio of decay widths, the known PDG values of $\mathcal{B}(D_s \to \phi\pi) = (3.6 \pm 0.9)\%$ and mean D_s life time $\tau_{D_s} = 490 \times 10^{-15}$ s. We take the $|V_{cs}|$ to be 0.973. The first uncertainty in the f_{D_s} measurement is statistical and the second is systematic error due to the measured ratio of decay widths. The third error is the uncertainty due to branching fraction of $D_s \to \phi\pi$. This result is consistent with the previous CLEO measurement [44] of

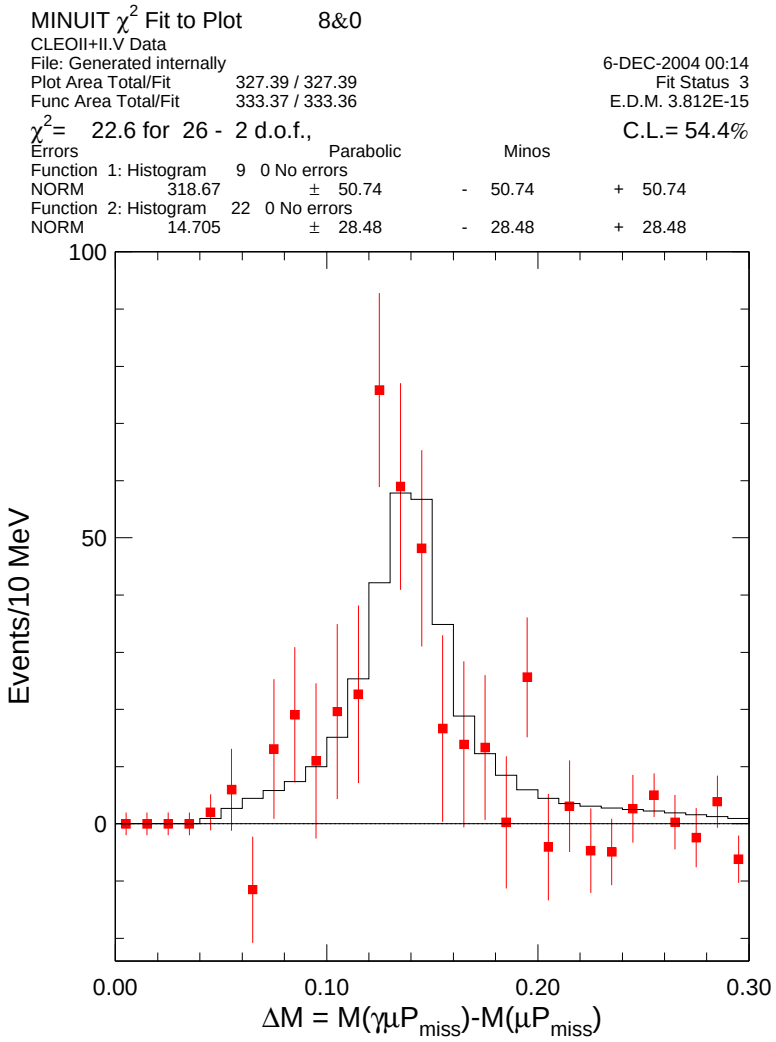

Figure 4.21: A fit to the background subtracted mass difference with kinematic constraints applied for CLEOII+II.V data.

$f_{D_s} = (280 \pm 19 \pm 28 \pm 34)$ MeV.

With a larger data sample and better track and shower information, we expected to improve upon the previous measurements of the ratio of decay widths $D_s \to \mu\nu / D_s \to \phi\pi$. We were able to optimize the event selection criteria and develop an analysis procedure to greatly reduce systematic errors. However, in the process of reducing systematic uncertainties, we sacrificed statistics and consequently incurred a larger statistical uncertainty even though we used a larger data sample.

A limiting source of the uncertainties in determining f_{D_s} comes from the measurement of the normalization mode $D_s \to \phi\pi$. Consequently, there is an interest in pursuing $D \to \mu\nu$ which does not suffer from this limiting factor. Alternatively, it would be ideal to measure the absolute branching fraction which is possible with the CLEO-c program when D and D_s's are produced at thresholds. Based on 60 pb^{-1} of CLEO-c data collected at $\psi(3770)$, CLEO [54] recently measured $\mathcal{B}(D \to \mu\nu) = (3.5 \pm 1.4 \pm 0.6) \times 10^{-4}$ and determined $f_D = (202 \pm 41 \pm 17)$ MeV, where the first error is statistical and the second is the systematic uncertainty. The absolute branching fraction measurement was made using an analysis of tagging one of the D produced from $e^+e^- \to D\bar{D}$ and searching for the other D which decays to $\mu\nu$. This measurement is statistically limited, so more data are being collected at CLEO to improve the precision of the f_D. In 2005, CLEO-c will be collecting data at $\sqrt{s} \sim 4140$ MeV at which D_s's are produced at threshold and the systematic uncertainty due to the normalization mode can be avoided.

Precise measurements of f_{D_s}, f_D and their ratio can be used as a calibration point to test Lattice QCD predictions for calculating f_{B_s}/f_{D_s} and f_B/f_D reliably, and thus

enhance our understanding of B and B_s decays. One latest theretical prediction [55] is $f_{D_s} = (263^{+5}_{-9} \pm 24)$ MeV. Currently, Lattice QCD has been able to predict up to $\sim 10\%$ precision, and it is important for experiments to be able to measure the decay constants with similar or better precision.

CHAPTER 5

Conclusions

Using 13.4 fb^{-1} of CLEO II and II.V data, we obtained the first confirming evidence for the existence of the $D^*_{sJ}(2317)$. The signature is a peak near 350 MeV/c^2 in the reconstructed $M(D_s^+\pi^0) - M(D_s)$ mass difference, using the $\phi\pi^+$ decay of the D_s^+. We have also observed and established the existence of a second new $c\overline{s}$ state decaying to $D_s^*\pi^0$. Accounting for the cross-feed backgrounds, we have measured the mass splittings of the two states with respect to the D_s and D_s^* mesons. For the $D^*_{sJ}(2317)$, we obtain $M(D^*_{sJ}(2317))-M(D_s) = 350.0\pm1.2$ [stat.]±1.0 [syst.] MeV/c^2, consistent with the observation from other experiments, and we find its natural width to be $\Gamma < 7$ MeV (90% C.L.). For the $D_{sJ}(2463)$, we obtain $M(D_{sJ}(2463))-M(D_s^*) = 351.2 \pm 1.7$ [stat.] $\pm$ 1.0 [syst.] MeV/c^2. The natural width of this state is also found to be $\Gamma < 7$ MeV.

We have also searched for the $D^*_{sJ}(2317)$ and $D_{sJ}(2463)$ in other decay modes such as $D_s\gamma$, $D_s^*\gamma$, and $D_s\pi^+\pi^-$. We find no evidence of decays to these final states, and set the upper limits on the branching fractions relative to the oberverd $D_s\pi^0$ mode. The results presented in Chapter 3 of this thesis were published[36] in 2003.

Finally, we have presented an improved measurement of the leptonic D_s-meson decays in the full data sample of 13.4 fb^{-1}. Improvements in the understanding of

background processes and optimized lepton-identification procedures have resulted in significant improvements in systematic uncertainties relative to the previous CLEO measurement [44]. We have used the normalization mode $D_s \to \phi\pi$ to obtain the ratio of decay widths for $\Gamma(D_s \to \mu\nu)/\Gamma(D_s \to \phi\pi) = 0.167 \pm 0.031 \pm 0.011$, from which we extract the decay constant $f_{D_s} = (270 \pm 25 \pm 9 \pm 34)$ MeV.

BIBLIOGRAPHY

[1] S. Eidelman et al. (Particle Data Group). Phys. Lett. **B592**, 1 (2004).

[2] S. Godfrey and N. Isgur. Phys. Rev. D **32**, 189 (1985).

[3] S. Godfrey and R. Kokoski. Phys. Rev. D **43**, 1679 (1991).

[4] J. Bartelt and S. Shukla. Ann. Rev. Nucl. Part. Sci. **45**, 133 (1995).

[5] A. Chen et al. (CLEO). Phys. Rev. Lett. **51**, 634 (1983).

[6] R. Briere et al. (CLEO). CLNS **01/1742** (2001).

[7] H. Albrecht et al. (ARGUS). Phys. Lett. **B146**, 111 (1984).

[8] N. Isgur and M. B. Wise. Phys. Rev. Lett. **66**, 1130 (1991).

[9] A. DeRujula et al. Phys. Rev. Lett. **37**, 785 (1976).

[10] M. D. Pierro and E. Eichten. Phys. Rev. D **64**, 114004 (2001).

[11] H. Albrecht et al. (ARGUS). Phys. Lett. **B230**, 162 (1989).

[12] Y. Kubota et al. (CLEO). Phys. Rev. Lett. **72**, 1972 (1994).

[13] B. Aubert et al. (BaBar). Phys. Rev. Lett. **90**, 242001 (2003).

[14] R. N. Cahn and J. D. Jackson. Phys. Rev. D **68**, 037502 (2003). `hep-ph/0305012`.

[15] T. Barnes et al. Phys. Rev. D **68**, 054006 (2003). `hep-ph/0305025`.

[16] E. van Beveren and G. Rupp. Phys. Rev. Lett. **91**, 012003 (2003). `hep-ph/0305035`.

[17] W. Bardeen, E. J. Eichten, and C. T. Hill. Phys. Rev. D **68**, 054024 (2003). `hep-ph/0305049`.

[18] A. P. Szczepaniak. Phys. Lett. **B567**, 23 (2003). `hep-ph/0305060`.

[19] S. Godfrey. Phys. Lett. B **568**, 254 (2003). `hep-ph/0305122`.

[20] P. Colangelo and F. D. Fazio. Phys. Lett. B **570**, 180 (2003). hep-ph/0305140.

[21] M. A. Nowak et al. Phys. Rev. D **48**, 4370 (1993).

[22] W. A. Bardeen and C. T. Hill. Phys. Rev. D **49**, 409 (1994).

[23] P. L. Cho and M. B. Wise. Phys. Rev. D **49**, 6228 (1994).

[24] M. A. Nowak et al. Hep-ph/0307102.

[25] S. Okubo. Phys. Lett. **5**, 165 (1963).

[26] J. Iizuka. Prog. Theor. Phys. Suppl. **37-38**, 21 (1966).

[27] J. Iizuka et al. Prog. Theor. Phys. **35**, 1061 (1966).

[28] G. Zweig. CERN Report No. TH-401 and TH-412 (1964).

[29] A. Juettner and J. Rolf. Phys. Lett. **B560**, 59 (2003). hep-lat/0302016.

[30] Y. Kubota et al. (CLEO). Nucl. Instrum. Meth. **A320**, 66 (1992).

[31] T. Hill et al. (CLEO). Nucl. Instrum. Meth. **A418**, 32 (1998).

[32] K. Hagiwara (Particle Data Group). Phys. Rev. D **66**, 010001 (2002).

[33] J. Gronberg et al. Phys. Rev. Lett. **75**, 3232 (1995).

[34] S. Li et al. CBX 03-21.

[35] S. Li et al. The calculation of cross feed backgrounds in Section 3.4.1 did not account for the possibility of $D_{sJ}(2463) \to D_{sJ}(2317)\gamma$ decays. However, the impact of ignoring this channel is insignificant based on our upper limit.

[36] D. Besson et al. (CLEO). Phys. Rev. D **68**, 032002 (2003). hep-ex/0305100.

[37] B. Aubert et al. (BaBar). Phys. Rev. D **69**, 031101 (2004). hep-ph/0310050.

[38] K. Abe et al. (Belle). Phys. Rev. Lett. **92**, 012002 (2004). hep-ph/0307052.

[39] P. Krokovny et al. (Belle). Phys. Rev. Lett. **91**, 262002 (2003).

[40] B. Aubert et al. (BaBar). Phys. Rev. Lett. **93**, 181801 (2004). hep-ex/0408041.

[41] B. Aubert et al. Hep-ex/0408067.

[42] A. Heister et al. (ALEPH). Phys. Lett. B **528**, 1 (2002).

[43] V. Alexandrov et al. (BEATRICE). Phys. Lett. B **478**, 31 (2000).

[44] M. Chadha et al. (CLEO). Phys. Rev. D **58**, 032002 (1998).

[45] K. Kodama et al. (E653). Phys. Lett. B **382**, 299 (1996). `hep-ex/9606017`.

[46] J. Z. Bai et al. (BES). Phys. Rev. Lett. **74**, 4599 (1995).

[47] D. Acosta et al. (CLEO). Phys. Rev. D **49**, 5690 (1994).

[48] S. Aoki et al. (WA75). Prog. Theor. Phys. **89**, 131 (1993).

[49] M. Artuso et al. CLEO collaboration, CLEO 04-3, CLNS 04/1861, submitted to Physical Review D.

[50] F. Morrow. CSN-91/316.

[51] I. Narsky (2001). Southern Methodist University Ph.D. Thesis.

[52] L. Gibbons et al. CBX 95-6.

[53] D. Atwood and W. J. Marciano. Phys. Rev. D **D41**, 1736 (1990).

[54] G. Bonvicini et al. CLEO collaboration, CLEO 04-15, CLNS 04/1896, submitted to Physical Review D.

[55] J. Simone et al. Hep-lat/0410030.